Electromagnetic scattering of dense media with application to active and passive microwave remote sensing of terrestrial snow

Wenmo Chang

A dissertation

submitted in partial fulfillment of the

requirements for the degree of

Doctor of Philosophy

University of Washington

2015

Reading Committee:

Leung Tsang, Chair

John Sahr

Kung-Hau Ding

Program Authorized to Offer Degree:

Department of Electrical Engineering

University of Washington

Abstract

Electromagnetic scattering of dense media with application to active and passive microwave remote sensing of terrestrial snow

Wenmo Chang

Chair of the Supervisory Committee:

Prof. Leung Tsang

Department of Electrical Engineering

It is of great importance to estimate the amount and the variation of water storage in the form of seasonal snowpack, in order to effectively monitor and manage the water resources all over the world. It is believed that significant temporal changes and spatial changes in local snowpack, regional snowpack and global snow are due to climate change. The Snow Water Equivalent (SWE) is defined as the depth of some hypothetical water which is melted instantaneously from an entire snowpack. Therefore the estimate of SWE is critical to the understanding of the water cycle, water resource management, prediction of climate change, flood forecasting, etc. Microwave remote sensing has been used in estimating SWE for decades. As radar measurement, radiometric measurement, and ground measurement data abound in microwave

remote sensing campaigns, it is important to connect the ground measurement to electrical measurement by developing accurate physical models for snow, as well as scattering models for random medium. In this dissertation, Dense Media Radiative Transfer (DMRT) is combined with Quasi-Crystalline Approximation (QCA) and bicontinuous model. The DMRT-QCA and DMRT-bicontinuous are applied to data analysis of recent multi-frequency backscattering coefficients measurements in SnowSAR and SnowScat campaigns respectively. Then DMRT-bicontinuous model is used to study both active and passive remote sensing in the NoSREx campaign. Backscattering enhancement effect is considered. Lastly, the QCA model and the bicontinuous model are compared in microwave scattering as well as the medium characterization. The parameter extraction of these two models from ground measurement are discussed.

ACKNOWLEDGMENTS

First and foremost, the author would like to show deepest gratitude to my supervisor, Prof. Leung Tsang, a respectable, responsible and resourceful scholar, who has provided me with valuable guidance in every stage of the writing of this thesis. Without his enlightening instruction, impressive kindness and patience, the thesis could not be completed. His keen and vigorous academic observation enlightens me not only in this thesis but also in the future study.

The author shall extend the thanks to Prof. John Sahr, Prof. Kung-Hau Ding, Prof. Yasuo Kuga, and Dr. Edwards Josberger for all their kindness and help. I would like to thank all of my committee members who have helped me to develop the fundamental and essential academic competence.

Besides, the author would like to thank all former and current students in Laboratory of Applications and Computations in Electromagnetics and Optics, for their encouragement and technical support.

The work in this thesis was supported by the Remote Sensing Theory program of NASA and the IIP "WISM" project of NASA. The author appreciates the financial support from these projects.

DEDICATION

I wish to dedicate this dissertation to my mother, Yuchun Wang, who gave me unconditional love throughout my life, and support through the PhD study and completion of dissertation. I could not be here without your love.

TABLE OF CONTENTS

LIST OF TABLES

Number *Page*

LIST OF FIGURES

Number *Page*

CHAPTER 1: INTRODUCTION

1.1 BACKGROUND AND MOTIVATION

The quantitative estimation of water storage in seasonal snowpack on earth is of great importance in geophysical science. It is known that the spatial and the temporal changes in the snowpack, whether localized, regional, or global, are significantly caused by climate change. The Snow Water Equivalent (SWE) of a snowpack is defined as a hypothetical depth of water which is immediately melted from this snowpack. The quantitative estimation of SWE is of great importance to hydrology science and other cross field science, in particular crucial to the knowledge of the water cycle, water management, prediction of climate change, flooding forecast, and so on [I1]. In the past decades, microwave remote sensing techniques have been extensively used in estimating SWE [I1] – [I6]. Microwave remote sensing missions can be categorized by their carriers: satellite missions, airborne campaigns, and ground campaigns. The latter two kinds of remote sensing missions are generally used for the feasibility study of the first kind, as satellite missions are expensive and not easy to be launched frequently. Microwave remote sensing missions can be also categorized by the ways they collect microwave signals: passive remote sensing, and active remote sensing. Passive remote sensing collects thermal emission from the target object, while active remote sensing uses a radar or a scatterometer to transmit a signal and then receive the reflected signal from the target.

Table 1-1 Passive and active spaceborne remote sensing missions

Name of the mission	Spatial resolution	Repetition cycle	Frequencies of active [GHz]	Frequencies of passive [GHz]	State of the mission
AMSR-E	8 – 29 km	1 day	NA	10.65, 18.7, 36.5	2002 – 2011
GCOM-W AMSR-2	5 – 50 km	1 – 2 days	NA	10.65, 18.7, 36.5	Launched in 2012
WindSat	8 – 25 km	Twice per day	NA	10.7, 18.7, 37.0	Launched in 2003
COSMO-SkyMed	Active SAR: 1 (Spotlight) -100m (ScanSAR)	16 days	9.6	NA	Four satellites launched 2007-2010
SCLP	Active SAR: 50 – 100 m Passive: Sub-km	15 days	9.6, 17.2	18.7, 36.5	Decadal mission of NASA Tier 3
CoReH2O	Active SAR: 50 m	3 – 15 days	9.6, 17.2	NA	Feasibility Study ESA 2009-2013

The passive and active spaceborne microwave remote sensing missions that have been launched or planned are listed in Table 1-1 [I1]. Passive microwave remote sensing of SWE already had 30-year heritage [I7] [I8]. To name a few, SSM/R and SSM/I were series of passive microwave radiometer systems. SSM/R had 5 operating frequencies and was launched in 1978. SSM/I was the successor of SSM/R. SSM/I had 7 channels at 4 operating frequencies. AMSR-E was launched by NASA in 2002, and stopped spinning since 2011. AMSR-E worked on 11 channels at 6 operating frequencies. Its spatial resolution ranged from 6 to 75 km [I7]. After it stopped spinning, its successor AMSR-2 was installed on GCOM-W1 and launched by Japan in 2012. AMSR-2 had 13 channels at 7 operating frequencies. WindSat was a satellite-based polarimetric microwave radiometer launched in 2003 by US Navy. Its spatial resolution ranged from 8 to 39 km.

Spaceborne active remote sensing missions have received considerable attention recently [I1]. The Cold Regions Hydrology High-Resolution Observatory (CoReH2O) was a proposed satellite mission in European Space Agency (ESA) [I2] [I3]. This mission proposed to make measurement of water storage on land surfaces and in glaciers in the global range. The proposed frequencies in CoReH2O are 9.6 and 17.2 GHz, which are used in a Synthetic Aperture Radar (SAR) system with a spatial resolution of 50 meters. Therefore this mission will provide observations at fine spatial resolution scales, and thus will offer the possibility to retrieve SWE at such fine resolution. This mission was one of the three candidate missions considered by ESA in the 7th Earth Explorer. However, the mission was not selected by ESA in March 2013. Snow and Cold Land Processes (SCLP) is NASA's Tier-3 level decadal mission. The most important feature of this satellite mission is making passive microwave sensors measurements and the Synthetic Aperture Radar (SAR) measurements over the same site and at the same time. The

passive frequencies are 18.7 and 36.5 GHz, while the active frequencies are 9.6 and 17.2 GHz at spatial resolutions of 50 – 100m [I2].

Table 1-2. Ground campaigns and airborne campaigns

Name of the campaign	Platform	Equipment	Spatial resolution	Frequency [GHz]	Aim of the campaign
CLPX 2002-2003 2006-2008	Airborne	Scatterometer TerraSAR, SAR	100m	13.4GHz X band	Feasibility study of SCLP
SnowSAR 2009-2013	Airborne	SAR	10 m	9.6, 17.2	Feasibility study of CoReH2O
SnowScat 2009-2012	Ground-based tower	Scatterometer	NA	10.2, 13.3, 16.7	Feasibility study of CoReH2O

The ground-based and airborne campaigns that were performed as part of the feasibility studies of CoReH2O and SCLP missions are listed in Table 1-2. The Cold Land Processes Field Experiments (CLPX) were series of airborne campaigns performed in the central Rocky Mountains of the western US in 2002, and in Alaska in 2003. It operated at 100 meters resolution and Ku-band (13.4 GHz).

The mini-SAR airborne system SnowSAR was an ESA effort, and was deployed to collect data over the Sodankylä area, Finland [I2] [I3]. The SnowSAR system operated at a mean incident angle of 40 degree, with dual-frequency (X-band 9.6 GHz, Ku-band 17.25 GHz) and dual polarization (VV and HV). At the designated flight altitude, SnowSAR system had 400 meter swath width; measured data was provided at 2 meter and 10 meter resolution scales. The ESA's SnowScat instrument includes a frequency sweeping (X- to Ku-band) and tower-based scatterometer [I2]. The instrument was mounted on a ground based tower at the height of 9 meters. The measurement of snow was performed in a forest-free area. Any vegetation factor, such as trees, bushes, or shrubs, was removed from the area before measurements were made. The repeated measurements using SnowScat, were performed every four hours, and covered inclined incident angles from 30 to 60 degrees with a 10-degree step. In order to mitigate the random speckle effects from natural variation of the snowpack and the soil background, measurement at each inclined incident angle was averaged by 17 discrete looks in azimuthal directions. Radar backscattering coefficients at four polarizations (HH, HV, VH, and VV) of the snowpack were measured. SnowScat measurements were processed to three discrete bands of 2 GHz, with center frequencies at 10.2, 13.3 and 16.7 GHz.

The Snow and Cold Land Processes (SCLP) was a proposed satellite mission having both multi-frequency Synthetic Aperture Radar (SAR) and multi-frequency microwave radiometer. The development of Wideband Instrument for Snow Measurement (WISM) is for the planning of SCLP mission. It will make both active and passive measurements over the same site and the same time. Cold Land Processes Field Experiment (CLPX) used an airborne scatterometer at Ku-band (13.4 GHz) at 100 meter resolution scale. It was performed as feasibility studies of SCLP. The CLPX experiments were performed in the central Rocky Mountains in the western US

between 2002 and 2003. CLPX was followed by a series of experiments: CLPX-II in Colorado between 2006 and 2008, CLPX-II in Alaska between 2007 and 2008, and CLPX-III in Colorado between 2009 and 2010.

As active radar, passive radiometry, and ground measurement data abound in microwave remote sensing campaigns, it is crucial to connect the ground measurement data to electrical measurement data by developing accurate physical models for snow, as well as scattering models for random medium [I9] – [I12]. The scattering model can be validated by transmission loss experiments [I13], backscattering measurement [I4] [I14] – [I16], and brightness temperature measurement [I7]. In transmission loss experiments, electromagnetic wave is incident in the normal direction of the top surface a snow slab. The total incident intensity on the slab is measured and recorded. The total intensity transmitted through the air snow interface is reduced by the air-to-snow transmission coefficient. At each position in the snow slab, the total coherent intensity attenuates due to absorption and scattering effects of the ice grains. The attenuation follows exponential decaying function, so the ratio of the intensity at the bottom of the snow slab to that at the top will determine the decaying factor and the extinction coefficient [I13].

In addition to the scattering and emission experiments, people in the past used correlation length to characterize the physical medium of snow [I17] – [I19]. Images were taken from real snow, and coarse correlation function is extracted [I20] [I21]. From the decaying characteristic of the function close to the origin, the correlation length is extracted. The relationship between the correlation length and the grain size was empirically established [I22].

1.2 RESEARCH METHODOLOGY AND OVERVIEW OF THE DISSERTATION

In numerical simulation, both QCA and bicontinuous model will give phase matrices and scattering coefficients. Assuming negligible absorption effect, the scattering coefficients of the scattering models can be validated by the measured extinction coefficients of the snow slab, which is taken out from the real snowpack. The scattering models can be also combined with DMRT equations, to predict the radar backscattering and brightness temperature. These prediction are then validated by the real measurement data.

In this dissertation, Chapter 2 applied Dense Media Radiative Transfer (DMRT) to SnowScat and SnowSAR campaigns [I4] [I5]. The DMRT theory is applied to data analysis of multi-channel microwave backscattering coefficients from the snowpacks in SnowScat and SnowSAR campaigns. Quasi-Crystalline Approximation (QCA) model and the bicontinuous model are both used on the multilayer snow medium in the two campaigns. The common feature of the two models is that two size parameters are used in both models. Single grain size and stickiness parameter are employed in QCA model. The bicontinuous model has two model parameters: the mean wavenumber $\langle\zeta\rangle$ and the clustering parameter b. The mean wavenumber $\langle\zeta\rangle$ is inversely corresponding to the average grain size, while the parameter b determines the spreading width of the wavenumber distribution, and is thus related to the clustering property of the medium. The bicontinuous model is used to generate the microstructures of snow in each realization of Monte Carlo simulation, and Maxwell equations are solved numerically by full wave methods for each sample of automatically generated structure, in order to compute the extinction coefficient and the phase matrices. Other medium characterization of the bicontinuous medium include covariance (correlation) functions and Specific Surface Area (SSA), both of which can be computed from the parameters $\langle\zeta\rangle$ and b. When making comparisons to the electrical measurement, ground measurements of single grain size, snow densities, snow depth, layering

information, and SSA of snow cover are used as the input parameters to the scattering models. The geometric descriptions and the scattering properties of the QCA and the bicontinuous model are compared with past models. When making the multi-frequency-channel data comparisons, the same physical parameters will be used for all three frequencies: X-band 10.2 GHz, Ku-band 13.3 GHz and 16.7 GHz. It is worth noting that the DMRT-QCA and DMRT-bicontinuous models provide flexible frequency dependence, grain size dependence, and angular distribution that are distinct from the conventional Rayleigh scattering model, and agree well with experimental observations.

In Chapter 3, the DMRT theory is used to study both active and passive remote sensing data simultaneously. Both radar backscattering coefficients and brightness temperatures are computed and validated to NoSREx campaign using the same physical parameters as the input. The backscattering enhancement effects, which stems from the constructive superposition in the dual backscattering paths, will increase the computed radar backscattering coefficients, but will not decrease the emissivity or the brightness temperature. With inclusion of the backscattering enhancement effects in co-polarization backscattering coefficients, the vector radiative transfer equations are solved by an iterative approach with cyclical correction. The order of scattering automatically takes the multiple scattering effects into account. Both QCA and bicontinuous models are used in the computation. The DMRT-bicontinuous model is then applied to the ground measurement and electrical measurement in NoSREx campaign in the winter season of 2010 – 2011. Numerical results agree well with multi-channel data from both scatterometer (X- to Ku-bands) and radiometer (X- to Ka-bands).

In Chapter 4, comparison studies are made between the QCA-Mie model and the bicontinuous model in microwave scattering from terrestrial snow. Both the scattering properties and the

medium characterization are compared. For QCA, the multi-size and the sticky particle models are used. For bicontinuous model, different probability distribution function for the wavenumber are used. The scattering rate and the angular distribution of scattering using the mean cosine of scattering are compared, and it is shown that the two models have similar properties. In medium characterization, the pair distribution functions is used in QCA to derive the correlation functions. It is shown that both the Percus-Yevick pair functions and the bicontinuous model have tails in the correlation functions that are distinctly different from the traditional exponential correlation functions. The methodologies of using ground measurements of grain size distributions and correlation functions to obtain model parameters are addressed. In the past, it has been difficult to derive input parameters such as stickiness for the QCA model. In this thesis, the correlation function is derived from the pair distribution functions, and can be obtained from digitized pictures of snow. Thus by comparing the correlation function, parameters such as stickiness can be derived.

The last two proposed satellite missions listed in Table 1-1 use radar at dual frequencies and dual polarizations. For example, the proposed measurement of CoReH2O include co- and cross-polarization backscattering at two different frequencies: σ_{VV} and σ_{VH} at 9.6 and 17.2 GHz. Therefore these four measurement will potentially retrieve four parameters which characterize global snow. The snow density and the snow depth are two of the key parameters of a snowpack, as the SWE is the product of density and depth. Another two parameters are the size parameters of the snow models, such as grain size and stickiness parameter of QCA model, or mean wavenumber and b of bicontinuous model. Therefore the forward scattering model studied in this thesis should have four input parameters: snow depth, snow density, and the two size parameters. And then a look-up table of the backscattering will be created. In the corresponding retrieval

algorithm, the four measured backscattering will be matched to the look-up table by minimizing RMSE. Then the snow depth, snow density, and two size parameters will be retrieved. In this way, no ground data such as grain size, is required in the retrieval algorithm, which makes it possible for global snow.

Passive radiometry data are complementary to the active radar data, although the passive data are collected at coarse spatial resolution. However, when the snow depth exceeds 2 meters, saturation effect in the brightness temperature will be observed. This is caused by the attenuation in the large optical depth of the snow medium, especially at high frequencies such as Ka-band. In order to sense the thermal emission from deep snow, low frequencies data such as X-band data should be considered. SodRad instruments of NoSREx campaign provide brightness temperature at 10.65 GHz, so it is useful for retrieving the snow depth of deep snow, such as 2 – 4 meters.

1.3 REFERENCES

[I1] Board, Space Studies. *Earth science and applications from space: National imperatives for the next decade and beyond*. National Academies Press, 2007.

[I2] H. Rott, S. H. Yueh, D. W. Cline, C. Duguay, R. Essery, C. Haas, F. Heliere, M. Kern, G. Macelloni, E. Malnes, T. Nagler, J. Pulliainen, H. Rebhan, and A. Thompson, "Cold Regions Hydrology High-Resolution Observatory for Snow and Cold Land Processes," *Proceedings of the IEEE* , vol.98, no.5, pp.752,765, May 2010

[I3] H. Rott, D. W. Cline, C. Duguay, R. Essery, P. Etchevers, I. Hajnsek, M. Kern, G. Macelloni, E. Malnes, J. Pulliainen, and S. H. Yueh, "CoReH2O, a dual frequency radar mission for snow and ice observations," *Geoscience and Remote Sensing Symposium (IGARSS), 2012 IEEE International* , vol., no., pp.5550,5553, 22-27 July 2012

[I4] A. Coccia, C. Trampuz, E. Imbembo, and A. Meta, "First Results of SnowSAR, the new X- and Ku-Band Polarimetric Airborne SAR Sensor supporting the CoReH2O Mission." *Workshop on Advanced RF Sensors and Remote Sensing Instruments, ESA/ESTEC, Noordwijk, NL*. 2011.

[I5] H. Rott, T. Nagler, M. Heidinger, F. Müller, G. Macelloni, F. Montomoli, G. Fontanelli, U. Cortezi, M. Gai, R. Liguri, R. Scheiber, I. Hajnsek, D. Flach, J. Pulliainen, A. Arslan, E. Malnes, T. Tollefsen, K. J. Grottum, P. Etchevers and Y. Durand, “Development of Snow Retrieval Algorithms for CoReH$_2$O,” *Final Report. ESA ESTEC Contract No. 22830/09/NL/JC*.

[I6] A. T. C. Chang, J. L. Foster, and D. K. Hall. "Nimbus-7 SMMR derived global snow cover parameters." *Annals of Glaciology* 9.9 (1987): 39-44.

[I7] R. E. Kelly; A. T. Chang; L. Tsang; and J. L. Fosters, "A prototype AMSR-E global snow area and snow depth algorithm," *Geoscience and Remote Sensing, IEEE Transactions on* , vol.41, no.2, pp.230,242, Feb. 2003

[I8] G. Macelloni; S. Paloscia; P. Pampaloni; and M. Tedesco, "Microwave emission from dry snow: a comparison of experimental and model results," *Geoscience and Remote Sensing, IEEE Transactions on* , vol.39, no.12, pp.2649,2656, Dec 2001

[I9] J. T. Pulliainen, J. Grandell, and M. T. Hallikainen. "HUT snow emission model and its applicability to snow water equivalent retrieval." *Geoscience and Remote Sensing, IEEE Transactions on* 37.3 (1999): 1378-1390.

[I10] J. Lemmetyinen, J. Pulliainen, A. Rees, A. Kontu, Y. Qiu, and C. Derksen, “Multiple-layer adaptation of HUT snow emission model: comparison with experimental data,” *IEEE Trans. Geosci. Remote Sens.*, vol. 48, no. 7, pp. 2781-2794, July 2010.

[I11] C. Mätzler, and A. Wiesmann. "Extension of the microwave emission model of layered snowpacks to coarse-grained snow." *Remote Sensing of Environment* 70.3 (1999): 317-325.

[I12] A. Wiesmann, and C. Mätzler. "Microwave emission model of layered snowpacks." *Remote Sensing of Environment* 70.3 (1999): 307-316.

[I13] M. T. Hallikainen, F. T. Ulaby and T. E. Deventer, “Extinction behavior of dry snow in the 18 to 90 GHz range,” *IEEE Trans. Geosci. Remote Sens.*, vol.25, no.6, pp. 737-745, 1987

[I14] J. Shi; J. Dozier; and H. Rott, "Snow mapping in alpine regions with synthetic aperture radar," *Geoscience and Remote Sensing, IEEE Transactions on* , vol.32, no.1, pp.152,158, Jan 1994 doi: 10.1109/36.285197

[I15] J. Shi; and J. Dozier, "Inferring snow wetness using C-band data from SIR-C's polarimetric synthetic aperture radar," *Geoscience and Remote Sensing, IEEE Transactions on* , vol.33, no.4, pp.905,914, Jul 1995

[I16] J. Shi, and J. Dozier. "Mapping seasonal snow with SIR-C/X-SAR in mountainous areas." *Remote Sensing of Environment* 59.2 (1997): 294-307.

[I17] C. Mätzler, "Autocorrelation functions of granular media with free arrangement of spheres, spherical shells or ellipsoids." *Journal of Applied Physics* 81.3 (1997): 1509-1517.

[I18] C. Mätzler, "Improved Born approximation for scattering of radiation in a granular medium." *Journal of Applied Physics* 83.11 (1998): 6111-6117.

[I19] A. Wiesmann, C. Mätzler, and T. Weise, “Radiometric and structural measurements of snow samples,” *Radio Science*, vol. 33, no. 2, pp. 273-289, 1998.

[I20] F. Vallese, and J. A. Kong. "Correlation function studies for snow and ice." *Journal of Applied Physics* 52.8 (1981): 4921-4925.

[I21] S. Schleef, and H. Loewe. "X-ray microtomography analysis of isothermal densification of new snow under external mechanical stress." *Journal of Glaciology* 59.214 (2013): 233-243.

[I22] C. Mätzler, “Relation between grain-size and correlation length of snow,” *J. Glaciol*., vol. 48, no. 162, pp. 461-466, 2002.

CHAPTER 2: DENSE MEDIA RADIATIVE TRANSFER APPLIED TO SNOWSCAT AND SNOWSAR

2.1 INTRODUCTION

Snow Water Equivalent (SWE) is the equivalent depth of water in a given snowpack. The estimation of this parameter is important for water resource management, prediction of climate change, flood forecasting, etc. Microwave remote sensing technology has been used in estimating SWE for decades [1] – [3]. Common types of microwave remote sensing missions are satellite missions, airborne campaign, and ground-based campaigns. Estimation of SWE has been carried out through a spaceborne passive remote sensing mission: Advanced Microwave Scanning Radiometer – Earth Observing System (AMSR-E) [4]. Spaceborne active remote sensing missions have received considerable attention recently, for example, algorithms were developed to retrieve SWE from the experimental data of the spaceborne mission COSMO-Skymed [5]. The Cold Regions Hydrology High-Resolution Observatory (CoReH2O) was a proposed satellite mission making measurement of water storage on land surfaces and in glaciers globally. This mission would provide observations at fine spatial resolution scales, and thus offer the potential to retrieve SWE at such high resolutions. The mission was one of the three candidate missions considered for the 7th Earth Explorer by ESA (European Space Agency) [6]. The mission was not selected by ESA in March 2013. Feasibility studies of CoReH2O were performed between 2009 and 2013. Airborne radar called SnowSAR, operating at the same set of frequencies, was deployed [2] [3]. In addition, NoSREx (Nordic Snow Radar Experiment) campaign was initiated in autumn 2009 by ESA, and it covered three snow seasons until the summer of 2012. The campaign site was located at Sodankylä, northern Finland, representing a typical boreal forest/taiga landform, where an average of the maximum of 80 cm snow

accumulation can be expected. The aim of the campaign was to provide data for algorithm development, by measuring the microwave signature of snow covered terrain over several winter seasons. In this campaign, ground based scatterometer measurements using an ESA owned instrument (SnowScat) from a fixed site were performed, covering several winter seasons. SnowScat is a ground based fully polarimetric scatterometer operating in the range of 9 – 18 GHz [2]. The scatterometer observations cover a wide range of incident and azimuthal angles. Microwave data were complemented by regular measurements of snow, soil and atmospheric properties, both form automated sensors and manually collected data. Extensive ground measurements were taken of the snow characteristics in northern Finland, including grain size, snow depth, fraction volume (or snow density), and specific surface area [7] [8]. In this study, data from the 2010-2011 winter seasons are applied.

In snow, the ice particles are packed closely together. Since the ice grains are of millimeter and sub-millimeter sizes, there are thousands of ice grains packed within one-wavelength cube at the microwave frequencies from X-band to Ka-band (9 - 37 GHz). As the propagation and scattering of electromagnetic waves are coherent within distances of about a wavelength or more, the ice grains in snow do not scatter independently. In the conventional radiative transfer theory [9] [10], one uses incoherent superposition to add the scattered intensities of different particles. In the Dense Media Radiative Transfer theory (DMRT) [11] [12], the author take into account the collective scattering and wave interaction effects of densely packed ice grains. Conventional scattering theory is based on Rayleigh scattering because the ice grains are much smaller than wavelength at X-band and Ku-band. The Rayleigh theory gives an extinction that is proportional to the 4^{th} power of frequency, and the 3^{rd} power of grain size. The angular dependence of scattering is that of Rayleigh phase function which is the electric dipole scattering pattern with

mean cosine of scattering equal to zero. The theoretical predictions of DMRT show several departures from conventional Rayleigh scattering theory [12] – [16]:

(a) Conventional independent scattering models, such as Rayleigh scattering model, show that the scattering coefficient is proportional to the fourth power of the frequency, when the scattering particles are electrically small. Though ice grain sizes are small at microwave wavelengths, the frequency dependence of dense media scattering is much lower than the conventional theory. The lowest power law of frequency dependence in the simulations so far is 1.7 [13].

(b) For a conglomeration of particles, conventional independent scattering models superimpose the scattering intensity of each particle, independent of each other, to get the total effect. Therefore, the total scattering is linearly proportional to the fraction volume (or density) of the medium. However in dense media such as real snow, scattering is not linearly proportional to the fractional volume (or density of snow). Scattering saturates at high fractional volumes.

(c) In conventional scattering models, the electrically small particles are considered as dipoles. Therefore the scattering patterns are uniform in azimuthal direction, and follow $(\cos\theta)^2$ in the inclined plane. In dense media model, the scattering phase matrices are different from the electric dipole scattering pattern, although ice grains are small. The phase matrices show significantly stronger forward scattering.

(d) In conventional scattering models, there is no cross polarization in scattering when particles are spheres. In the dense media model, the electric dipole interactions of closely packed ice grains result in strong cross polarization in the phase matrices [13].

The author have developed three DMRT models: Analytical Quasi-Crystalline Approximation for densely packed spheres [12] [14] [15], numerical Foldy-Lax multiple scattering equations for densely packed spheres [16], and bicontinuous model for ice grain clusters with Discrete Dipole Approximation (DDA) [13]. QCA is an analytical approximation, while bicontinuous model is based on numerical solutions of Maxwell equations for automatically generated samples of snow microstructures. It is noteworthy that besides QCA, Foldy-Lax, and bicontinuous models, two other models in the literature are MEMLS model which is based on strong fluctuation theory, and the Helsinki University of Technology (HUT) model. Strong permittivity fluctuation theory was developed by using distorted Born approximation [17] [18]. A low frequency approximation is made on the strong permittivity fluctuations. The strong fluctuation theory utilized autocorrelation function and the correlation length. Vallese and Kong [19] studied the autocorrelation functions of real snow and found that they are close to exponential functions. Their results show that the correlation lengths are smaller than 0.5 mm. The approach was subsequently adopted by Stogryn [20] and Matzler [21], and it was confirmed for different snow types from new snow to depth hoar [22] – [26]. Recently strong fluctuation theory was applied to snow cover and SAR data at a single frequency, e.g. X-band [27]. Because of the built-in assumptions, and the measured small correlation length, strong fluctuation theory results are similar to Rayleigh scattering theory. Major results of strong fluctuation theory and Rayleigh theory include: (1) the scattering coefficient is proportional to $f^{4.0}d^{3.0}$ where f is the frequency and d is the grain size, because the correlation length is much smaller than a wavelength at C, X and Ku band. (2) the angular distribution of scattering is the Rayleigh phase function, which is the dipole's scattering pattern. This means that the mean cosine of scattering ($\bar{\mu}$) equals zero. Thus when applying strong fluctuation theory to multi-

frequencies, the frequency dependence is adjusted empirically. The Helsinki University of Technology (HUT) model is based on experimental observation of extinction coefficients. The frequency dependence of extinction is based on empirical fit. The HUT model chooses a scattering phase function with strong forward scattering, and the mean cosine ($\bar{\mu}$) is chosen as 0.96 [28] [29].

The DMRT-QCA and the DMRT-bicontinuous model are applied for data analysis. Two size parameters are used in the implementation of the QCA model and the bicontinuous model. In the QCA model, the two size parameters are grain size diameter $2a$ and stickiness parameter τ. The stickiness parameter represents the aggregation properties of snow grains to form clusters. In the bicontinuous model, the two size parameters are the mean wavenumber $\langle\zeta\rangle$ and the parameter b, related to wavenumber distribution. The mean wavenumber is corresponding to the inverse of the grain size. The second parameter is related to the clustering property. A common feature of QCA and bicontinuous is that strong forward scattering property is exhibited by using the stickiness parameter τ and the parameter b respectively. Bicontinuous model parameters $\langle\zeta\rangle$ and b are also related to snow parameters, such as grain size, auto-correlation function, and Specific Surface Area (SSA). A feature of the bicontinuous model is that it is related to the past models. By varying the b parameter, it gives varied frequency dependence and strong forward scattering as in the DMRT-QCA model [13]. It is also related to the Helsinki University of Technology (HUT) model [28] [29] in that it has strong forward scattering. The bicontinuous model also utilizes correlation functions that are characterized by functional forms and correlation lengths. Thus it is related to the strong permittivity fluctuation model [17] [20] [25].

In implementing DMRT-QCA and DMRT-bicontinuous a multiple layered medium and full multiple scattering solutions are computed using the method of azimuthal harmonic expansions and quadrature discretization of the inclination angles. The differential equations are solved numerically. Rough surface scattering are based on NMM3D (Numerical 3D solutions of Maxwell equations [30] [31].

Measured snow parameters are used as input to the DMRT theory to compute backscattering results which are then compared with the measured backscattering of SnowSAR and SnowScat. The author used DMRT-QCA and DMRT-bicontinuous models to show that both models can utilize the same physical parameters for multi-frequency measurements. The scattering properties of DMRT-QCA and DMRT-bicontinuous are consistent for various dependences of the co-polarized backscattering coefficients. Moreover, the bicontinuous model has the advantages of large cross-polarization [13] and the resemblance to the microstructures of real snow.

In Section 2.2, the QCA model is briefly discussed. The scattering properties of QCA are illustrated using the two size parameters. In Section 2.3, bicontinuous model is briefly discussed. The parameters of the bicontinuous model are then related to the snow physical parameters. In Section 2.4, scattering properties of the bicontinuous model are illustrated using the two size parameters. In Section 2.5, multiple scattering DMRT theory and rough surface effects for active remote sensing are described. In Section 2.6, SnowSAR and SnowScat measurements are described. In Section 2.7, DMRT-QCA model is compared with SnowSAR radar data. In Section 2.8, DMRT-bicontinuous model is compared with SnowScat scatterometer data.

2.2 QUASI-CRYSTALLINE APPROXIMATION MODEL

Under QCA model [11] [12], the particles are assumed to be densely packed and can also adhere together to form aggregates. The sticky particle model has 2 size parameters: particle size $2a$, where a is the radius, and stickiness parameter τ which describes the surface adhesion among the particles. When the particles are randomly packed together, they have a tendency to form clusters and bonds with each other. The adhesive force is parameterized using the stickiness parameter which governs the degree of clustering. In Monte Carlo simulations of particle positions, the author has made use the Metropolis shuffling techniques [11] to create random positions. In addition, the particles are allowed to form bonding and result in aggregation. The parameter τ is used to describe the bonding state [11]. A smaller τ indicates stronger clustering effect, and a larger τ indicates weaker clustering or even non-sticky particles.

Because the grain sizes are much smaller than wavelength at X-band and Ku-band, the classical independent scattering theory will be Rayleigh theory which is the same as Mie theory for small size. The classical results will have frequency dependence to the 4th power, size dependence to the third power, and the Rayleigh phase matrix of electric dipole scattering pattern. The author illustrates scattering properties by varying the stickiness parameter τ.

The angular distribution of phase matrix is described by the mean cosine of scattering $\bar{\mu}$:

$$\bar{\mu} = \frac{\int p(\hat{s},\hat{s}')(\hat{s}\cdot\hat{s}')d\Omega'}{\int p(\hat{s},\hat{s}')d\Omega'} = \frac{\int_0^{\pi} d\Theta \sin\Theta\cos\Theta\,[P_{11}(\Theta)+P_{22}(\Theta)]}{\int_0^{\pi} d\Theta \sin\Theta\,[P_{11}(\Theta)+P_{22}(\Theta)]} \quad (2\text{-}1)$$

For the Rayleigh phase function, $\bar{\mu} = 0$. The stronger the forward scattering is, the larger $\bar{\mu}$ is. When forward scattering is weaker than backward scattering, $\bar{\mu} < 0$. Figure 2-1 illustrates the

phase matrices of QCA model. In the figure the phase matrices are normalized by the scattering coefficient κ_S, given by

$$\kappa_S = \pi \int_0^{\pi} d\Theta \sin\Theta \left[P_{11}(\Theta) + P_{22}(\Theta)\right] \tag{2-2}$$

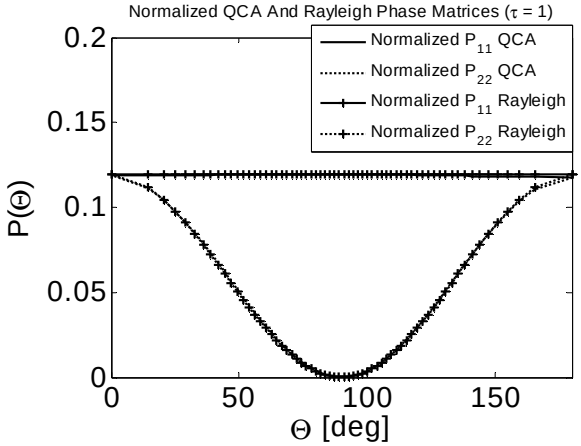

(a)

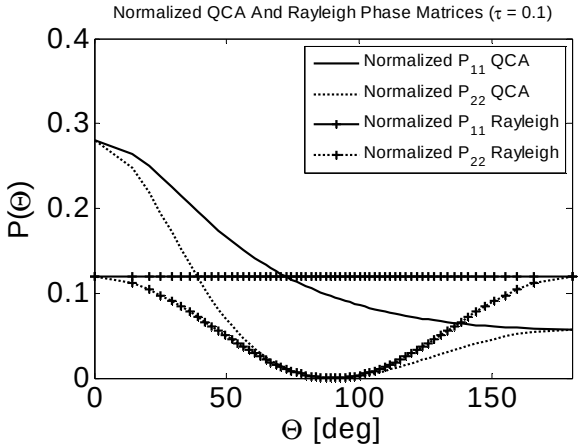

(b)

Figure 2-1 QCA phase matrices showing strong forward scattering.

Frequency = 17.2 GHz; diameter = 1.0 mm; fraction volume = 20%;

(a) QCA stickiness parameter = 1.0 (b) QCA stickiness parameter = 0.1

The phase matrix $P_{21}(\Theta)$ and $P_{12}(\Theta)$ are cross-polarization. They are much smaller than co-polarization and only make small contributions to scattering coefficients and mean cosine. Therefore they are ignored in Equation (2-1) & (2-2). In Figure 2-1, co-polarization phase matrices are plotted against Θ which is the angle between the incident direction and the scattered direction. Thus $\Theta = 0$ is forward scattering and $\Theta = 180^{\circ}$ is backscattering. The 1- 2 frame is based on using the plane formed by the incident and scattered directions [32].

The Rayleigh phase function $P_{11}(\Theta)$ is constant and $P_{22}(\Theta)$ is proportional to $(\cos\Theta)^2$. Figure 2-1(a) illustrates a case with $\tau = 1.0$, and the QCA phase matrices are similar to those of Rayleigh phase matrix. This is because the particles are not that sticky, and particles which are small retain the angular distribution. Figure 2-1(b) is a sticky case with $\tau = 0.1$. It shows strong forward scattering compared with Rayleigh scattering phase matrix. In this case, $1 > \bar{\mu} > 0$.

Figure 2-2 illustrates QCA scattering coefficients (defined in Equation (2-2)) as a function of the diameter of the particles. The two frequencies at X- and Ku-bands are considered. The author compared the two sticky cases. It is seen that scattering coefficient decreases as stickiness parameter τ increases, because small τ indicates stronger stickiness. Therefore stronger sticky effect will lead to stronger scattering effect, because the stickiness parameter has the clustering effects. The aggregates of small particles are “effectively” larger in size than that of the small particle. The frequency dependence and size dependence of QCA scattering coefficients is extracted from Figure 2-2.

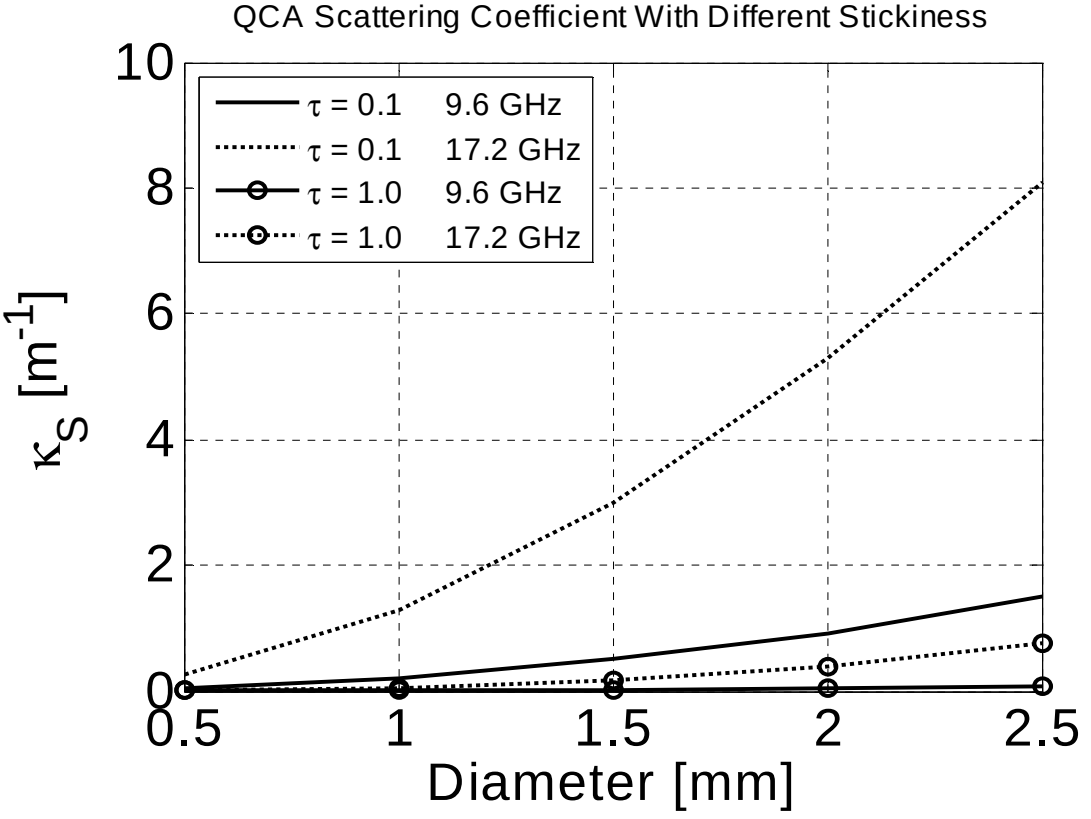

Figure 2-2 Scattering coefficients of QCA model with various stickiness parameter τ

$$\alpha = \log(\kappa_{S2}/\kappa_{S1}) \,/\, \log(f_2/f_1) \quad \text{(2-3a)}$$

$$\beta = \log\left(\kappa_S^{(2)}/\kappa_S^{(1)}\right) / \log(d_2/d_1) \quad \text{(2-3b)}$$

where α is the frequency dependence, β is the size dependence. The computed results are shown in Table 2-1. For the sticky case $\tau = 0.1$, the frequency dependence is 2.9 when the diameter is 2.5 mm. At 17.2 GHz, the size dependence is 1.9 when the diameter is 1.5 mm or 2.0 mm. These results are lower than 4th power frequency dependence and 3rd power size dependence. A weaker sticky case $\tau = 1.0$ is also shown in Table 2-1. The frequency dependence is 4.0, and the size dependence is 3.0 for all cases.

Table 2-1 Frequency dependence, and sizedependence at Ku-band.

Extracted from QCA data in Figure 2-2

Diameter [mm]		0.5	1.0	1.5	2.0	2.5
Frequency dependence	$\tau = 0.1$	3.6	3.3	3.1	3.0	2.9
	$\tau = 1.0$	4.0	4.0	4.0	4.0	4.0
Size dependence (17.2 GHz)	$\tau = 0.1$	2.3	2.0	1.9	1.9	
	$\tau = 1.0$	3.0	3.0	3.0	3.0	

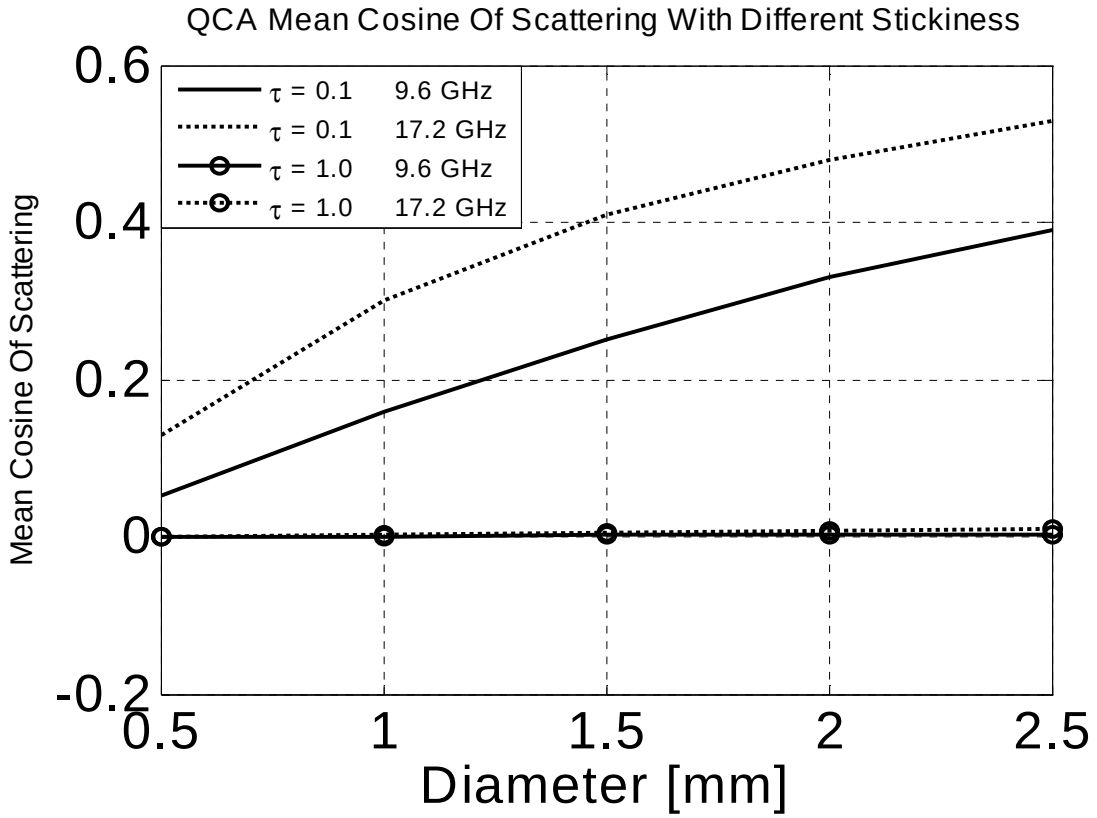

Figure 2-3 Mean cosine of scattering $\bar{\mu}$ of QCA model with various stickiness parameter

Figure 2-3 illustrates the mean cosine of scattering $\bar{\mu}$ for QCA model for two frequencies and two sticky cases. It is seen that QCA model will create moderately large $\bar{\mu}$ if $\tau = 0.1$. When the

diameter is 2.5 mm, the mean cosine of scattering is 0.39 at 9.6 GHz, and 0.53 at 17.2 GHz. At both two frequencies, as the stickiness parameter τ increases to 1.0, the mean cosine of scattering will decrease to 0.011 or lower. Thus stronger sticky effects of the particles make larger $\bar{\mu}$, and stronger forward scattering.

In the HUT model [28] [29], a strong forward scattering of mean cosine $\bar{\mu} = 0.96$ is assumed. Using the QCA model, with mean grain size of 1 mm, and with the smallest stickiness parameter allowed ($\tau > 0.093$), the mean cosine of scattering is 0.70 at frequency of 17.2 GHz. The mean cosine is moderately large in QCA but not as large as in the HUT model.

2.3 GEOMETRIC DESCRIPTION OF BICONTINUOUS MODEL

2.3.1 Generation algorithm and model parameters

Recently, DMRT-bicontinuous model has been proposed for analysis of signatures of microwave remote sensing of snow [13] [33]. It combines numerical 3D solutions of Maxwell equations with the automatic generations of realistic microstructures of snow. The bicontinuous model is based on a continuous representation of interfaces between different phases or domains within the medium [34]. Figure 2-4 illustrates examples of automatically generated images of snow using the bicontinuous model. The shapes are irregular and there are clustering effects. The automatically generated snow microstructures resemble that of natural snow.

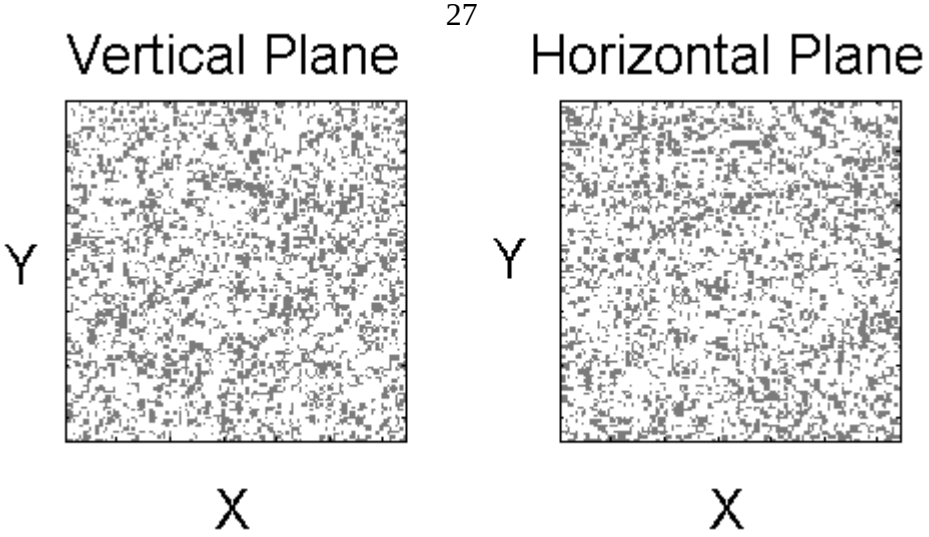

Figure 2-4 Typical automatically generated snow structure: bicontinuous model.

Total size: 6.4 cm * 6.4 cm

To generate the bicontinuous medium automatically, the author divided the sample into cubic grids. For each realization, the bicontinuous medium is generated by the following algorithm. Let

$$S(\bar{r}) = \frac{1}{\sqrt{N}} \sum_{n=1}^{N} \cos(\bar{\zeta}_n \cdot \bar{r} + \varphi_n) \tag{2-4}$$

where $\bar{r}$ is the position variable for the center of each cubic grid of the bicontinuous medium. The random function $S(\bar{r})$ at each grid $\bar{r}$ is generated stochastically by choosing a large number N. In Equation (2-4), the wave vector $\bar{\zeta}_n$ and the phase φ_n are independent random variables. The phase φ_n is uniformly distributed between 0 and 2π, and the unit vector $\bar{\zeta}_n$ is uniformly distributed on a unit spherical surface. The magnitude of the wave vector ζ_n is distributed between 0 and $+\infty$ and has a probability density function $p(\zeta)$. A variety of distributions can be used. The author chose to use the Gamma distribution:

$$p(\zeta) = \frac{1}{\Gamma(b+1)} \frac{(b+1)^{b+1}}{\langle \zeta \rangle} \left(\frac{\zeta}{\langle \zeta \rangle} \right)^{b} \exp\left[-(b+1) \frac{\zeta}{\langle \zeta \rangle} \right] \quad (2\text{-}5)$$

After all the random variables are generated, the random function $S(\bar{r})$ is computed at each grid point $\bar{r}$ by Equation (2-4). Then a cutting level α is introduced to determine the space filling in each cube of the bicontinuous medium.

$$\alpha = \mathrm{erf}^{-1}(1 - 2f_V) \quad (2\text{-}6)$$

Where $\mathrm{erf}^{-1}(\cdot)$ is the inverse error function. For every point $\bar{r}$

$$\Theta_\alpha(\bar{r}) = \begin{cases} 1, S(\bar{r}) > \alpha \\ 0, S(\bar{r}) < \alpha \end{cases} \quad (2\text{-}7)$$

$\Theta_\alpha(\bar{r}) = 1$ is corresponding to filling with ice in the cube where $\bar{r}$ locates, while $\Theta_\alpha(\bar{r}) = 0$ is corresponding to filling with air in the cube.

The distribution of wavenumbers has the mean and the standard deviation. Thus as constructed in the algorithm above, the bicontinuous distribution has two parameters: the mean wavenumber $\langle \zeta \rangle$ and the parameter b. The b parameter controls the width of the distributions and is related to the standard deviation. The mean wavenumber $\langle \zeta \rangle$ is corresponding to the inverse of the prevailing grain size.

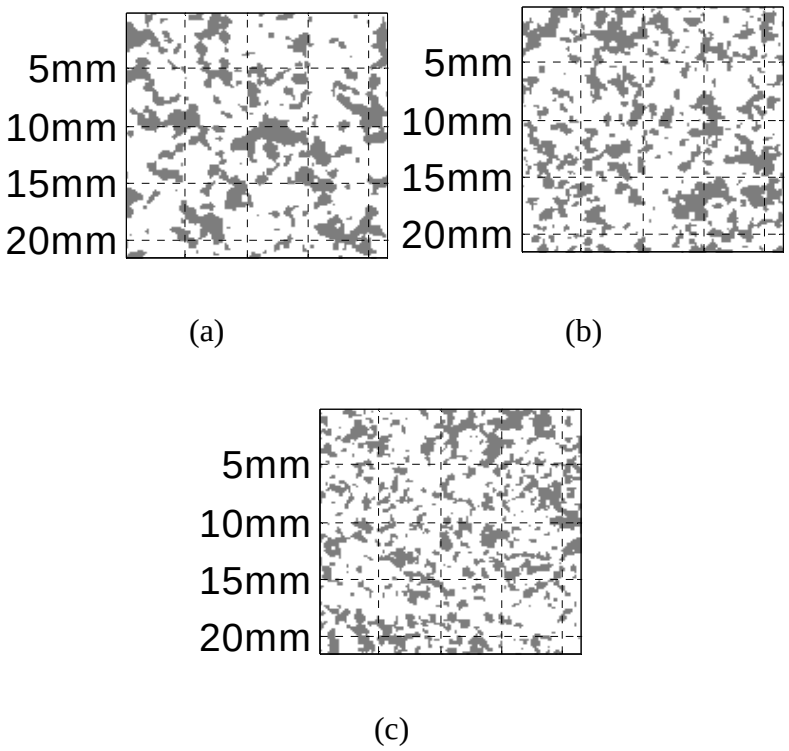

Figure 2-5 Bicontinuous medium: various $\langle\zeta\rangle$, $b = 1.5$, $f_V = 0.3$

(a) $\langle\zeta\rangle = 3500\ [m^{-1}]$ (b) $\langle\zeta\rangle = 4500\ [m^{-1}]$ (c) $\langle\zeta\rangle = 5500\ [m^{-1}]$

Figure 2-5 show realizations of the microstructures of bicontinuous medium with the same b and various mean wavenumbers $\langle\zeta\rangle$. As $\langle\zeta\rangle$ increases, the prevailing size in the generated structure decrease. The three result microstructures structures in Figure 2-5 are similar but with different sizes of grains. Figure 2-6 illustrates bicontinuous medium with the same mean wavenumber $\langle\zeta\rangle$ and various b. From the figures, the author sees clustering in the microstructures. Decreasing the b parameter increases the clustering. The parameter b has the role of a clustering parameter with smaller b corresponding to more clustering. In Figure 2-6(a), $b = 0.5$ and grains aggregate to form effectively larger grains because of the clustering effect.

Thus QCA and bicontinuous models have similar physical concepts. In QCA stickiness parameter τ is used to represent aggregation, while in the bicontinuous model the parameter b plays the role of clustering effects.

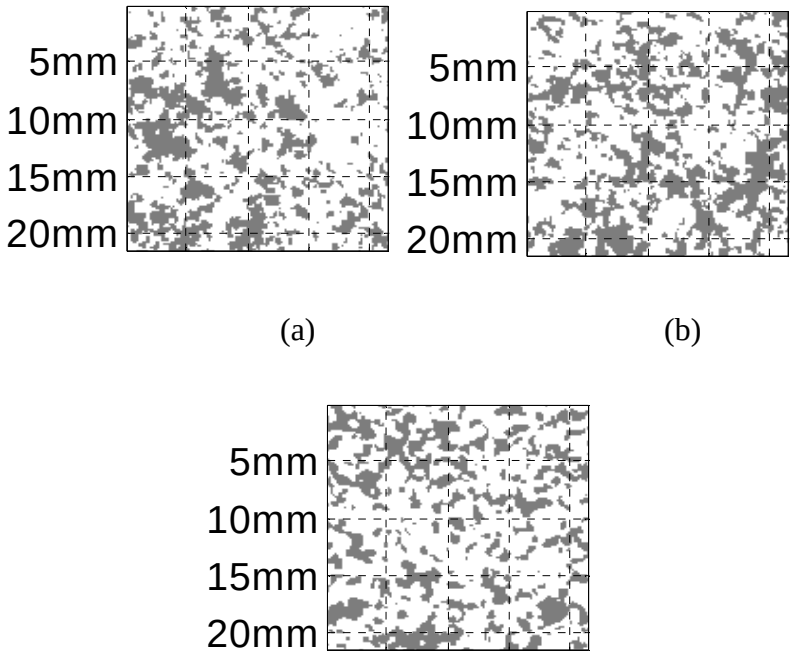

(a) (b)

(c)

Figure 2-6 Bicontinuous medium: various b, $\langle\zeta\rangle = 4500\ [m^{-1}]$, $f_V = 0.3$

(a) $b = 0.5$ (b) $b = 1.0$ (c) $b = 2.0$

2.3.2 Auto correlation function

The auto correlation function has been studied extensively in the context of distorted Born approximation for random media [35], and strong permittivity fluctuations [17] [20] [25]. In the early work, a correlation function is used to describe the random permittivity fluctuations [19]. Vallese and Kong [19] performed the extraction from several photographs of a vertical cross-sectional slice of a snow pile. The photographs were obtained from the microtomed slice of a

casted snow sample. The images were digitized and then assumed with discrete permittivity of ice or air. The cross correlation of a reference sub-image with the entire image was computed as the correlation function. They found that the correlation functions are exponential in character. Vallese and Kong [19] concluded that the random permittivity fluctuations could be described by its mean, variance and correlation lengths, and the correlation lengths are corresponding to the average particle dimensions in snow.

In the bicontinuous model an analytical expression of the auto correlation function was derived [13]:

$$ACF(d) = \sum_{n=1}^{+\infty} C_n(\alpha)[C_S(d)]^n \tag{2-8}$$

Where α is the cutting level of the bicontinuous generation algorithm, and is directly related to the fraction volume, as shown by Equation (2-6). The coefficients $C_n(\alpha)$ in Equation (2-8) are given by

$$C_n(\alpha) = \frac{\exp(-2\alpha^2)\,[H_{n-1}(\alpha)]^2}{\pi n!\, 2^n} \tag{2-9}$$

Where $H_n(\cdot)$ is the Hermite polynomial. $C_S(d)$ is given by

$$C_S(d) = (\cos\varphi)^{b+1}\,\frac{\sin(b\varphi)}{b\sin\varphi} \tag{2-10}$$

Where $\varphi = \arctan\frac{\langle\zeta\rangle d}{b+1}$. Figure 2-7 illustrates the correlation functions for mean wavenumber $\langle\zeta\rangle = 5000\ [m^{-1}]$ and for two different b. The exponential correlations functions are shown for comparison. On a linear scale (Figure 2-7(a)), the correlation functions of bicontinuous model resemble that of exponential correlation functions. However, when the correlation functions are

plotted in a logarithm scale (Figure 2-7(b)), it will show stronger correlation for distances larger than 1 mm. This becomes even clearer as the parameter b decreases.

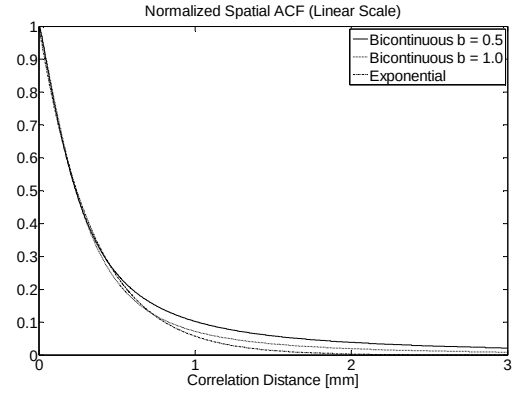

(a)

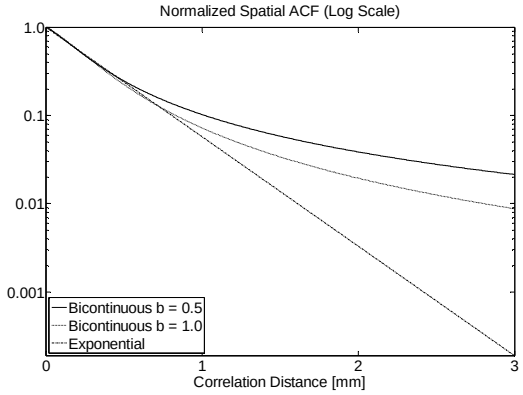

(b)

Figure 2-7 Auto correlation function of bicontinuous model with various parameter b.

$\langle\zeta\rangle = 5000\ [m^{-1}]$, $f_V = 0.2$ (a) Linear scale (b) Log scale

The author also analyzed the spectral density, $W(\bar{k})$ is the 3-D Fourier transform of the auto correlation function, while $W(k_z)$ is the corresponding 1-D auto-correlation function derived from $W(\bar{k})$

$$W(\bar{k}) = \frac{1}{(2\pi)^3}\int_{-\infty}^{+\infty} dx \int_{-\infty}^{+\infty} dy \int_{-\infty}^{+\infty} dz\, ACF(\bar{d}) \exp(-j\bar{k}\cdot\bar{d}) \quad \text{(2-11a)}$$

$$W(k_z) = \frac{1}{2\pi^2 k_z}\int_{0}^{+\infty} drr \sin(k_z r)\, ACF(r) \quad \text{(2-11b)}$$

To obtain the spectral density function, one needs to carry out the integration to a larges upper limit. This accounts for the effects of clustering property that is contained in the correlation function for large r beyond the correlation length. Figure 2-8 illustrates the spectral density using the same parameters as Figure 2-7. The bicontinuous model's spectral density is larger than that of exponential correlation function when the wavenumber k <2000 $[m^{-1}]$. This indicates the presence of clustering effect that is not in the exponential correlation function. As the parameter b decreases, the clustering effect becomes clearer, and the difference from exponential correlation function is larger.

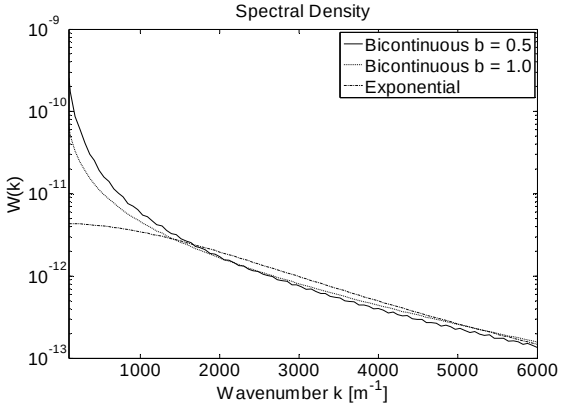

Figure 2-8 Spectral density function of bicontinuous model with various parameter b

$$\langle\zeta\rangle = 5000\ [m^{-1}],\ f_V = 0.2$$

The author defined the correlation length l as

$$l = ACF^{-1}(e^{-1}) = ACF^{-1}(0.37) \quad (2\text{-}12)$$

Where $ACF^{-1}(\cdot)$ is the inverse function. Therefore, by using bicontinuous model, the correlation length is extracted. However, it is important to note that two size parameters are used and the correlation length alone cannot adequately describe the microstructure of snow. The correlation length defined in this manner will only correspond closely to the inverse of the mean wavenumber. The extraction of the parameter b from real snow samples will be a challenge in future studies.

2.3.3 Specific Surface Area (SSA)

SSA is surface area per unit mass (m^2/kg or cm^2/g) or surface area per unit volume (m^{-1}). It is used to characterize snow microstructures. Common techniques of measuring SSA include: methane adsorption at 77 K [36], X-ray tomography [37], snow reflectance at short-wave infrared (SWIR) [38] [39], etc. For bicontinuous model, SSA is computed analytically [13]:

$$SSA = \frac{1}{\rho_{ice}} \frac{\exp(-2\alpha^2)}{f_V} \frac{2\langle\zeta\rangle}{\pi\sqrt{3}} \sqrt{1 + \frac{1}{b+1}} \quad (2\text{-}13)$$

Where ρ_{ice} is the density of ice. Note that SSA in Equation (2-13) is defined as surface area per unit mass. In addition to using the analytic expression, the author also computed SSA numerically by using the automatically generated snow samples and counting the surface areas. In the numerical procedure, the samples are divided into small cubes of air and small cubes of ice. Each surface on an ice cube, which is in direct contact with an air cube, is counted in the total surface area. Table 2-2 shows the SSA for various parameter b. Both analytical SSA (Equation (2-13)) and numerical SSA are shown. As parameter b decreases, size distribution

becomes broader, thus the small particles will contribute to the increasing surface area. It is noted counting surface areas in the manner is dependent on the size of discretization. The discretization size that the author used is based on the microwave wavelength. Thus the SSA counted in this manner is corresponding to a "microwave view" of SSA of the snow sample.

The bicontinuous parameters are related to ground truth data. The descriptors of the bicontinuous medium include autocorrelation functions and specific surface areas, both of which can be computed from the parameters $\langle\zeta\rangle$ and b. On the other hand, specific surface areas and correlation functions can be derived from digitization of real snow microstructures. The parameter b is related to grain size distribution which can be observed in ground measurements. The author has chosen the Gamma distribution, and defined parameter b of Gamma distribution as the wavenumber distribution parameter. The rigorous relation of the parameter b to grain size distribution is a subject of continual studies.

Table 2-2 SSA comparison among various parameter b.

$$\langle\zeta\rangle = 5000\ [m^{-1}],\ f_V = 20\%$$

b	0.5	1.0	1.5
Numerical $[cm^2/g]$	57.0	56.6	53.9
Analytical $[cm^2/g]$	63.5	60.2	58.2

2.4 SCATTERING PROPERTIES OF BICONTINUOUS MODEL

The author illustrated the scattering properties of bicontinuous model include scattering coefficient, mean cosine of scattering, and phase matrix. Figure 2-9 illustrates the bicontinuous

scattering coefficients against b parameters. As b decreases, the clustering effect becomes stronger and aggregation effects are stronger, thus the scattering coefficient becomes larger. Results in two frequencies are shown. The frequency dependences of bicontinuous model are extracted and listed in Table 2-3. When parameter $b = 0.01$, the frequency dependence between 9.6 GHz and 17.2 GHz is 2.4. As b increases to 2.0, the frequency dependence increases to 4.0, which indicates the clustering effect becomes weaker.

Table 2-3 Frequency dependence between 9.6 and 17.2 GHz of bicontinuous model.

$$\langle \zeta \rangle = 5000\ [m^{-1}],\ f_V = 20\%$$

b	0.01	0.5	1.0	1.5	2.0
Frequency dependence	2.4	2.7	3.2	3.8	4.0

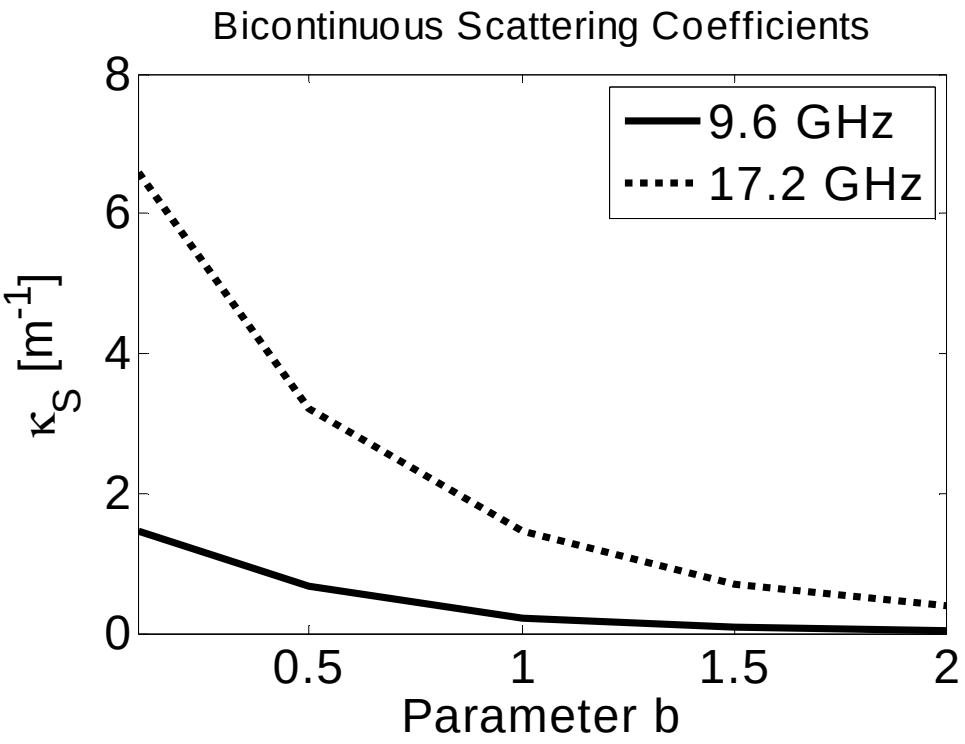

Figure 2-9 Bicontinuous scattering coefficients against parameter b for two frequencies

$\langle\zeta\rangle = 5000\ [m^{-1}]$, $f_V = 20\%$

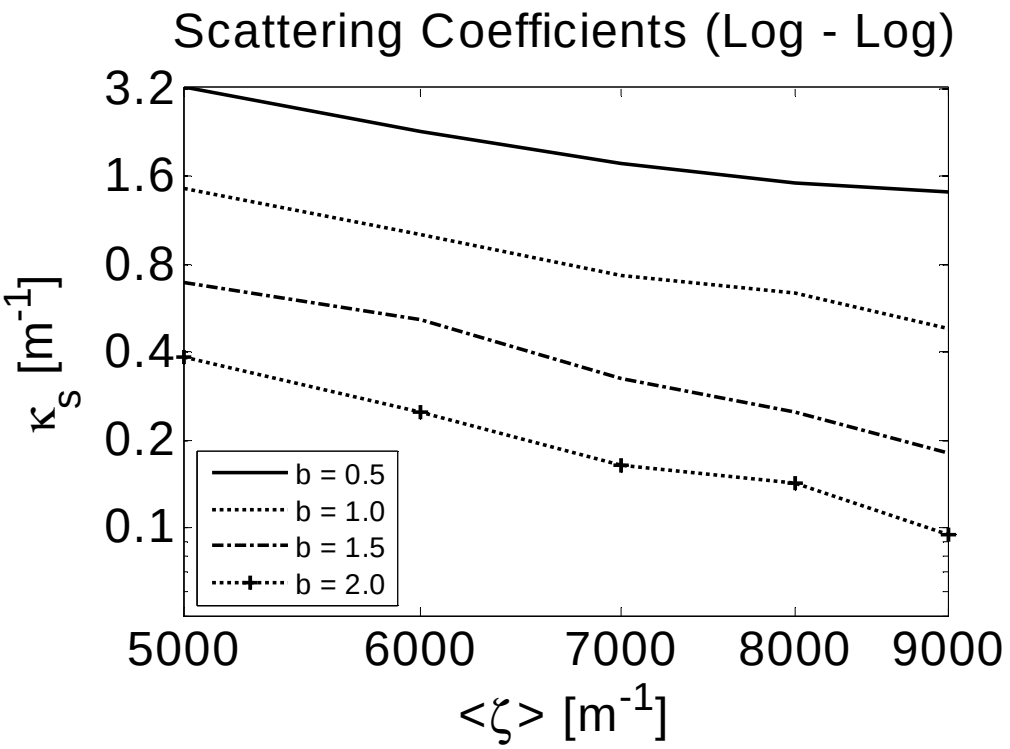

Figure 2-10 Bicontinuous scattering coefficients vs. the mean wavenumber for vairous *b* parameter.

Frequency = 17.2 GHz; fraction volume = 20%. Plotted in double-log scale.

Figure 2-10 illustrates the scattering coefficients against the mean wavenumber $\langle\zeta\rangle$ for various *b*. It is seen that scattering coefficients decrease as the mean wavenumber increase, because the mean wavenumber relates to the inverse of grain size. In addition, the scattering coefficients decrease as *b* parameter increases, because the clustering effect becomes weaker. Another important feature of Figure 2-10 is the $\langle\zeta\rangle$ dependence, or the scattering coefficient's power law with respect to $\langle\zeta\rangle$. Now that $\langle\zeta\rangle$ relates to the inverse of grain size, the $\langle\zeta\rangle$ dependence will indicate the size dependence property of bicontinuous model. To compute the dependence, two

mean wavenumbers $\langle\zeta\rangle_1 = 5000[m^{-1}], \langle\zeta\rangle_2 = 9000[m^{-1}]$ are considered. By using the same method as QCA model (Equation (2-3)), the $\langle\zeta\rangle$ dependences are shown in Table 2-4. All the results are negative, which comes from the inverse relationship between $\langle\zeta\rangle$ and grain size. It is seen that when $b = 0.5$, clustering effect is strong, thus the $\langle\zeta\rangle$ dependence is -1.4; when $b = 2.0$, clustering effect is weak, thus the $\langle\zeta\rangle$ dependence is -2.4. All the results are larger than -3.0. The size dependence of Rayleigh scattering model is 3.0, and the inverse dependence is -3.0.

Table 2-4 $\langle\zeta\rangle$ dependence of bicontinuous model.

Frequency = 17.2 GHz, fraction volume = 20%

b	0.5	1.0	1.5	2.0
$\langle\zeta\rangle_1 = 5000[m^{-1}], \langle\zeta\rangle_2 = 9000[m^{-1}]$	-1.4	-1.9	-2.3	-2.4

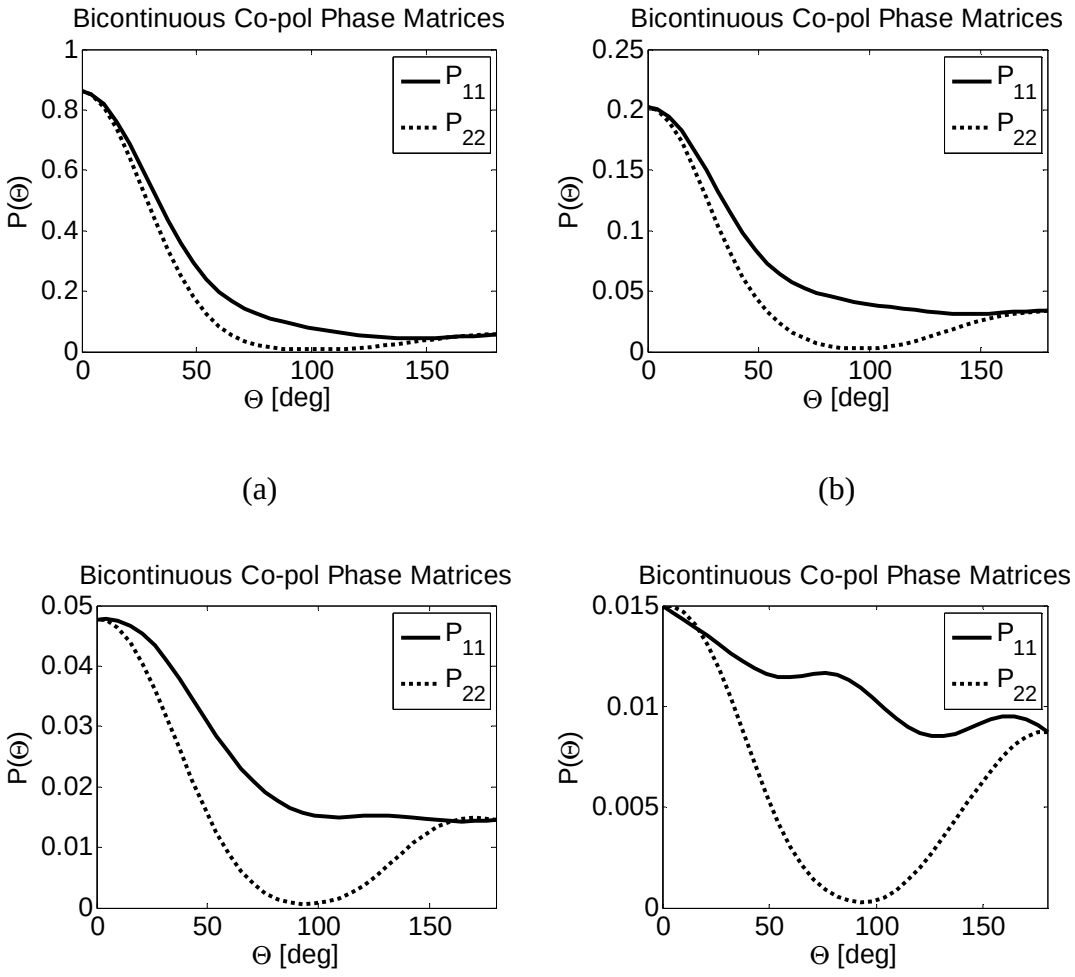

Figure 2-11 Bicontinuous phase matrix with different parameter b at 9.6 GHz.

$$\langle\zeta\rangle = 5000\ [m^{-1}],\ f_V = 20\%$$

(a) $b = 0.1$ (b) $b = 0.5$ (c) $b = 1.0$ (d) $b = 1.5$

In Figure 2-11, the author showed the phase matrices at X-band for various b parameters. The mean wavenumber and the fraction volume are fixed at $\langle\zeta\rangle = 5000[m^{-1}], f_V = 20\%$. As parameter b decreases, the phase matrix becomes larger at $\Theta = 0$ or forward scattering direction. Figure 2-12 illustrates the mean cosine of scattering of bicontinuous model, using the same

parameters as Figure 2-11. $\bar{\mu}$ decreases as parameter b increases, which indicates stronger clustering effect will create stronger forward scattering. No matter how small b is, $\bar{\mu}$ does not exceed 0.6. Thus bicontinuous model will provide only moderately strong forward scattering.

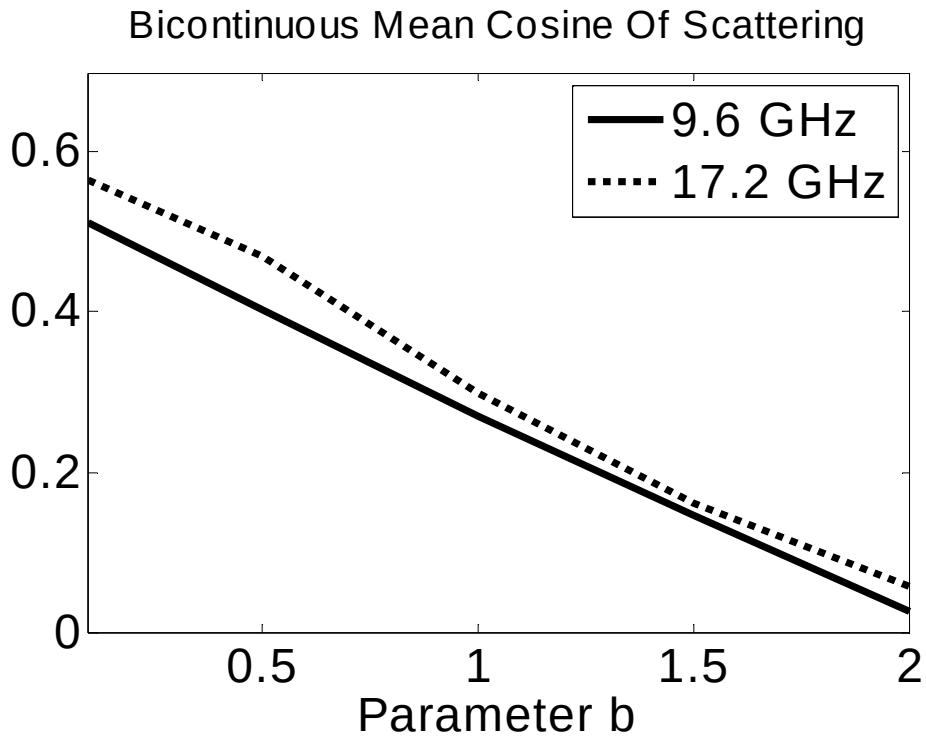

Figure 2-12 Mean cosine $\bar{\mu}$ of bicontinuous model against various parameter b

$$\langle\zeta\rangle = 5000\ [m^{-1}],\ f_V = 20\%$$

2.5 MULTILAYER DMRT MODEL WITH FULL MULTIPLE SCATTERING EFFECTS AND ROUGH SURFACE EFFECTS

In the previous work [15], the multiple scattering effect is considered for single-layer snow. To include multiple scattering in a multilayer structure, the specific intensity is decomposed into reduced intensity and diffused intensity. Reduced intensities are solved analytically, and diffused intensities is expressed in Fourier series in the azimuthal direction:

$$\bar{I}^{(D)}(\theta,\varphi,z)=\bar{I}_0^{(D)}(\theta,z)+\sum_{m=1}^{M_{max}}\bar{I}_{mc}^{(D)}(\theta,z)\cos[m(\varphi-\varphi_{inc})]+\sum_{m=1}^{M_{max}}\bar{I}_{ms}^{(D)}(\theta,z)\sin[m(\varphi-\varphi_{inc})] \quad (2\text{-}14)$$

Each Fourier harmonic $\bar{I}_0^{(D)}(\theta,z),\bar{I}_{mc}^{(D)}(\theta,z),\bar{I}_{ms}^{(D)}(\theta,z)$ is solved by the eigen-quadrature approach. The eigen-quadrature approach is based on the boundary conditions at each interface between different layers:

$$\bar{I}_i^{(up)}(\theta_i,-d_i)=\bar{\bar{R}}_{i,i+1}(\theta_i)\bar{I}_i^{(down)}(\theta_i,-d_i)+\bar{\bar{T}}_{i+1,i}(\theta_{i+1},\theta_i)\bar{I}_{i+1}^{(up)}(\theta_{i+1},-d_i)$$

$$\bar{I}_{i+1}^{(down)}(\theta_{i+1},-d_i)=\bar{\bar{R}}_{i+1,i}(\theta_{i+1})\bar{I}_{i+1}^{(up)}(\theta_{i+1},-d_i)+\bar{\bar{T}}_{i,i+1}(\theta_i,\theta_{i+1})\bar{I}_i^{(down)}(\theta_i,-d_i) \quad (2\text{-}15)$$

Where $\bar{\bar{R}}$ is the reflection coefficient matrix between two layers, $\bar{\bar{T}}$ is the transmission coefficient matrix between two layers. θ_i,θ_{i+1} are quadrature angles, and they are not identical in different layers, due to Snell's law. Thus an interpolation matrix should be added in front of $\bar{\bar{T}}$ matrix when Equation (2-15) is combined into a large matrix equation.

Rough surface scattering is computed by NMM3D implemented with the Method of Moments (MoM) [30] [31]. The snow-ground interface is modeled as a Gaussian random rough surface with exponential correlation function.

Finally volume scattering and surface scattering are combined in an additive way:

$$\sigma_0=\sigma_{VOL}+\sigma_{SURF}\exp(-2\kappa_e d\sec\theta_i) \quad (2\text{-}16)$$

Where σ_0 is the total backscattering, σ_{VOL} is the volume scattering obtained from multilayer DMRT model, σ_{SURF} is the surface scattering obtained by NMM3D , κ_e is the extinction

coefficient including scattering effect and absorption effect, d is the snow depth, and θ_i is the incident angle.

2.6 SNOWSAR AND SNOWSCAT EXPERIMENTS DESCRIPTION

2.6.1 SnowScat

The ESA SnowScat instrument is a frequency scanning (X to Ku band), tower-based scatterometer. For the NoSREx campaign, the instrument was mounted on a tower at the height of ca. 9 meters, allowing the measurement of snow in a forest opening. Any significant vegetation (small trees, shrubs) were removed from the clearing prior to measurements. The remaining low surface vegetation consisted of lichen and moss. According to a soil survey performed in 2010, the soil consisted of a thin organic layer (5-10 cm) overlying a coarse sandy soil (70% sand, 29% silt, 1% clay).

The routine measurements using SnowScat, performed every four hours, covered incident angles between 30 and 60 degrees at 10 degree intervals. To reduce effects of random speckle from natural variability of the snowpack and the soil background, each incident angle was covered by a scan over 17 discrete azimuth directions. Radar backscattering coefficients at four polarizations (HH, HV, VH, and VV) of snow backscattering coefficients were measured. SnowScat measurements were processed to three discrete bands of 2 GHz, with centre frequencies at 10.2, 13.3 and 16.7 GHz.

In situ measurements consisted of automated sensor data and manual snow pit measurements. The automated observations provided information on soil moisture, soil and snow temperature, snow depth and SWE, and weather conditions. Manual snow pit measurements were made at the

immediate vicinity of the microwave observations on a weekly basis. The measured properties included bulk SWE and density, snow stratigraphy (layering), and profiles of snow grain size, density, temperature and moisture. Snow stratigraphy was first determined visually and by testing the hardness of the snow. Snow density was measured as a profile in 10 cm increments using a manual snow scale. The temperature profile was recorded similarly at 10 cm intervals using a digital thermometer. Measuring the exact snow grain size has uncertainties in field conditions; for the NoSREx dataset, macro-photographs of snow grains, taken against a reference grid, were used to determine the typical grain size of each detected snow layer. A photograph of a snow sample, extracted from each layer, was taken and evaluated in laboratory conditions. The grain size was determined as the maximum diameter of prevailing grains [41]. Also the grain type was determined visually. It is acknowledged that large uncertainties are related to this type of classification; the estimation of grain size is prone to observer bias, especially regarding the choice of prevailing grains in the snowpack. Moreover, the snow grain size determined in this way may not be the only option [26]. Therefore, the measured snow grain size is treated in this study as a proxy of the snow microstructure in simulations.

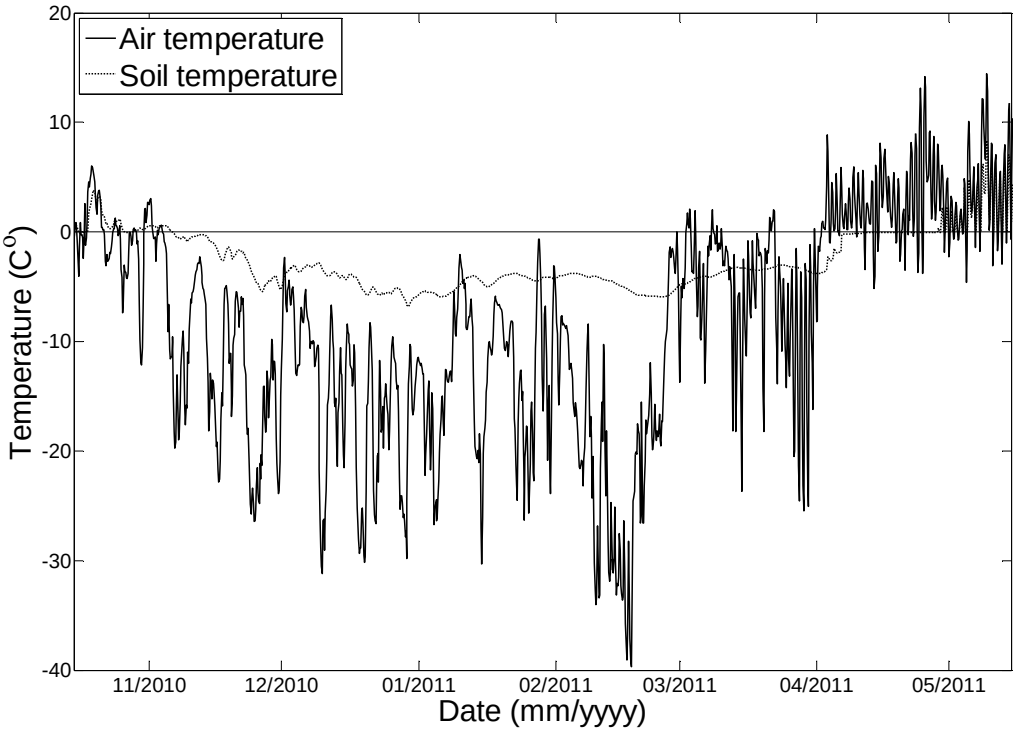

Figure 2-13 Air temperature and soil temperature (at 2 cm depth) measured at the SnowScat site in Sodankylä, Finland, in the winter season of 2010-2011.

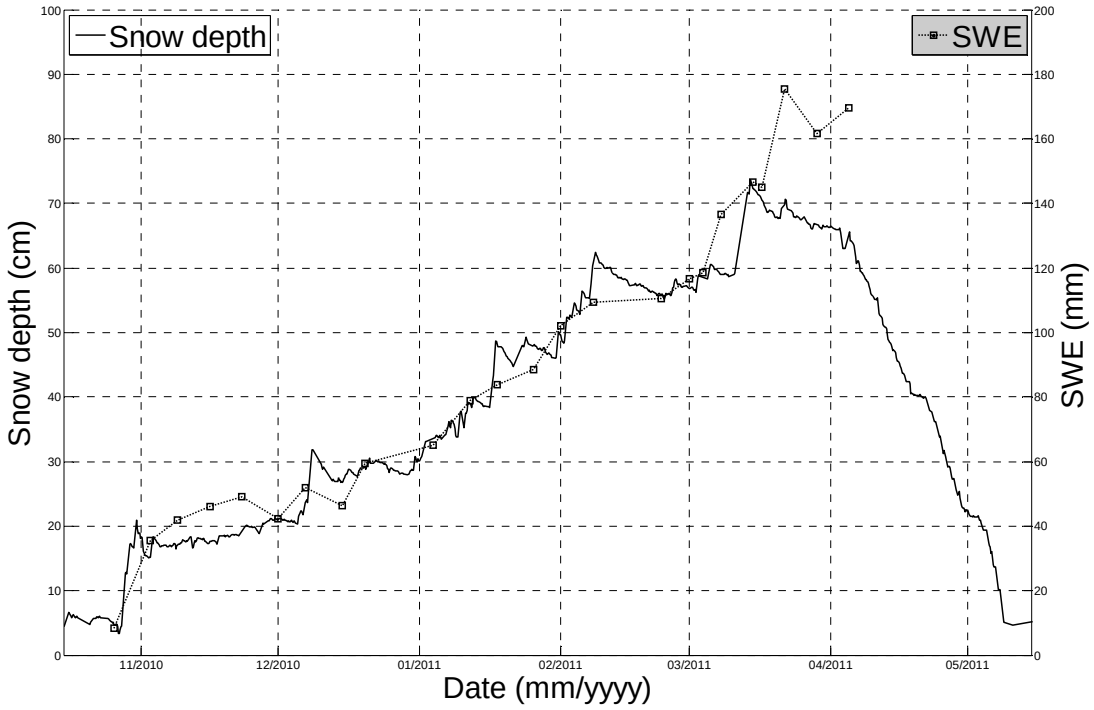

Figure 2-14 Snow depth and SWE measured at the SnowScat site in Sodankylä, Finland, in the winter season of 2010-2011. Snow depth was measured by an automated sensor. SWE was measured weekly using a manual snow scale.

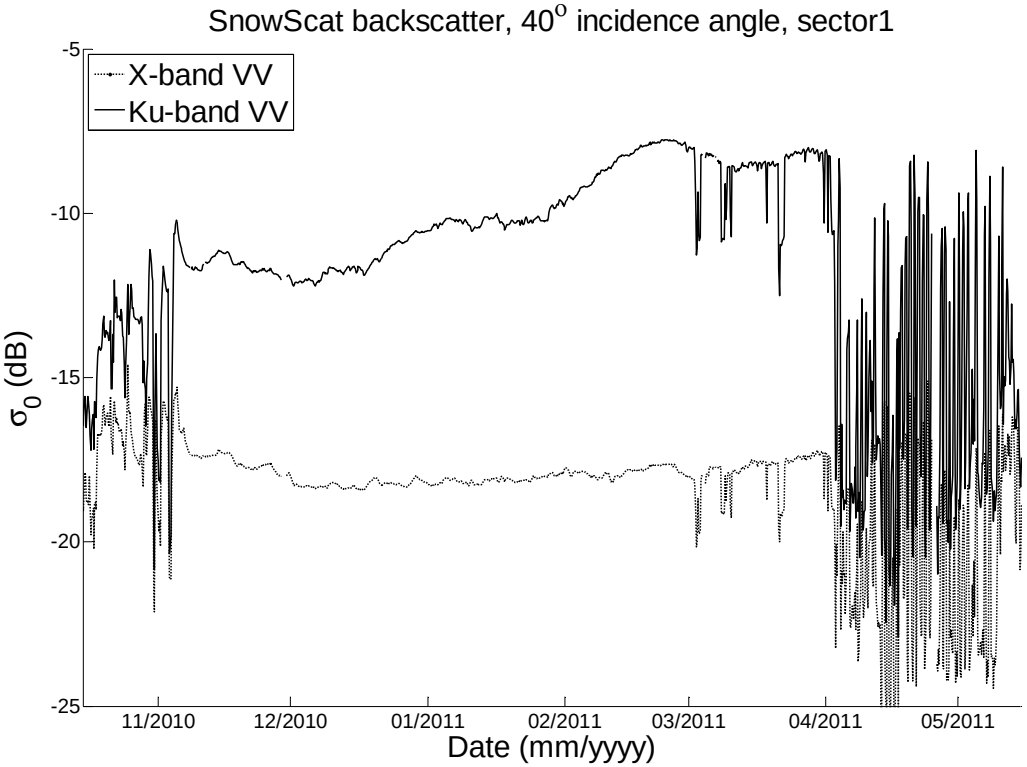

Figure 2-15 Radar backscattering coefficients measured by the SnowScat instrument at co-polarization, 40 °incidence angle for X (10.2 GHz) and Ku (16.7 GHz) bands. Average of 17 azimuth looks.

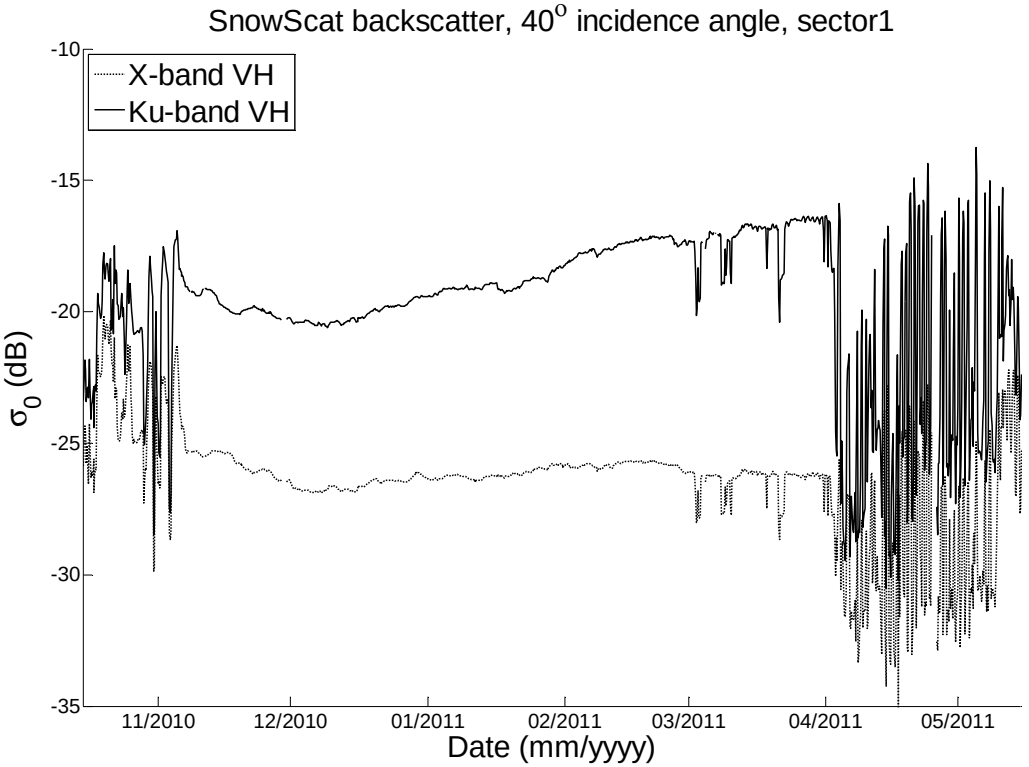

Figure 2-16 Radar backscattering coefficients measured by the SnowScat instrument at cross-polarization, 40 °incidence angle for X (10.2 GHz) and Ku (16.7 GHz) bands. Average of 17 azimuth looks.

For analysis, data from eight snowpits between Jan 4th and March 1st were chosen. During this period, air temperatures remained below zero, which is shown in Figure 2-13. Snow depth, shown in Figure 2-14, increased from ca. 30 cm (61 mm SWE) to ca. 60 cm (114 mm SWE). During this period, the measured backscattering coefficients at co-polarization, shown in Figure 2-15, changed from -10.2 to -7.9 dB and from -18.2 to -18.1 dB at Ku and X-band, respectively. At cross-polarization, shown in Figure 2-16, the change was from -19.3 to -17.3 and from -26.3 to -26.1 at Ku and X-band, respectively. The measured backscattering coefficients signal shows features in November 2010, which cannot be directly connected with increasing snow mass. A

distinct feature observed in SnowScat backscattering coefficients was a gradual decrease of backscattering intensity after an initial rapid increase in the early season. This can be attributed to a combination of changes in soil properties, as well as the gradual relaxation of crust structures in snow, formed during melt-refreeze events, to more typical late-winter snow. Several melt-refreeze events occurred in the early season in October / November 2010; the effect can be seen as rapid decrease (during melt) followed by a rapid increase (during refreezing) of the measured backscattering in Figure 2-15 and Figure 2-16. Gradual relaxation followed each refreeze event; the last event in early November was followed by sub-zero temperatures until March 2011, with decreasing backscattering coefficients until December 2010. The observed decrease in backscattering coefficients is also consistent with decreasing permittivity of the soil due to freezing; residual soil moisture was measured by dielectric sensors at the site until December 2010. It is thus likely that both factors contributed to the detected signatures. After December 2010, a steady increase in the backscattering signal can be linked to the increasing snow mass at Ku band. For X-band, any increase in backscattering coefficients is too weak to be significant.

2.6.2 SnowSAR

During the second and third snow seasons, a mini-SAR airborne system SnowSAR was also deployed to collect data over the Sodankylä area. The SnowSAR operates at mean incident angle of 40 degree with dual-frequency (X band 9.6 GHz, Ku band 17.25 GHz) and dual polarization (VV and HV). At the designated flight altitude, SnowSAR had a swath width of 400 m; data was provided both at 2 m and 10 m resolutions. The first SnowSAR acquisition, applied in this study, was taken on March 15, 2011, covering an area of 5 × 10 km over the Sodankylä test site. The

test site is also the location of the tower-based SnowScat measurements. The data acquisition flights was complemented by near simultaneous in situ measurements, including snow pit measurements (with additional snow pit sites) and distributed measurements of snow depth and SWE. The evolution of snow characteristics throughout the season is reflected by manual snow pit information, as complemented by automated measurements of weather and soil conditions. Coincidental TerraSAR-X data is also available to provide inter-comparison.

The airborne SnowSAR data acquisitions provide spatial variability of the microwave signature of the snow covered ground. Different test sites show quite different snow pack accumulation characteristics, such as snow depth and density, etc. The desired acquisition area over the winter of 2010-2011 consists of 20 parallel and 2 perpendicular flights. The 20 parallel acquisitions are contiguous, from south to north; the other 2 are from east to west. The whole area has covered various landforms of forest, peat bog, and lake ice, etc. Among all the flights, dual-pol data are only available for 4 acquisitions due to an instrumental failure in the Ku-band receiver. The best spatial correlation with the ground in situ sampling points is from the west most flight transects. The more extensive data acquisitions over the winter of 2011-2012 have also provide temporal variability at the main test site and tundra site. However, SAR data of this later season are not yet available at this moment. So the comparisons are confined to the 2010-2011 snow season on March 15th, 2011.

2.7 DMRT-QCA MODEL COMPARISON WITH SNOWSAR DATA

For active remote sensing, the DMRT-QCA model has been used to compare with CLPX radar data [42]. In this section, the DMRT-QCA model results are compared with SnowSAR data.

The physical structure of the snow layers in SnowSAR measurement is modeled as multilayer structure on the top, and a rough ground surface at the bottom. Each snow layer has its own grain size, snow depth, and snow density, which are collected from ground measurements. The upper layers have small grain size, typically around 0.5 mm, while the lower layers have large grain size, typically greater than 1.0 mm or even up to 3.0 mm. The snow grain size variations are due to the snow accumulation fallen at different days. The upper layers are composed of newly fallen dry snow, while lower layers are composed of snow with a few melt-freeze cycles. It is noteworthy that the snow depth data were collected from a few isolated points over the entire map of the SnowSAR flight. Five snow pits that have complete ground data were also measured. However, radar data did not cover the entire map because of an instrumental failure of the mini-SAR system. Therefore in the geographical range of the radar data, complete ground data is available at only one snow pit, and snow depth data are sparsely distributed.

In Table 2-5, the measured snow parameters of snow layer structure at the IOA snow pit on March 15th, 2011 are listed, including the snow depth, visual grain size and mean density of each layer. In the table, the stickiness parameters τ of the QCA scattering model used for each layer are also listed. The airborne SnowSAR backscattering measurements were performed on the same day. The flight track (data acquisition nr. 2(a)) covered the IOA snow pit. Besides the snow pit measurement, distributed snow course sampling was also made. The snow course sampling only provided snow depth and SWE information. The sampling points which had overlap with the flight tract were selected out of the measurements on March 17th, 2011, two days after the SnowSAR flight. The scattering data was extracted out of the 2m resolution SAR image with the nearest pixel.

Table 2-5. Snowpack layer structure measured at IOA snowpit on 03/15/2011, and corresponding QCA stickiness parameters

Index of layer	Snow depth [cm]	Grain size [mm]	Density [g/cc]	Stickiness parameter τ
1	30	0.5	0.111	0.12
2	20	1.0	0.224	0.15
3	7	2.0	0.189	0.25
4	18	3.0	0.216	0.35

At present, available ground data are the complete snow profile of the IOA snowpit and depth information in other points distributed in the entire map area. At the distributed sampling points, only snow depth and SWE information are available. The IOA site is coincidental for SnowSAR and SnowScat datasets. Therefore in the SnowSAR comparison, a four layer model based on the IOA snowpit was assumed. The author used the measured snow structure at IOA snow pit (as shown in Table 2-5) and backscattering coefficients to tune the stickiness parameter τ as well as ground roughness. At distributed sampling points, the grain size, density and stickiness parameters for each layer are taken to be the same as IOA site, which is shown in Table 2-5. The snow depth of each layer and ground roughness are tuning parameters. The optimization parameters were chosen to match backscattering coefficients at both X and Ku bands. A 1^{st} order multi-layer DMRT forward scattering model was applied to the profiles shown in Table 2-6 to

match the SnowSAR data, as shown in Figure 2-17(b). The ground roughness effect was included in this first order model by adding the rough surface backscattering with attenuation. The ratio between the correlation length and rms height was fixed to 4, and ground permittivity was fixed to $(3 + 1i)\varepsilon_{eff}$, where $\varepsilon_{eff} \approx 1.3\varepsilon_0$ is the effective permittivity of the bottom snow layer. The rough surface backscattering was computed using a NMM3D lookup table. As comparison, a simpler single layer DMRT with flat frozen ground and with multiple scattering effects was also applied to these sampling points, as shown in Figure 2-17(a). The measured total snow depth is used in the model, and the grain size is set to 0.7 mm, stickiness parameter τ 0.1, and fractional volume 20%. The stickiness parameter τ is related to clustering effects, and affects the frequency dependence and size dependence. In Monte Carlo simulations of positions of particles [11], the stickiness is represented by an adhesive potential that attracts the spheres. This then gives a probability of adhesion which is implemented numerically during shuffling of spheres positions. In the data comparison, τ is obtained from a minimization procedure to give the size dependence and frequency dependence of scattering coefficient κ_s at IOA snow pit where sufficient ground measurements are available. Since the grain size profile is known, an assumption is made that the Ku band backscattering coefficients mainly comes from the bottom layers with largest grain size. This assumption would give an initial guess for the stickiness parameter of the bottom layers. The stickiness parameter for other layers are then determined by keeping a reasonable size dependence of κ_s. All the parameters are then refined based on a minimization procedure, to achieve better agreement as well as reasonable frequency / size dependence.

Table 2-6 Parameter setup in 1st order multilayer DMRT with rough ground

Total depth (cm)	Top layer 1 (cm)	Layer 2 (cm)	Layer 3 (cm)	Bottom Layer 4 (cm)	Ground rms (mm)	Ground cl/rms	Ground permittivity
45	30	10	5	0	2.63	4	$(3 + 1i)\varepsilon_{eff}$
55	30	18	5	2	3.05	4	$(3 + 1i)\varepsilon_{eff}$
65	30	20	7	8	3.05	4	$(3 + 1i)\varepsilon_{eff}$
75	30	20	7	18	3.05	4	$(3 + 1i)\varepsilon_{eff}$

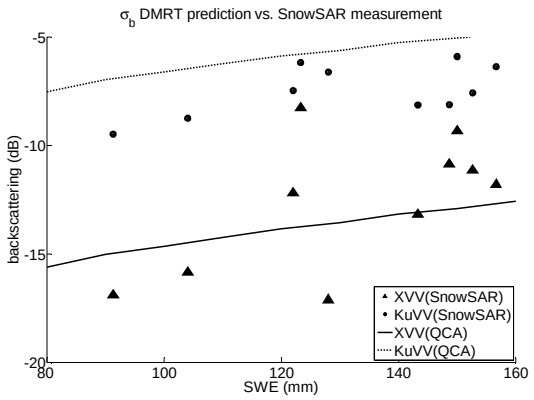

(a)

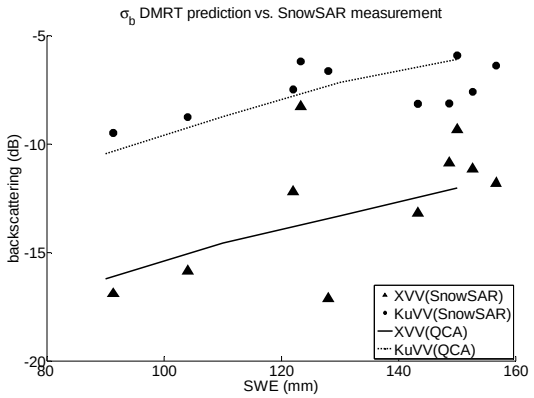

(b)

Figure 2-17 Comparison between SnowSAR measurement and DMRT-QCA prediction

(a) Single layer model with multiple scattering. Grain diameter 0.7mm, stickiness $\tau = 0.1$, fractional volume 20%, $\varepsilon_{r,ice} = 3.15 + i0.001$, flat ground $\varepsilon_{r,gnd} = 3.2 + i0.002$ (b) 1st order Multilayer model with rough ground. Parameter setup is listed in Table 2-5 & 2-6.

Figure 2-17 also indicates the difference between single layer model and multilayer model, over the whole dataset. It is known that he surface scattering has minor contribution to Ku band backscattering coefficients, and from Table 2-6, in the multilayer configuration, only the ground

roughness of the 45cm snow depth is different from others. Therefore comparing Figure 2-17(a) and 17(b), the difference in backscattering is mostly due to multilayer model. A careful analysis of the 1st order multilayer DMRT indicates that the main contribution to the backscattering comes from the dominant layers at the bottom with larger grain sizes. This is contrary to the single layer model, which does not capture the variability in depth dependence. The single layer model does not exhibit the frequency dependence of the measurements neither. Table 2-7 shows the RMS errors and correlation coefficients between DMRT-QCA prediction and SnowSAR data. It is seen that the RMSE for the Ku band is significantly improved by the multilayer DMRT model. The RMSE for X band, and the correlation coefficients at both bands, do not improve as much because of the sparse distribution behavior of the data. In Figure 2-17, DMRT prediction shows that the model sensitivities to SWE at the two frequencies are close to each other. It is noteworthy that SnowSAR has a spatially varying dataset, so the ground permittivity and roughness varies. The X-band backscattering coefficients, which results from a thinner optical thickness, is more sensitive to the ground backscattering.

Table 2-7 RMS errors and correlation coefficients between DMRT-QCA prediction and SnowSAR data

	$\mathrm{RMSE_X}$	$\mathrm{RMSE_{Ku}}$	r_{X}	r_{Ku}
Single layer	2.6656	2.0714	0.6238	0.6036
Multiple layer	2.3851	1.1630	0.6179	0.6233

2.8 DMRT-BICONTINUOUS MODEL COMPARISON WITH SNOWSCAT DATA

The DMRT-bicontinuous model is implemented by incorporating bicontinuous phase matrices into the DMRT equations. Rough surface effect is considered in an additive way, shown by Equation (2-16) in Section 2.5. The RMS height of the rough surface is assumed to be 1 mm, and the correlation length of the rough surface is 4 mm. The ground is assumed to be frozen ground with permittivity $(3.4 + 0.84i)\varepsilon_0$.

Model results are compared with SnowScat scatterometer data, collected by FMI over Finland area, from January to March, 2011. The data include three channels in X-band and Ku-band: 10.2 GHz, 13.3 GHz and 16.7 GHz. Ground data at a specific snowpit (IOA snowpit) include grain size, layer structure, snow depth, snow density, and SSA, etc. In Figure 2-18, comparisons at three channels are shown as a function of snow depth. The backscattering increases slightly as snow depth increases. In Figure 2-18(a), the backscattering predicted by DMRT-bicontinuous model is higher than measured data. The results at 13.3 GHz and 16.7 GHz are in good agreement.

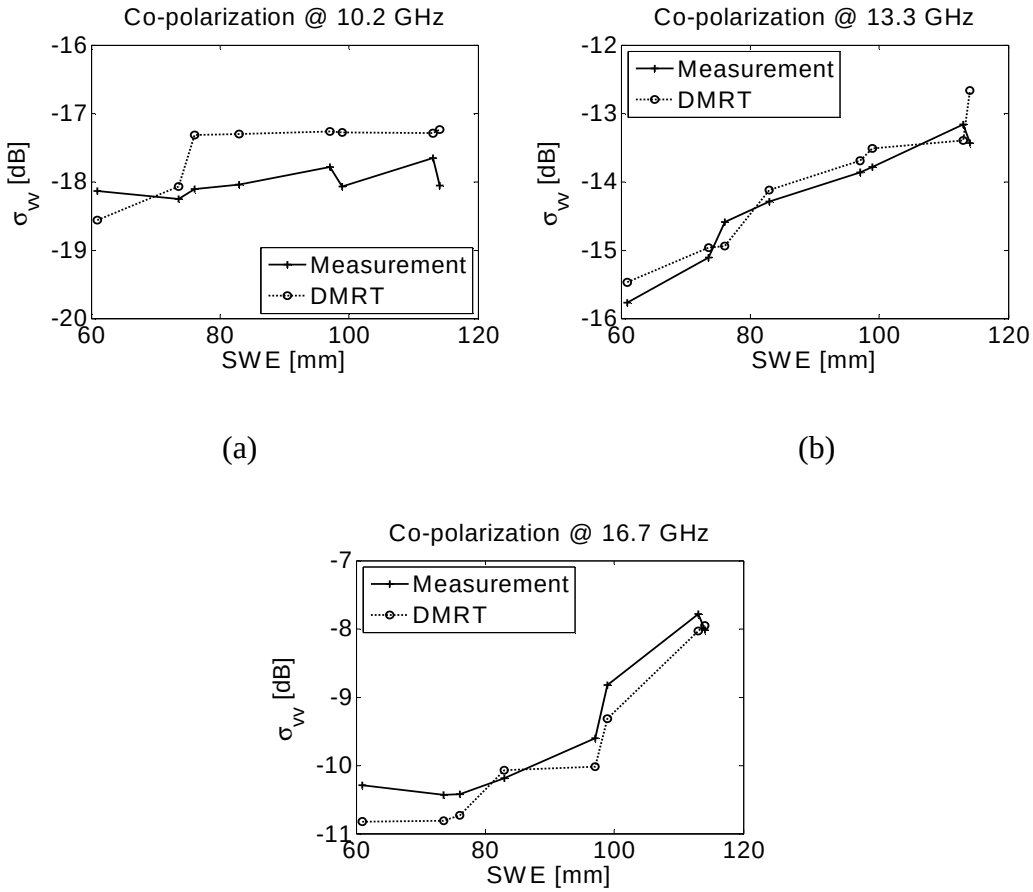

Figure 2-18 DMRT-bicontinuous prediction compared with measured radar backscattering at IOA snowpit

(a) 10.2 GHz (b) 13.3 GHz (c) 16.7 GHz

Table 2-8 lists the physical parameters measured at Jan. 18, 2011, and the numerical parameters extracted from bicontinuous model. The first five columns are the ground data. It is noteworthy that the grain size and the density are measured on the same day as the radar measurement; however SSA data on the same day is not available at this moment. Therefore SSA measured in another two years on the same site are used. The fourth and fifth column of Table 2-8 are the

SSA measured at Jan. 17, 2012 and Jan. 15, 2013. It is seen that within three days and at the same site, SSA are well correlated between two different years, so it is reasonably assumed that the acquired SSA are representative of the SSA at Jan. 18, 2011, when the radar data is available. More datasets on SSA show that typical values of measured SSA at the bottom layers are 59 ~ 124 cm^2 / g, and are 100 ~ 790 cm^2 / g at top and intermediate layers. In Table 2-8, the bicontinuous SSA (the eighth column) agrees with the ground data, except for the second layer from the top. The exception is due to the large grain size observed in the experiment. Ground data shows that mean grain size in the second layer is 2 mm, which is rarely seen at top layers. Such large grain size will lead to small bicontinuous parameter $\langle\zeta\rangle$ and small analytical SSA, but measured SSA is in the normal range 241 ~ 373 cm^2/g which is attributed to small ice grains. The relationship between SSA and radar backscattering coefficients on the same day will be a subject of continual study.

Table 2-8. Measured parameters and extracted parameters comparison.

Time series data # 3, collected at Jan. 18, 2011.

SSA data collected at Jan. 17, 2012 and Jan. 15, 2013.

Index of layer	Grain size [mm]	Density [g/cc]	Measured SSA [cm^2 / g]		$\langle\zeta\rangle$ [m^{-1}]	*b*	Bicontinuous SSA [cm^2 / g]	Bicontinuous correlation length [mm]
			2012	2013				
1	0.3	0.064	289	230	50000	1.0	395	0.029
2	2.5	0.064	373	241	6000	1.0	47.3	0.23
3	0.5	0.156	300	234	30000	1.0	347	0.054
4	0.5	0.164	218	223	30000	1.0	352	0.054
5	1.3	0.168	180	160	11500	1.0	136	0.14
6	2.0	0.208	142	95	7500	1.7	88.2	0.23
7	2.5	0.180	135	104	7000	2.0	79.2	0.24
8	2.0	0.180	110	102	7500	1.7	86.0	0.22
9	2.8	0.208	145	102	5500	2.0	63.8	0.31

The correlation length was not measured in SnowScat ground data, but Table 2-8 shows the correlation length extracted from bicontinuous model increases with the grain size. This establishes the connection between model parameters and ground data.

The total backscattering coefficients is composed of volume scattering from snow, and surface scattering from snow-ground interface. Table 2-9 shows the contribution of volume scattering and rough surface scattering to the total radar backscattering coefficients. As shown in Table 2-9, surface scattering plays an important role at X-band. When surface scattering is significant in the total backscattering coefficients, the increasing trend of volume scattering is not apparent. In the simulations the author assumed that the snow-ground interface roughness condition did not change throughout the studied period so that the backscattering coefficient from the surface (σ_{SURF}) is a constant. It is seen that at X-band, rough surface scattering is comparable to volume scattering, while at 13.3 GHz of Ku-band, rough surface scattering is at least 4 dB lower than volume scattering, at 16.7 GHz of Ku-band, rough surface scattering is at least 6 dB lower than volume scattering. Therefore it is important to use an accurate snow model at high frequencies of Ku-band.

Table 2-9. Contribution of volume scattering and rough surface scattering.

Time series data # 3, collected at Jan. 18, 2011.

Frequency [GHz]	Volume scattering $\sigma_{VOL}\ [dB]$	Rough surface scattering (Attenuated by optical depth) $\sigma_{SURF}\exp(-2\kappa_e d\sec\theta_i)\ [dB]$	Total backscattering coefficients $\sigma_0\ [dB]$
10.2	-20.37	-20.29	-17.32
13.4	-16.37	-20.45	-14.94
16.7	-11.67	-17.86	-10.74

By applying the phase matrices of bicontinuous models to DMRT equations, the resulting backscattering coefficients show good agreement with SnowScat data, using the collected ground truth as input parameters. In actual practice of airborne and spaceborne missions, some parameters are not measured and judicious guessed values are used in the simulation. Changes in the value of these parameters affect simulation results. For example, in the DMRT-bicontinuous model, ground scattering is a guessed contribution. One possible solution is to collect the ground parameters before the snow season, in order to obtain a reasonable estimation for the simulation parameters. Another solution is to use cost function minimization in developing retrieval algorithms for airborne campaigns and space missions, without any prior knowledge of the ground status before the snow season. In such a case, regularized techniques in the minimization of cost functions will be used. This includes adapting the parameters of the DMRT models to

airborne measurements in various intensive campaign sites, as well as developing regularization parameters.

By combining DMRT equations with bicontinuous model, both backscattering coefficients σ_0 and brightness temperature T_B can be computed. In aircraft campaigns and satellite missions, combined active and passive microwave remote sensing are deployed increasingly. When the bicontinuous model is applied to passive microwave remote sensing, the moderate forward scattering effect that was shown in Section 2.4 is of particular importance, and is associated with parameter b [40]. Brightness temperatures with the same scattering coefficient, but different mean cosine of scattering will have significant difference in brightness temperatures particularly at 37 GHz. It is seen that when $\bar{\mu}$ is larger, more forward scattering exists in snow. Thus more emission will be received by the radiometer. As a consequence, the brightness temperature will be larger. The combined passive and active results are reported in [40] and is a subject of continual study.

2.9 CONCLUSION

In this chapter, the DMRT-QCA model and DMRT-bicontinuous model are applied to predict the radar backscattering coefficients of terrestrial snow, and are compared with multi-frequency experiments of SnowSAR and SnowScat respectively.

Both DMRT models account for the dense effects of closely packed ice grains, when the near-field and intermediate-field coherent wave interactions among the ice grains are strong. QCA model is an analytic approximation, while bicontinuous model is based on exact solutions of Maxwell equations, to compute the phase matrices of automatically generated microstructures of snow. The models give weaker frequency and size dependences than classical Rayleigh

scattering. They also give stronger forward scattering in the phase matrix, than the Rayleigh phase functions. In comparisons with multi-frequency experiments, the author used the same model parameters for all frequencies. The aggregation effects of ice grains are clearly seen by using the stickiness parameters in QCA model, and the size distribution parameter b in the bicontinuous model. The author also developed relations between the model parameters to the physically measured ground truth. These relations include grain sizes, as well as SSA and autocorrelation functions. Development of such relations will continue to be studied. In particular, the microstructures of bicontinuous model resemble that of real snow. Quantitative comparisons of the microstructure of real snow and automatically generated snow will be performed. By applying the phase matrices of QCA and bicontinuous models to DMRT equations, the resulting backscattering coefficients show good agreement with SnowSAR and SnowScat data respectively, using the collected ground truth as input parameters.

CHAPTER 3: BACKSCATTERING ENHANCEMENT AND MULTIPLE-SCATTERING EFFECTS

3.1 INTRODUCTION

It is important to develop microwave emission and scattering models of snowpack to explain the observed microwave signatures and to facilitate SWE retrieval. In the past, most of the modeling work was done for passive microwave remote sensing because of the prevalence of brightness temperature data. The empirical model developed in Helsinki University of Technology (HUT) [28] [29] based on extinction rate measurement of snow slab [43], the semi-empirical thermal microwave emission model of layered snowpacks (MEMLS) [24] [25] based on brightness temperature measurement of snow [23] [26], and dense media radiative transfer multi-layer model (DMRT-ML) [44] based on the physical scattering model of QCA-CP [11] [12] [18] are all designed for passive remote sensing. With the recent prospects of acquiring radar observations at sufficiently high frequencies to detect properties of the snow volume, the semi-empirical radiative transfer (sRT) model [6] [45] [46] based on first order RT theory was developed. Furthermore, the active DMRT theory has been applied to include multiple scattering effects [15]. In the framework of the dense media radiative transfer (DMRT) theory, the quasi-crystalline approximation (QCA) with stickiness [11] [12] was developed to model scattering from cluster of dielectric spheres adhered to form aggregates. The extinction rate and co-pol scattering phase matrix was validated by Monte Carlo simulation of sticky spheres and solving Foldy-Lax multiple scattering equations [16] [47]. The QCA phase matrix was then combined with DMRT to predict both brightness temperature [14] [48] and backscattering coefficient [15]. Bicontinuous media and discrete dipole approximation (DDA) scattering model [13] was then developed to account for the irregular shape of ice grains, providing good estimations of cross-

pol backscattering coefficients. The bicontinuous media phase matrix was also combined with DMRT to predict brightness temperature and backscattering coefficients [33] [49]. The multiple scattering effects are accounted for by solving the vector radiative transfer equation using a discrete coordinate approach based on the quadrature eigenvalue analysis [15].

In all of these approaches, when both brightness temperature and backscattering are of interest, either completely different models are used for passive and active, respectively, or even if the same model is used, one needs to feed the model with different parameters in order to get agreement with field measurements. Typically, if one fixes the input parameter for both active and passive microwave models, and tunes parameters to match the measured backscattering coefficients, then the model prediction of brightness temperature will be too low. This is because of the ignorance of the backscattering enhancement effects in the radiative transfer equations. Radiative transfer theory only includes the ladder terms of the Feynman diagrams. Backscattering enhancement is due to the cyclical terms of the Feynman diagrams [12] [18] [50] [51]. In the backscattering direction, the forward path and reverse path have exactly the same phase shift and give constructive interference of the two scattered fields. However, as the scattering direction deviates from the backscattering direction, the coherent addition of fields quickly degrades to the incoherent addition of energy. The phase of two scattered fields fluctuates due to the random position of scatterers, leading to a peak of finite angular width spread near the backscattering direction. Backscattering enhancement is of less importance in passive remote sensing because the angular width of enhancement is small and does not contribute much to energy transport of radiation. In backscattering, this effect has been observed in laboratory experiments of optical scattering of densely packed latex microspheres suspended in deionized water for both co-polarization and cross-polarization [52] [53]. The depolarization

effects of the enhanced retro-reflectance in volume scattering due to multiple scattering effects differs itself from surface scattering exhibiting no cross-pol enhancement [53]. This has been explained by analytically summing up all the ladder and cyclical terms in purely volume scattering using the wave approach [50] [51]. Only backscattering enhancement in volume scattering was considered in [50] [51] because the optical thickness of the colloidal sol was so large that the boundary effects were essentially negligible. The enhancement also occurs when there are interactions with boundaries. The effect can also be exhibited with the distorted Born approximation [54]. However, the distorted Born approximation only accounts for single volume scattering. Single scattering quickly saturates with the increase of optical thickness. In [15] multiple scattering was included in the frame work of radiative transfer but backscattering enhancement was not accounted for.

The solution of radiative transfer equations agrees with the wave approach if cyclical correction is included. The cyclical correction for co-polarization is easily done by a factor of two for the contribution of the cyclical terms [18]. The cyclical terms could be easily tracked by solving the vector radiative transfer equation using an iterative approach. With the iterative approach, the higher order scattering is updated from lower order scattering. Thus the contribution from different scattering orders is separated and this offers a natural evaluation of multiple scattering effects. Each scattering order is comprised of many physically interpretable terms; each term is corresponding to a unique scattering path, depending on the sequence of volume scattering and surface bounces, and contributes to certain kind of scattering mechanism [18] [32]. Those terms, if the sequence of scattering and surface bounces is reversed, that is corresponding to another physically distinct term, are identified as cyclical terms. Manual manipulation of all these terms is not feasible for higher scattering orders. Thus a numerical iterative approach is adopted to

automatically keep track of all these scattering paths. In the numerical iterative approach, the specific intensity is discretized with respect to its three independent coordinates θ, ϕ and z. For most random medium with azimuth symmetry, the phase matrix is only required at one fixed azimuth incidence angle ϕ_i. The iteration is carried out numerically to higher order until the convergence of backscattering coefficients. The cyclical terms are identified and their contribution is doubled when being included in the total radar backscattering.

The vector radiative transfer equation will be solved with two reflective boundaries both at bottom and on the top, as in the case of terrestrial snowpack scattering. This is an extension of the research where only one bottom reflective boundary is considered as in the case of vegetated surface layer scattering. The phase matrix and extinction matrix of these two cases are of course different. Both QCA with sticky spheres and bicontinuous / DDA scattering model are applied to account for the dense medium scattering effects. The QCA model is applied to compare results with the previous work [15]. The bistatic scattering result of the numerical iterative approach agrees with the quadrature eigenvalue analysis approach if cyclical correction is ignored. However, the backscattering with cyclical correction is significantly increased. The backscattering enhancement effects are evaluated both at X- and Ku- band for co-polarization. The bicontinuous / DDA phase matrix is then applied to the ground data acquired in the NoSREx campaign in the snow season of 2011 to 2012 by the Finish Meteorological Institute (FMI) under an ESA contract in Sodankylä northern Finland [8] [55]. Radar backscattering coefficients is predicted using this numerical iterative approach with cyclical correction. Brightness temperature is predicted by a separate DMRT code with multiple scattering effects included [48]. The same set of snowpack parameters is applied. Results show good agreement with multiple

channel observations of both scatterometer (X- to Ku- band) and radiometer (X- to Ka- band) data.

This Chapter is organized as follows. In Section 3.2, the numerical iterative approach with cyclical correction is formulated. In Section 3.3, QCA phase matrix is applied to compare bistatic scattering results with [15] and to illustrate the backscattering enhancement effects. In Section 3.4, bicontinuous media phase matrix is applied to valid the model against active and passive multiple frequency observations from the NoSREx campaign. Finally, conclusions are drawn in Section 3.5.

3.2 NUMERICAL ITERATIVE APPROACH WITH CYCLICAL CORRECTION

3.2.1 DMRT and iterative approach

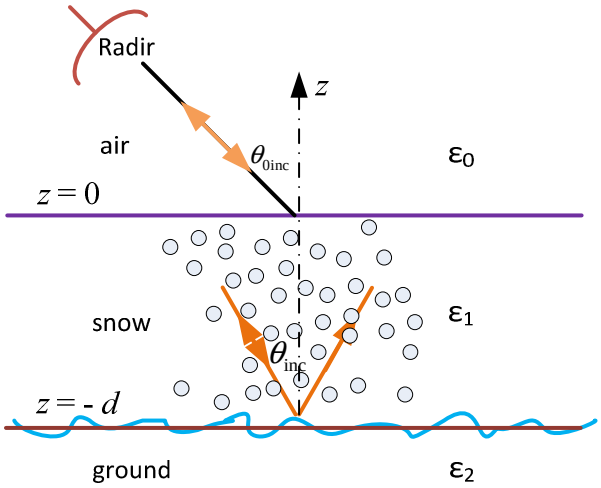

Figure 3-1 Active remote sensing of a snow layer

First consider the active remote sensing of a snow layer with thickness d above ground, as shown in Figure 3-1. Region 0 is air, region 1 is snow and region 2 is ground. The ground

surface could be either flat or rough. The vector dense media radiative transfer (DMRT) equations governing the specific intensity $\bar{I}(\theta,\phi,z)$ [15] [18] [32] are

$$\cos\theta\frac{d\bar{I}(\theta,\phi,z)}{dz}=-\kappa_e\cdot\bar{I}(\theta,\phi,z)+\bar{S}(\theta,\phi,z) \tag{3-1a}$$

$$-\cos\theta\frac{d\bar{I}(\theta,\phi,z)}{dz}=-\kappa_e\cdot\bar{I}(\pi-\theta,\phi,z)+\bar{W}(\theta,\phi,z) \tag{3-1b}$$

κ_e is the extinction coefficient. The source terms $\bar{S}(\theta,\phi,z)$ and $\bar{W}(\theta,\phi,z)$ are related to the specific intensity by phase matrix $\bar{\bar{P}}$,

$$\begin{aligned}\bar{S}(\theta,\phi,z)=\int_0^{2\pi}d\phi'\int_0^{\pi/2}d\theta'\,sin\,\theta'\big[&\bar{\bar{P}}(\theta,\phi;\theta',\phi')\cdot\bar{I}(\theta',\phi',z)\\&+\bar{\bar{P}}(\theta,\phi;\pi-\theta',\phi')\cdot\bar{I}(\pi-\theta',\phi',z)\big]\end{aligned} \tag{3-2a}$$

$$\begin{aligned}\bar{W}(\theta,\phi,z)=\int_0^{2\pi}d\phi'\int_0^{\pi/2}d\theta'\,sin\,\theta'\big[&\bar{\bar{P}}(\pi-\theta,\phi;\theta',\phi')\cdot\bar{I}(\theta',\phi',z)\\&+\bar{\bar{P}}(\pi-\theta,\phi;\pi-\theta',\phi')\cdot\bar{I}(\pi-\theta',\phi',z)\big]\end{aligned} \tag{3-2b}$$

The top reflective boundary condition at $z=0$,

$$\begin{aligned}&\bar{I}(\pi-\theta,\phi,z=0)\\&\quad=\bar{\bar{R}}_{10}(\theta)\bar{I}(\theta,\phi,z=0)\\&\quad+\bar{\bar{T}}_{01}(\theta_0)\bar{I}_0\delta(\cos\theta_0-\cos\theta_{0\mathrm{inc}})\delta(\phi-\phi_{\mathrm{inc}})\end{aligned} \tag{3-3a}$$

and the bottom reflective boundary condition at $z=-d$,

$$\bar{I}(\theta,\phi,z=-d)=\bar{\bar{R}}_{12}(\theta)\bar{I}(\pi-\theta,\phi,z=-d) \tag{3-3b}$$

The angle in air region θ_0 is related to the angle in snow region θ by Snell's law, $n_0 \sin\theta_0 = n_1 \sin\theta$. $n_1 = \sqrt{\varepsilon_1/\varepsilon_0}$. ε_1 is the real part of the effective dielectric constant of snow. The incidence angle in air region $\theta_{0\text{inc}}$ is also related to angle θ_{inc} in snow region by Snell's law. $\bar{\bar{R}}_{10}(\theta)$ and $\bar{\bar{R}}_{12}(\theta)$ are the reflective matrix on the snow-air boundary and the snow-ground boundary. $\bar{\bar{T}}_{01}(\theta_0)$ is the transmissivity matrix from air to snow [18] [32].

When the bottom boundary is rough with rms height h, the coherent reflectivity $\bar{\bar{R}}_{12}(\theta)$ is multiplied by an attenuation factor K_F^2 following Kirchhoff approximation, where $K_F = \exp(-2(n_1 k \cos\theta\, h)^2)$. k is the wavenumber in free space.

The DMRT equation could be casted into two coupled integral equations using method of variation of variables,

$$
\begin{aligned}
&\bar{I}(\theta,\phi,z) \\
&= \exp(-\kappa_e(z+2d)\sec\theta)\,\bar{\bar{R}}_{12}(\theta)\bar{\bar{Z}}^{-1}(\theta)\bar{\bar{T}}_{01}(\theta_0)\bar{I}_0\delta(\cos\theta_0-\cos\theta_{0\text{inc}})\delta(\phi \\
&-\phi_{\text{inc}}) \\
&+\sec\theta\exp(-\kappa_e(z \\
&+2d)\sec\theta)\,\bar{\bar{R}}_{12}(\theta)\bar{\bar{Z}}^{-1}(\theta)\bar{\bar{R}}_{10}(\theta)\int_{-d}^{0}dz'\exp(\kappa_e z'\sec\theta)\,\bar{S}(\theta,\phi,z') \\
&+\sec\theta\exp(-\kappa_e(z+d)\sec\theta)\,\bar{\bar{R}}_{12}(\theta)\bar{\bar{Z}}^{-1}(\theta)\int_{-d}^{0}dz'\exp(-\kappa_e(z' \\
&+d)\sec\theta)\,\bar{W}(\theta,\phi,z')+\sec\theta\int_{-d}^{z}dz'\exp(\kappa_e(z'-z)\sec\theta)\,\bar{S}(\theta,\phi,z')
\end{aligned}
\tag{3-4a}
$$

$$
\begin{aligned}
&\bar{I}(\pi-\theta,\phi,z)\\
&=\exp(\kappa_e z\sec\theta)\,\bar{\bar{Z}}^{-1}(\theta)\bar{\bar{T}}_{01}(\theta_0)\bar{I}_0\delta(\cos\theta_0-\cos\theta_{0\mathrm{inc}})\delta(\phi-\phi_{\mathrm{inc}})\\
&+\sec\theta\exp(\kappa_e z\sec\theta)\,\bar{\bar{Z}}^{-1}(\theta)\bar{\bar{R}}_{10}(\theta)\int_{-d}^{0}dz'\exp(\kappa_e z'\sec\theta)\,\bar{S}(\theta,\phi,z')\\
&+\sec\theta\exp(\kappa_e(z-d)\sec\theta)\,\bar{\bar{Z}}^{-1}(\theta)\bar{\bar{R}}_{10}(\theta)\bar{\bar{R}}_{12}(\theta)\int_{-d}^{0}dz'\exp(-\kappa_e(z'\\
&+d)\sec\theta)\,\bar{W}(\theta,\phi,z')+\sec\theta\int_{z}^{0}dz'\exp(\kappa_e(z'-z)\sec\theta)\,\bar{W}(\theta,\phi,z')
\end{aligned}
\tag{3-4b}
$$

where $\bar{\bar{Z}}(\theta)=\bar{\bar{I}}-\bar{\bar{R}}_{10}(\theta)\bar{\bar{R}}_{12}(\theta)\exp(-\kappa_e 2d\sec\theta)$.

Equation (4a, 4b) could be solved using iterative approach, $\bar{I}=\bar{I}^{(0)}+\bar{I}^{(1)}+\cdots$, by viewing $\bar{S}$ and $\bar{W}$ as small perturbations. The zero-th order solution $\bar{I}^{(0)}$, known as the reduced solution, is the first term in equation (4a, 4b) and does not contribute to backscattering. The n-th order solution $\bar{I}^{(n)}$ $(n=1,2,\ldots)$ could be updated from lower order solution $\bar{I}^{(n-1)}$ through source terms $\bar{S}^{(n)}$ and $\bar{W}^{(n)}$.

$$
\begin{aligned}
\bar{I}^{(n)}(\theta,\phi,z)=&\exp(-\kappa_e(z+2d)\sec\theta)\,\bar{\bar{R}}_{12}(\theta)\bar{\bar{Z}}^{-1}(\theta)\bar{\bar{R}}_{10}(\theta)\bar{S}_c^{(n)}(\theta,\phi)\\
&+\exp(-\kappa_e(z+d)\sec\theta)\,\bar{\bar{R}}_{12}(\theta)\bar{\bar{Z}}^{-1}(\theta)\bar{W}_c^{(n)}(\theta,\phi)\\
&+\bar{S}_z^{(n)}(\theta,\phi,z')
\end{aligned}
\tag{3-5a}
$$

$$
\begin{aligned}
&\bar{I}^{(n)}(\pi-\theta,\phi,z)\\
&\quad=\exp(\kappa_e z\sec\theta)\,\bar{\bar{Z}}^{-1}(\theta)\bar{\bar{R}}_{10}(\theta)\bar{S}_c^{(n)}(\theta,\phi)\\
&\quad+\exp(\kappa_e(z-d)\sec\theta)\,\bar{\bar{Z}}^{-1}(\theta)\bar{\bar{R}}_{10}(\theta)\bar{\bar{R}}_{12}(\theta)\bar{W}_c^{(n)}(\theta,\phi)\\
&\quad+\bar{W}_z^{(n)}(\theta,\phi,z')
\end{aligned}
\tag{3-5b}
$$

where $\bar{S}_c^{(n)}(\theta,\phi) = \sec\theta \int_{-d}^{0} dz' \exp(\kappa_e z' \sec\theta)\, \bar{S}^{(n)}(\theta,\phi,z')$,

$\bar{W}_c^{(n)}(\theta,\phi) = \sec\theta \int_{-d}^{0} dz' \exp(-\kappa_e (z'+d) \sec\theta)\, \bar{W}^{(n)}(\theta,\phi,z')$ and $\bar{S}_z^{(n)}(\theta,\phi,z) = \sec\theta \int_{-d}^{z} dz' \exp(\kappa_e (z'-z) \sec\theta)\, \bar{S}^{(n)}(\theta,\phi,z')$, $\bar{W}_z^{(n)}(\theta,\phi,z) = \sec\theta \int_{z}^{0} dz' \exp(\kappa_e (z'-z) \sec\theta)\, \bar{W}^{(n)}(\theta,\phi,z')$ are defined for short.

$\bar{S}^{(n)}$ and $\bar{W}^{(n)}$ are related to $\bar{I}^{(n-1)}$ by equation (2a, 2b), with $\bar{S}^{(1)}$ and $\bar{W}^{(1)}$ given explicitly,

$$\begin{aligned}\bar{S}^{(1)}(\theta,\phi,z) = {} & \bar{\bar{P}}(\theta,\phi;\theta_{\text{inc}},\phi_{\text{inc}})\bar{M}^{(0)}(\theta_{\text{inc}}) \exp(-\kappa_e (z+2d)\sec\theta_{\text{inc}}) \\ & + \bar{\bar{P}}(\theta,\phi;\pi-\theta_{\text{inc}},\phi_{\text{inc}})\bar{N}^{(0)}(\theta_{\text{inc}}) \exp(\kappa_e z \sec\theta_{\text{inc}})\end{aligned} \tag{3-6a}$$

$$\begin{aligned}\bar{W}^{(1)}(\theta,\phi,z) = {} & \bar{\bar{P}}(\pi-\theta,\phi;\theta_{\text{inc}},\phi_{\text{inc}})\bar{M}^{(0)}(\theta_{\text{inc}}) \exp(-\kappa_e (z+2d)\sec\theta_{\text{inc}}) \\ & + \bar{\bar{P}}(\pi-\theta,\phi;\pi-\theta_{\text{inc}},\phi_{\text{inc}})\bar{N}^{(0)}(\theta_{\text{inc}}) \exp(\kappa_e z \sec\theta_{\text{inc}})\end{aligned} \tag{3-6b}$$

where $\bar{M}^{(0)}(\theta_{\text{inc}}) = \bar{\bar{R}}_{12}(\theta_{\text{inc}})\bar{\bar{Z}}^{-1}(\theta_{\text{inc}})\bar{\bar{T}}_{01}(\theta_{0\text{inc}})\bar{I}_0 \frac{\varepsilon_0 \cos\theta_{0\text{inc}}}{\varepsilon_1 \cos\theta_{\text{inc}}}$, and $\bar{N}^{(0)}(\theta_{\text{inc}}) = \bar{\bar{Z}}^{-1}(\theta_{\text{inc}})\bar{\bar{T}}_{01}(\theta_{0\text{inc}})\bar{I}_0 \frac{\varepsilon_0 \cos\theta_{0\text{inc}}}{\varepsilon_1 \cos\theta_{\text{inc}}}$.

The contribution to bistatic scattering coefficient $\gamma_{\beta\alpha}^{(n)}(\theta_0,\phi;\theta_{0\text{inc}},\phi_{\text{inc}})$ and backscattering coefficient $\sigma_{\beta\alpha}^{(n)}(\theta_{0\text{inc}},\phi_{\text{inc}})$ from the n-th order specific intensity $\bar{I}^{(n)}(\theta,\phi,z)$ is [15] [18] [32]

$$\gamma_{\beta\alpha}^{(n)}(\theta_0,\phi;\theta_{0\text{inc}},\phi_{\text{inc}}) = 4\pi \frac{\cos\theta_0\, I_{0\beta}^{(n)}(\theta_0,\phi)}{\cos\theta_{0\text{inc}}\, I_{0\text{inc}\alpha}} \tag{3-7}$$

$$\sigma_{\beta\alpha}^{(n)}(\theta_{0\text{inc}},\phi_{\text{inc}}) = \cos\theta_{0\text{inc}}\, \gamma_{\beta\alpha}^{(n)}(\theta_{0\text{inc}},\pi+\phi_{\text{inc}};\theta_{0\text{inc}},\phi_{\text{inc}}) \tag{3-8}$$

where the n-th order specific intensity in the air region $\bar{I}_0^{(n)}(\theta,\phi)$ is related to $\bar{I}^{(n)}(\theta,\phi,z)$ by transmissivity matrix from snow to air $\bar{\bar{T}}_{10}(\theta)$, $\bar{I}_0^{(n)}(\theta,\phi) = \bar{\bar{T}}_{10}(\theta)\cdot\bar{I}^{(n)}(\theta,\phi,z=0)$. The overall bistatic scattering and backscattering is the sum of contribution from each order.

When the underlying boundary is rough, surface scattering also contributes to backscattering by $\sigma_s = \sigma_{s0}(\theta_{\rm inc}) \exp(-2\kappa_e d \sec\theta_{\rm inc})$, where $\sigma_{s0}(\theta_{\rm inc})$ is the bare surface backscattering coefficient at the incidence angle inside the snow medium. The bistatic scattering effects of rough surface is ignored.

3.2.2 Cyclical correction and backscattering enhancement

The advantage of iterative approach is that each term in the expression is corresponding to a physical interpretable scattering path. A scattering path describes the intensity flow in terms of scattering and reflection. The direction of energy flow is automatically separated into upwelling and downwelling, as implied by equation (2a, 2b) or its explicit form of 1st order in equation (6a, 6b). $\bar{S}^{(n)}(\theta,\phi,z)$ and $\bar{W}^{(n)}(\theta,\phi,z)$ are separated into upward and downward component depending on the direction of the lower order specific intensity flow being collected,

$$\bar{S}_u^{(n)}(\theta,\phi,z) = \int_0^{2\pi} d\phi' \int_0^{\pi/2} d\theta' \, sin\,\theta' \, \bar{\bar{P}}(\theta,\phi;\theta',\phi') \cdot \bar{I}^{(n-1)}(\theta',\phi',z) \tag{3-9a}$$

$$\bar{S}_d^{(n)}(\theta,\phi,z) = \int_0^{2\pi} d\phi' \int_0^{\pi/2} d\theta' \, sin\,\theta' \, \bar{\bar{P}}(\theta,\phi;\pi-\theta',\phi') \cdot \bar{I}^{(n-1)}(\pi-\theta',\phi',z) \tag{3-9b}$$

$$\bar{W}_u^{(n)}(\theta,\phi,z) = \int_0^{2\pi} d\phi' \int_0^{\pi/2} d\theta' \, sin\,\theta' \, \bar{\bar{P}}(\pi-\theta,\phi;\theta',\phi') \cdot \bar{I}^{(n-1)}(\theta',\phi',z) \tag{3-9c}$$

$$\bar{W}_d^{(n)}(\theta,\phi,z) = \int_0^{2\pi} d\phi' \int_0^{\pi/2} d\theta' \, sin\,\theta' \, \bar{\bar{P}}(\pi-\theta,\phi;\pi-\theta',\phi') \cdot \bar{I}^{(n-1)}(\pi-\theta',\phi',z) \tag{3-9d}$$

Note $\bar{S}_u^{(n)}$, $\bar{S}_d^{(n)}$, $\bar{W}_u^{(n)}$ and $\bar{W}_d^{(n)}$ denotes all four possibilities of transition in energy flow direction due to scattering by particle once. Then equation (5a, 5b) is automatically ground into four parts,

$$\bar{I}_{Su}^{(n)}(\theta,\phi,z) = \exp(-\kappa_e(z+2d)\sec\theta)\,\bar{\bar{R}}_{12}(\theta)\bar{\bar{Z}}^{-1}(\theta)\bar{\bar{R}}_{10}(\theta)\bar{S}_{cu}^{(n)}(\theta,\phi) + \bar{S}_{zu}^{(n)}(\theta,\phi,z') \tag{3-10a}$$

$$\bar{I}_{Sd}^{(n)}(\theta,\phi,z) = \exp(-\kappa_e(z+2d)\sec\theta)\,\bar{\bar{R}}_{12}(\theta)\bar{\bar{Z}}^{-1}(\theta)\bar{\bar{R}}_{10}(\theta)\bar{S}_{cd}^{(n)}(\theta,\phi) + \bar{S}_{zd}^{(n)}(\theta,\phi,z') \tag{3-10b}$$

$$\bar{I}_{Wu}^{(n)}(\theta,\phi,z) = \exp(-\kappa_e(z+d)\sec\theta)\,\bar{\bar{R}}_{12}(\theta)\bar{\bar{Z}}^{-1}(\theta)\bar{W}_{cu}^{(n)}(\theta,\phi) \tag{3-10c}$$

$$\bar{I}_{Wd}^{(n)}(\theta,\phi,z) = \exp(-\kappa_e(z+d)\sec\theta)\,\bar{\bar{R}}_{12}(\theta)\bar{\bar{Z}}^{-1}(\theta)\bar{W}_{cd}^{(n)}(\theta,\phi) \tag{3-10d}$$

$$\bar{I}_{Su}^{(n)}(\pi-\theta,\phi,z) = \exp(\kappa_e z\sec\theta)\,\bar{\bar{Z}}^{-1}(\theta)\bar{\bar{R}}_{10}(\theta)\bar{S}_{cu}^{(n)}(\theta,\phi) \tag{3-10e}$$

$$\bar{I}_{Sd}^{(n)}(\pi-\theta,\phi,z) = \exp(\kappa_e z\sec\theta)\,\bar{\bar{Z}}^{-1}(\theta)\bar{\bar{R}}_{10}(\theta)\bar{S}_{cd}^{(n)}(\theta,\phi) \tag{3-10f}$$

$$\bar{I}_{Wu}^{(n)}(\pi-\theta,\phi,z) = \exp(\kappa_e(z-d)\sec\theta)\,\bar{\bar{Z}}^{-1}(\theta)\bar{\bar{R}}_{10}(\theta)\bar{\bar{R}}_{12}(\theta)\bar{W}_{cu}^{(n)}(\theta,\phi) + \bar{W}_{zu}^{(n)}(\theta,\phi,z') \tag{3-10g}$$

$$\bar{I}_{Wd}^{(n)}(\pi-\theta,\phi,z) = \exp(\kappa_e(z-d)\sec\theta)\,\bar{\bar{Z}}^{-1}(\theta)\bar{\bar{R}}_{10}(\theta)\bar{\bar{R}}_{12}(\theta)\bar{W}_{cd}^{(n)}(\theta,\phi) + \bar{W}_{zd}^{(n)}(\theta,\phi,z') \tag{3-10h}$$

where $\bar{S}_{cu}^{(n)}$, $\bar{S}_{cd}^{(n)}$, $\bar{S}_{zu}^{(n)}$, $\bar{S}_{zd}^{(n)}$, $\bar{W}_{cu}^{(n)}$, $\bar{W}_{cd}^{(n)}$, $\bar{W}_{zu}^{(n)}$, and $\bar{W}_{zd}^{(n)}$ are defined similar to $\bar{S}_{c}^{(n)}$, $\bar{S}_{z}^{(n)}$, $\bar{W}_{c}^{(n)}$, and $\bar{W}_{z}^{(n)}$ by introducing a new subscript u/d in $\bar{S}^{(n)}$ and $\bar{W}^{(n)}$. It immediately follows that each term in $\bar{I}^{(n-1)}(\theta,\phi,z)$ contributes to two terms in $\bar{I}^{(n)}(\theta,\phi,z)$ and two terms in $\bar{I}^{(n)}(\pi-\theta,\phi,z)$, and each term in $\bar{I}^{(n-1)}(\pi-\theta,\phi,z)$ contributes to another two terms in $\bar{I}^{(n)}(\theta,\phi,z)$ and two terms in $\bar{I}^{(n)}(\pi-\theta,\phi,z)$. A simple deduction results in a total of 4^n separated terms in $\bar{I}^{(n)}(\theta,\phi,z)$ as a result of two reflective boundaries, which greatly increases the number of scattering paths. All these terms could be separated through the bridging connection of $\bar{S}_{u}^{(n)}$, $\bar{S}_{d}^{(n)}$, $\bar{W}_{u}^{(n)}$ and $\bar{W}_{d}^{(n)}$.

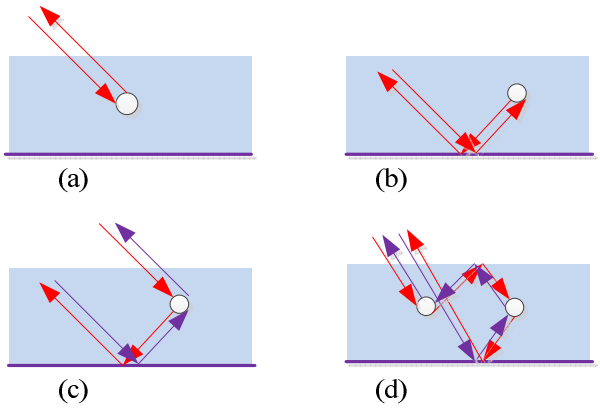

Figure 3-2 illustration of scattering terms

(a) non-cyclical term in 1st order backward volume scattering

(b) non-cyclical term in 1st order volume scattering with twice bounce from surface

(c) dual cyclical terms in 1st order volume-surface double bounce scattering

(d) dual cyclical terms in 2nd order volume scattering with twice bounce from surfaces

In Figure 3-2, several scattering terms are illustrated for example. Each term is depicted by a scattering path in backscattering direction. In general, for each of these paths, if the energy flow direction is reversed, it is corresponding to another distinct scattering and reflection process. In backscattering direction, if this also holds, it is a cyclical term, as shown in Figure 3-2 (c, d). A cyclical term is special that in backscattering direction, the two scattering fields of the two reverse scattering processes are identical for co-pol, both in magnitude and phase. The coherent addition of fields gains a factor of two comparing to the incoherent addition of intensity. However, there are also non-cyclical terms, as shown in Figure 3-2 (a, b). If the non-cyclical path is reversed, it is still itself, representing the same physical scattering process in backscattering direction. It is possible to determine whether a term is cyclical by examining its representing paths as being automatically traced in the iteration. A close examination reveals that only two non-cyclical terms exist, as given in Figure 3-2 (a, b). These two terms are the directly volume backscattering Figure 3-2 (a) and the reflection followed by the backward scattering followed by reflection Figure 3-2 (b) in first order scattering. Both these terms involve the backward volume scattering in first order. This is true because for any higher order scattering, the scattering events of the succeeding scatterers could always reverse sequence to form a physically unique dual scattering path even in backscattering direction.

The cyclical correction of the radiative transfer results involves the identification of cyclical terms and the inclusion of a factor of two for the contribution from these terms. σ_{cyc} is used to denote contribution to backscattering from cyclical terms, and σ_{noncyc} to denote contribution from non-cyclical terms, then

$$\sigma = \sigma_{\mathrm{cyc}} + \sigma_{\mathrm{noncyc}} \tag{3-11a}$$

$$\sigma_{\mathrm{cor}} = 2\sigma_{\mathrm{cyc}} + \sigma_{\mathrm{noncyc}} = 2\sigma - \sigma_{\mathrm{noncyc}} \tag{3-11b}$$

where σ is the total volume backscattering without cyclical correction, and σ_{cor} is the corrected total volume backscattering. This cyclical correction only applies to co-polarization volume backscattering.

3.2.3 Numerical recipe in iteration

In this subsection, the author describe the numerical iterative approach, in particular how to evaluate the angular integral in equation (2a, 2b) or (9a - 9d), and the z- integral in equation (4a, 4b) or the definition of to $\bar{S}_c^{(n)}$, $\bar{S}_z^{(n)}$, $\bar{W}_c^{(n)}$, and $\bar{W}_z^{(n)}$.

First consider the typical angular integral of equation (9a). The author applied Gaussian-Legendre quadrature for θ-integral and trapezoidal quadrature for ϕ- integral. Considering the azimuthal symmetry of phase matrix $\bar{\bar{P}}(\theta, \phi; \theta', \phi')$ with respect to $\phi - \phi'$, the discretized version of equation (9a) reads

$$\bar{S}_u^{(n)}(\theta_k, \phi_p, z) = \Delta\phi \sum_{p'=1}^{N_p} \sum_{k'=1}^{N_k} a_{k'} \big[\bar{\bar{P}}(\theta_k, \phi_p - \phi_{p'}; \theta_{k'}, 0) \cdot \bar{I}^{(n-1)}(\theta_{k'}, \phi_{p'}, z)\big] \tag{3-12}$$

where θ_k $(k = 1, \dots, N_k)$ are the Gaussian-Legendre quadrature points, with $\mu_k = \cos(\theta_k)$ the positive half of the $2N_k$ roots of Legendre polynomial of $2N_k$-th order and a_k the corresponding Gaussian-Legendre quadrature weights at θ_k; $\phi_p = p\Delta\phi$ $(p = 0,1, \dots, N_p - 1)$ are the uniformly spaced trapezoidal quadrature points, with $\Delta\phi = 2\pi/N_p$. Note phase matrix $\bar{\bar{P}}(\theta, \phi; \theta', \phi')$ is only required at the grid points $\bar{\bar{P}}(\theta_k, \phi_p; \theta_{k'}, 0)$, and the summation over $\phi_{p'}$ in equation (12) forms a cyclical convolution, and could be accelerated by FFT.

Three kind of z-integrals are encountered in the form of $\int_{-d}^{0} dz' f(z')$ as in $\bar{S}_c^{(n)}$ and $\bar{W}_c^{(n)}$, $\int_{-d}^{z} dz' f(z')$ in $\bar{S}_z^{(n)}$ and $\int_{z}^{0} dz' f(z')$ in $\bar{W}_z^{(n)}$. The author sampled z uniformly at $z_q = -d + q\Delta z,\ \Delta z = d/N_q,\ q = 0,1,\dots,N_q,$ and denote $f(z_q)$ with f_q. Then $\int_{-d}^{0} dz' f(z')$ could be evaluated with trapezoidal quadrature rule directly,

$$\int_{-d}^{0} dz' f(z') = \Delta z \left(\frac{1}{2} f_0 + \sum_{q'=1}^{N_q - 1} f_{q'} + \frac{1}{2} f_{N_q} \right) \tag{3-13}$$

$\int_{-d}^{z_q} dz' f(z')$ and $\int_{z_q}^{0} dz' f(z')$ could be evaluated recursively,

$$\int_{-d}^{z_q} dz' f(z') = \int_{-d}^{z_q - 1} dz' f(z') + \frac{\Delta z}{2} (f_{q-1} + f_q), q = 1, \dots, N_q \tag{3-14}$$

$$\int_{z_q}^{0} dz' f(z') = \frac{\Delta z}{2} (f_q + f_{q+1}) + \int_{z_{q+1}}^{0} dz' f(z'), q = N_q - 1, \dots, 0 \tag{3-15}$$

with $\int_{-d}^{z_0} dz' f(z') = 0$ and $\int_{z_{N_q}}^{0} dz' f(z') = 0$.

Note the angular integral as illustrated in equation (12) is to be applied for any sampling point of z_q. An estimation criterion of typical numerical parameters is provided. The discretization number of θ_k, ϕ_p can be set as $N_k = 16$ and $N_p = 32$ for relatively smoothly changing phase matrix; the discretization number of z_q could be related to the optical thickness of snow layer $\tau = \kappa_e d$ by $N_q = \max(\tau/0.05, 8)$; the sufficient scattering order for the convergence of backscattering could be related to the optical thickness τ and the scattering albedo $\varpi = \kappa_s/\kappa_e$ as $\max(\varpi\tau/0.1, 5)$.

3.3 DISCUSSIONS ON THE DMRT SOLUTIONS

In this section, the scattering model of QCA with sticky spheres is applied to compute the phase matrix, extinction rate, and effective permittivity in snow at X- and Ku bands. The results of the iterative approach are then compared with the previous work [15] to illustrate the multiple scattering effects and backscattering enhancement effects.

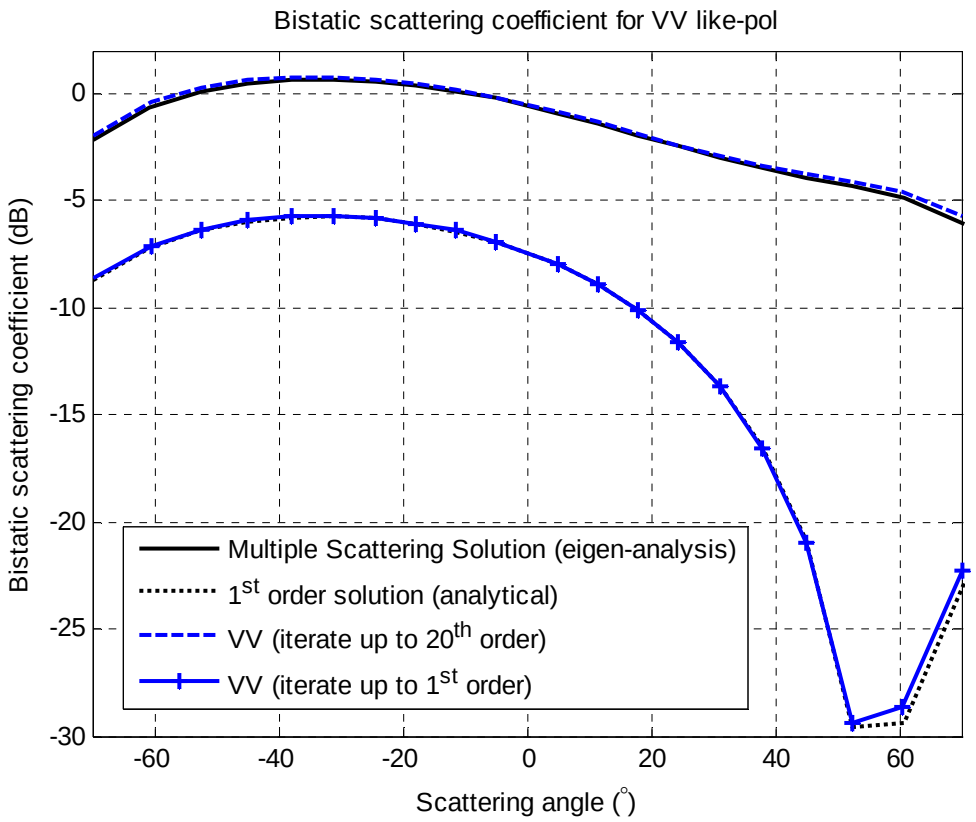

Figure 3-3 VV like-pol bistatic scattering coefficient without cyclical correction with grain size 1.4mm, frequency 17.5GHz, incidence angle 54˚, and snow depth 100cm.

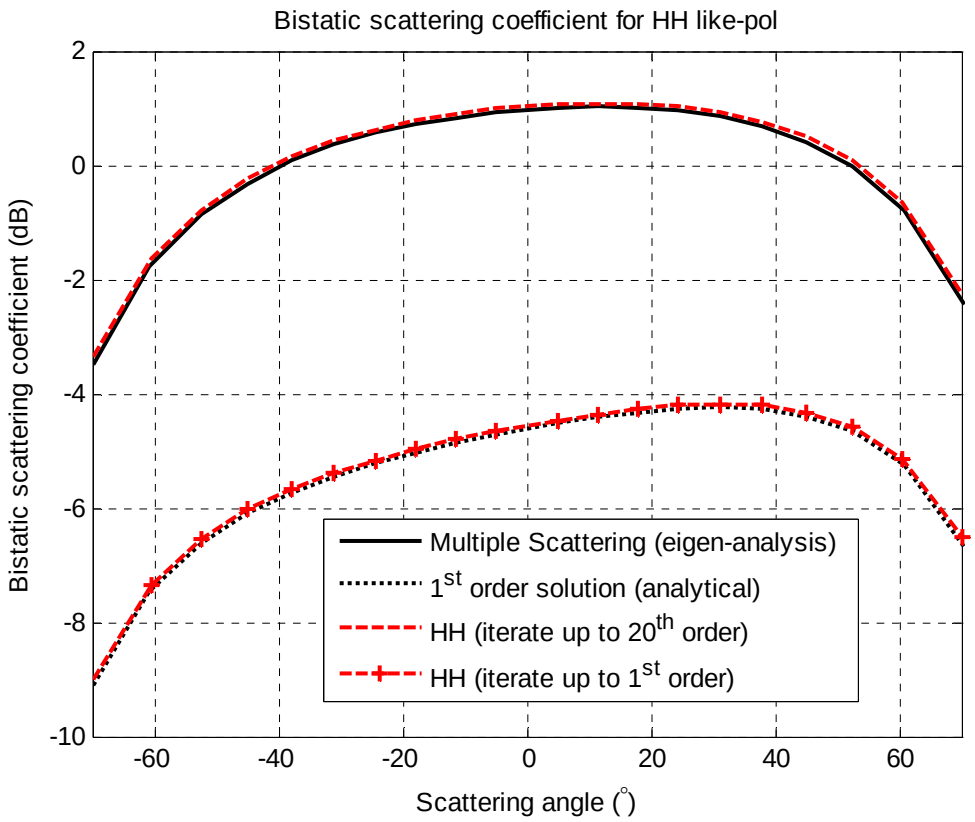

Figure 3-4 HH like-pol bistatic scattering coefficient without cyclical correction with grain size 1.4mm, frequency 17.5GHz, incidence angle 54˚, and snow depth 100cm.

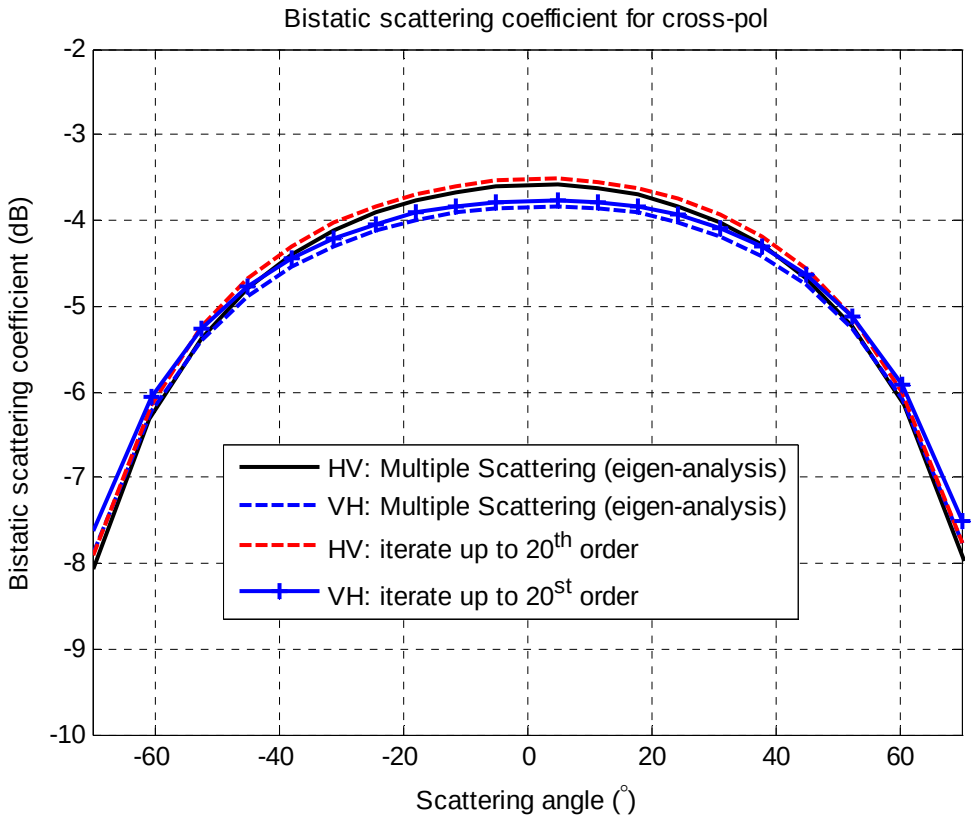

Figure 3-5 Cross-pol bistatic scattering coefficient without cyclical correction with grain size 1.4mm, frequency 17.5GHz, incidence angle 54˚, and snow depth 100cm.

The author considered a snowpack with thickness $d = 100cm$, snow fractional volume 25%, and ice particle grain diameter 1.4mm. The radar incidence angle is 54˚, and frequency is 17.5GHz. The ice permittivity is set to be 3.15 + 0.001i, and flat ground permittivity 3.2 + 0.002i. The QCA stickiness parameter is 0.1. The optical thickness $\tau = 1.98$, and scattering albedo $\varpi = 0.98$. The author carried out the numerical iteration up to 20th order. In Figure 3-3 to 3-5, the bistatic scattering coefficient on the incidence plane is compared against the analytical first order result [15] and the multiple scattering results using the quadrature eigenvalue analysis method [15]. Results agree very well as the cyclical correction is not included in the bistatic scattering. The contribution to backscattering from different orders with and without cyclical correction is

shown in Figure 3-6. Note that with QCA phase matrix there is no cross-pol in 1st order backscattering. So the accumulation bar diagram for cross-pol starts from the 2nd order. The author only applied cyclical correction hence backscattering enhancement to co-pols. The rate that the scattering order converges depends on the optical thickness and scattering albedo. In this case, contribution from the first ten orders is important. The cyclical correction to 1st order scattering is minor, since the two double bounce terms are small compared to volume scattering term. The cyclical correction to all the other orders doubles their contribution. Figure 3-7 is similar to Figure 3-6 but frequency is changed to X band (9.6GHz), where optical thickness $\tau = 0.29$, scattering albedo $\varpi = 0.96$. Convergence of backscattering coefficients is faster for this smaller optical thickness. The author iterated up to 5th order and contribution from the first three orders is important. It is clear that the first order scattering plays a more significant contribution in this thin optical thickness case, and the backscattering enhancement is even observable in 1st order for horizontal co-pol because of the increase of importance in the double bounce scattering.

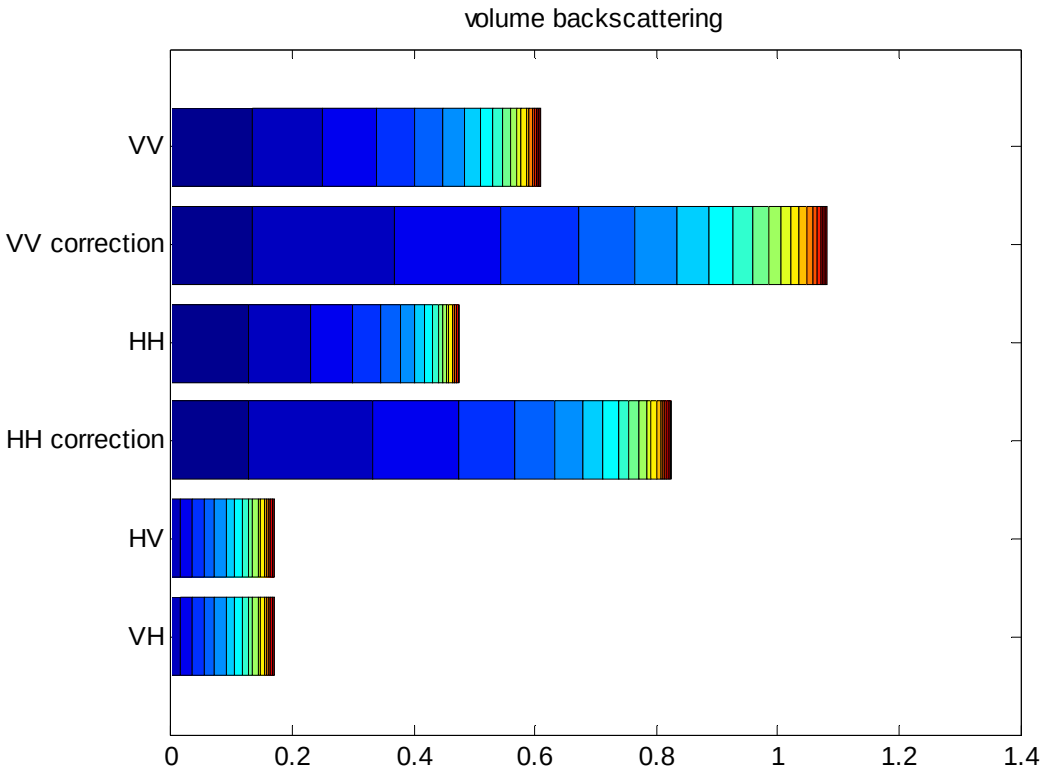

Figure 3-6 Contribution to volume backscattering with / without cyclical correction from each scattering order at 17.5 GHz. Sections of bars depict the relative effect of scattering orders from left (1st order for co-pol and 2nd order for cross-pol) to right (20th order).

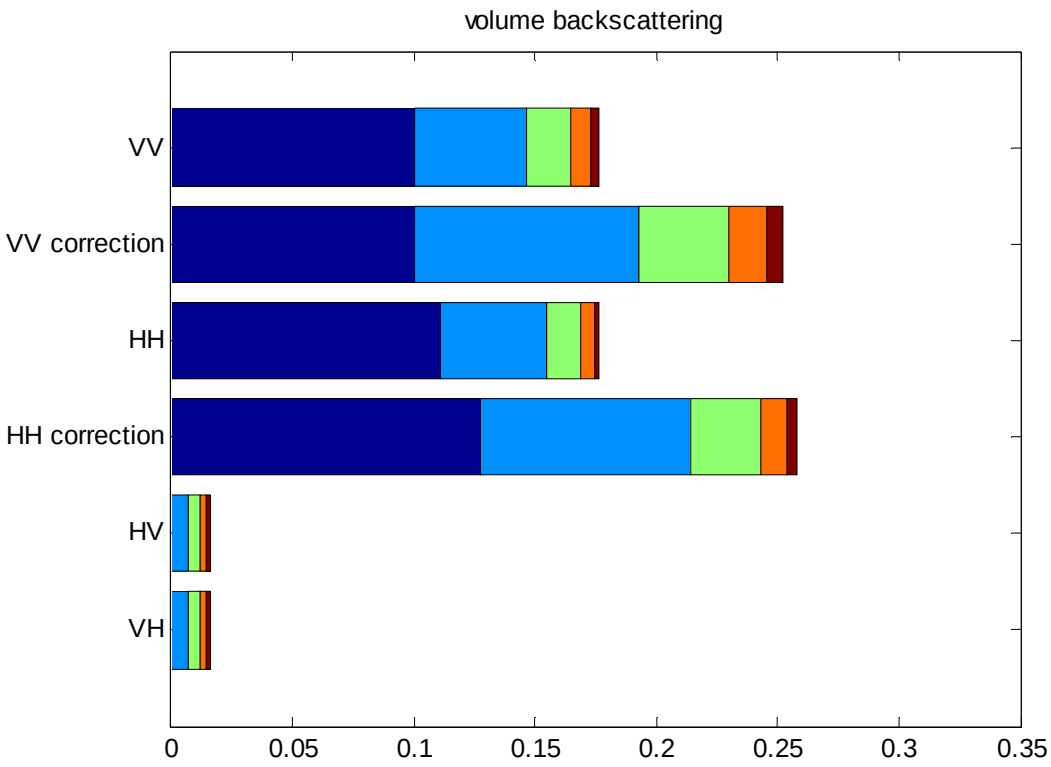

Figure 3-7 Contribution to volume backscattering with / without cyclical correction from each scattering order at 9.6 GHz. Sections of bars depict the relative effect of scattering orders from left (1st order for co-pol and 2nd order for cross-pol) to right (5th order).

3.4 MODEL VALIDATION WITH NOSREX CAMPAIGN

Finnish Meteorological Institute (FMI) has hosted the Nordic Snow Radar Experiment (NoSREx) campaign [8] [55] under an ESA contract for four successive winter seasons since November 2009 through May 2013. The NoSREx campaign was performed near the town of Sodankylä in northern Finland, about 100km north of the Arctic Circle. The objective of the campaign was to provide a continuous time series of coincidental active and passive microwave observations of snow cover, as part of Phase A studies for the proposed ESA CoReH2O mission. The main site for NoSREx activities is located at FMI Arctic Research Centre (FMI-ARC),

known as the Intensive Observation Area (IOA). The IOA hosts three experimental microwave instruments: SnowScat, Elbara-II and SodRad. SnowScat is a frequency scanning scatterometer operating from X- to Ku- band (10.2, 13.3 and 16.7GHz); Elbara-II is a radiometer operating at L band (1.4GHz); SodRad is another radiometer operating from X- to W- band (10.65, 18.7, 37 and 90 GHz). All these three microwave instruments are installed on tower, providing backscattering coefficients and brightness temperatures measurements at four incidence angles (30˚, 40˚, 50˚ and 60˚). The consolidated backscattering coefficients dataset of SnowScat is averaged over the full azimuth scan range. In situ measurements at IOA consist of manual snow pit measurements as well as extensive automated measurements on snow ground and metrological parameters. The area is mostly covered with sparse pine forest, as a representation of the typical Arctic boreal forest. The measurement sectors of the microwave instruments are located in a forest clearing. The location of the instruments, the approximate field of view of the instruments, and the location of manual snow pit observations are depicted in Figure 3-8.

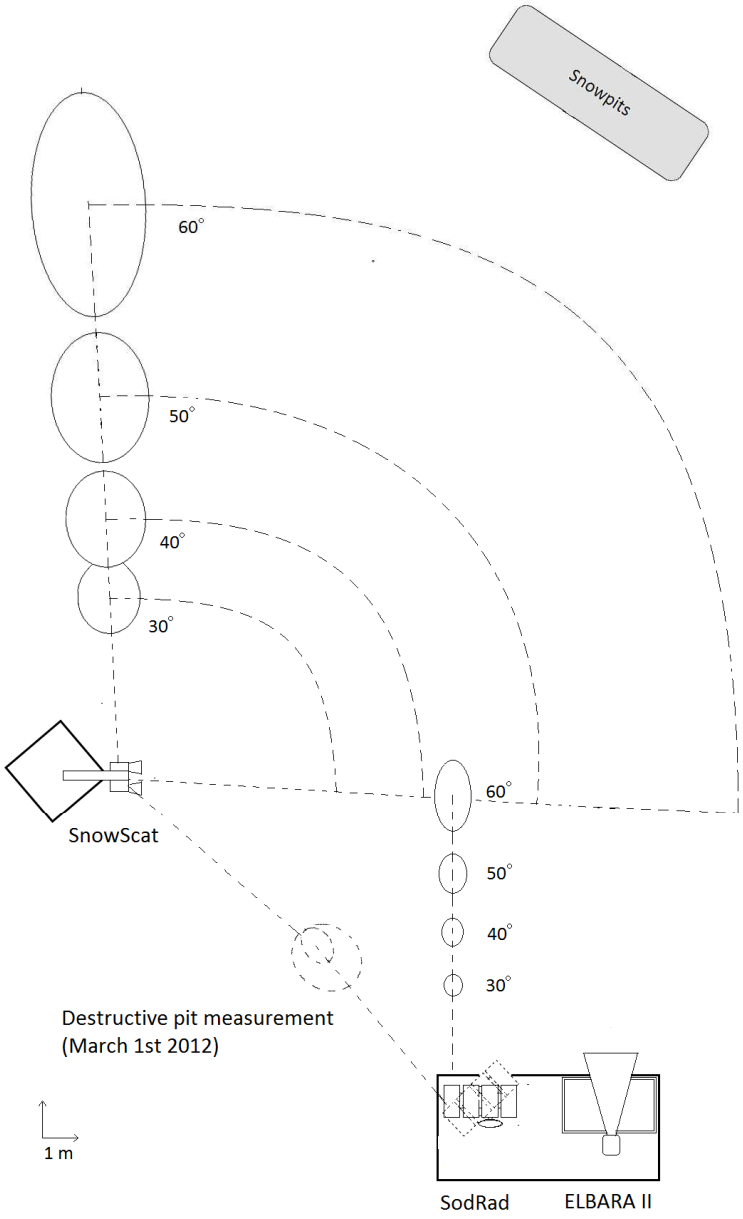

Figure 3-8 Schematic of NoSREx measurement setup including SnowScat scatterometer and SodRad and ELBARA II radiometer systems. Approximate location of SnowScat and SodRad 37 GHz receiver footprints at 30, 40, 50 and 60° incidence angles depicted.

Weekly snowpit measurements included the measurement of the snow temperature profile, measured using a digital thermometer at 10 cm vertical resolution, the snow density profile, measured using a manual scale at a 5 cm vertical resolution, as well as bulk snow density and SWE, using a large manual scale. Snow stratigraphy (layering) was identified visually and by use of a manual aid based of changes in snow hardness. The snow grain size and type were identified following Fierz et al. (2009). However, snow grain size was also analyzed in post-processing from macro photography, giving an approximate grain size for each layer at the precision of ¼ mm. A total of 31 snowpit measurements were made during the season of 2010-2011; 20 of these were made in dry snow conditions, between November 10th 2010, and March 29th, 2011. The grain size values represent the average of measured grain size values over the snowpack, weighted by the respective depth of each layer. The average grain size (of depth-weight values) in the dry snow period was 1.4 mm, with a standard deviation of 0.2 mm. The large standard deviation reflects observer errors which originate from the highly subjective measurement methodology. Nevertheless, the mean grain size reflects snowpack metamorphism and average conditions: the initial rise in mean grain size between November 2010 and January 2011 reflects an increase in snow grain size due to snow metamorphism. On the other hand, the slightly decreasing trend between January and March, 2011, reflects the increase of fine-grained snow through precipitation, decreasing the average grain size. Snow metamorphism continued in older snow layers also during this period.

Automated data from the site include measurements of air temperature, soil temperature at 2 cm depth, soil moisture at 2 and 10 cm depths, as well as snow depth. All automated data was recorded every ten minutes. The first snowfall of the season occurred on October 29th, 2010.

Temperatures on the following days remained above freezing point (up to +3°C) causing some initial melt of the fresh snowpack. However, from November 10th onwards, temperatures remained below zero until March 2nd, 2011, when temperatures rose to +1.7°C. Similar short periods of above-zero temperatures were experienced on several occasions in March. Initial cold temperatures in November, combined with a relatively shallow snowpack of < 20 cm resulted in a rapid freezing of the soil. Low values of measured volumetric soil moisture (< 0.05 m3/m3), after mid-November in Figure 3-2 reflect the low permittivity of frozen soil measured by the soil moisture probes. Major precipitation events (10 cm or over increase in snow depth) were experienced on December 8th, January 17th, and March 14th. Sustained periods of snowfall lasting several days occurred between 30 December, 2010 and January 8th, 2011 as well as between January 31st and February 8th, 2011. A maximum snow depth of 80 cm (ca. 170 mm in SWE) was reached in March.

In this section, the SnowScat backscattering coefficients observation at three frequencies ranging from X- to Ku- band (10.2, 13.3 and 16.7GHz) and the SodRad brightness temperature observation at three frequencies ranging from X- to Ka- band (10.65, 18.7 and 37GHz) are selected to compare with model prediction. Five representative dates with backscattering coefficients, brightness temperature observations and snow pit measurements collected during the winter season of 2010 to 2011 are chosen. Brightness temperature and backscattering coefficients collected at 40˚ incidence angle are used. The iterative approach with cyclical correction is used to compute backscattering coefficient, and a separate passive DMRT code [48] based on quadrature eigenvalue analysis is used to compute brightness temperature with multiple scattering effects. The bicontinuous media / DDA scattering model is used to compute the phase

matrix, effective permittivity, and extinction rate of snowpack. The same bicontinuous media parameter is applied to both active and passive models for all the six microwave channels. The bulk density and thickness of the snowpack is taken directly from the ground measurement. The ground is assumed to be rough with rms height of 1mm and exponential correlation length of 4mm. The ground relative permittivity is set to be $3.0 + 0.001i$. The surface backscattering is taken from a pre-built lookup table based on numerical solution of Maxwell equations in 3D (NMM3D) [30] [31] [56] and then attenuated by the snow layer. The vertical co-polarization backscattering coefficients is plotted versus SWE and compared against measurement in Figure 3-9. The brightness temperature is plotted against SWE in Figure 3-10 to 3-12 for three different passive frequencies, respectively. It is promising to observe that one set of physical parameters, when feeding into physical scattering models, could match microwave measurements in all six channels, for both active and passive. Without the cyclical correction, the model prediction of brightness temperature would be too low if the backscattering coefficients get agreement. The backscattering coefficients and brightness temperature is again plotted against frequency for data taken on Jan. 12, 2011 in Figure 3-13 and 3-14 respectively to illustrate typical frequency dependence. The measured snowpack properties such as mean grain size, bulk density, and the defining parameters of the bicontinuous media $\langle\zeta\rangle$ and b are also listed in Table 3-1. The bicontinuous media $\langle\zeta\rangle$ and b are derived in a similar way as documented in [49].

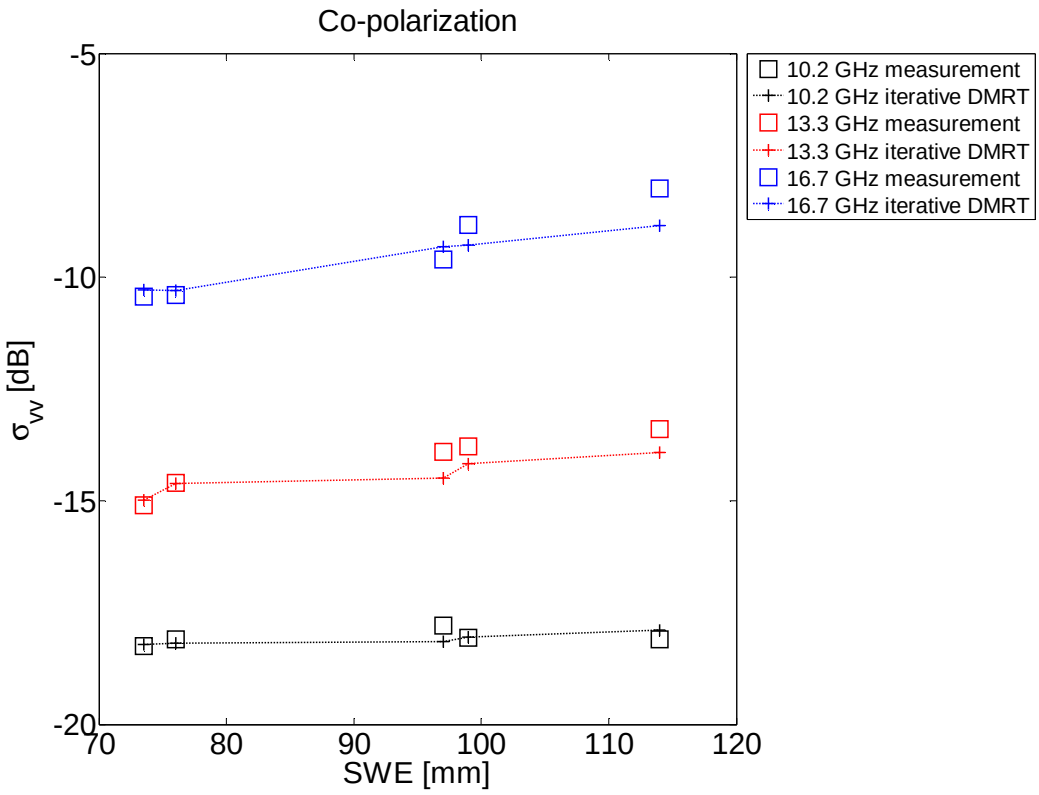

Figure 3-9 Radar backscattering coefficients against SWE for vertical co-pol

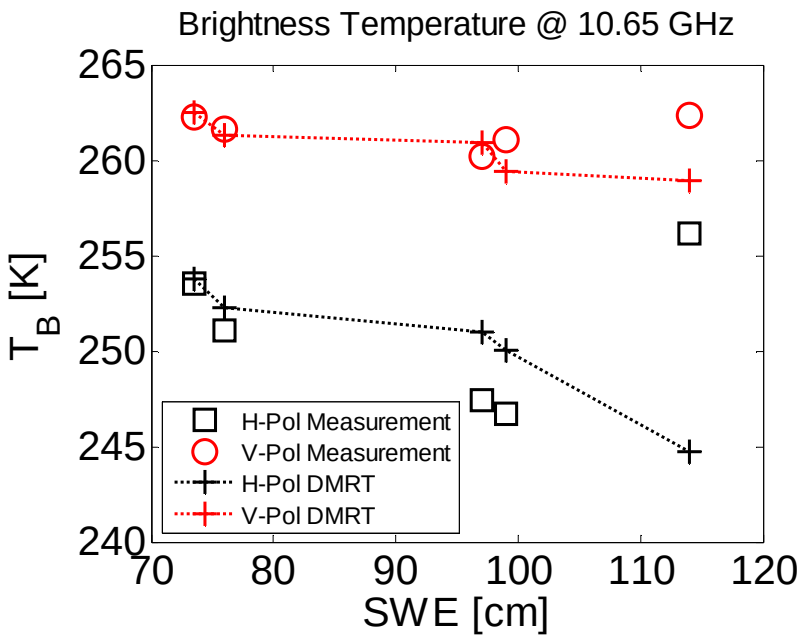

Figure 3-10 Brightness temperature against SWE at 10.65GHz

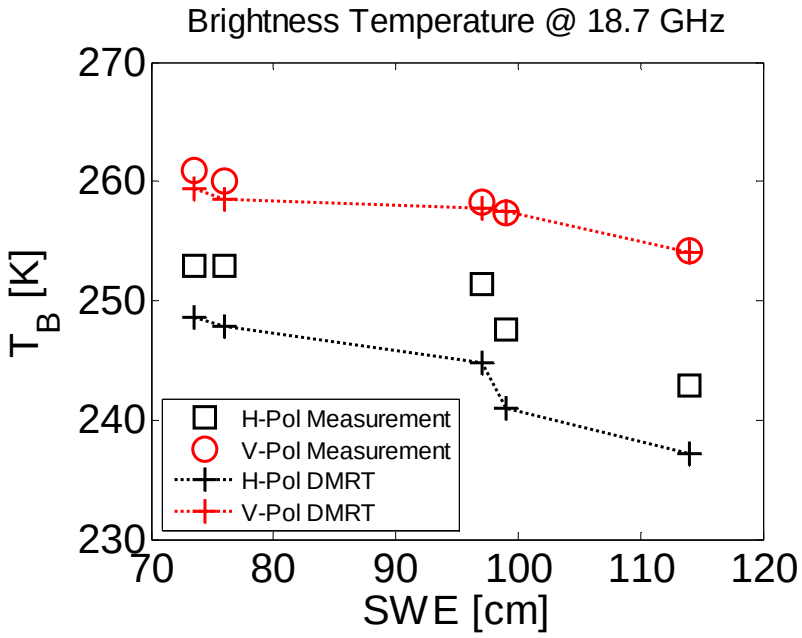

Figure 3-11 Brightness temperature against SWE at 18.7 GHz

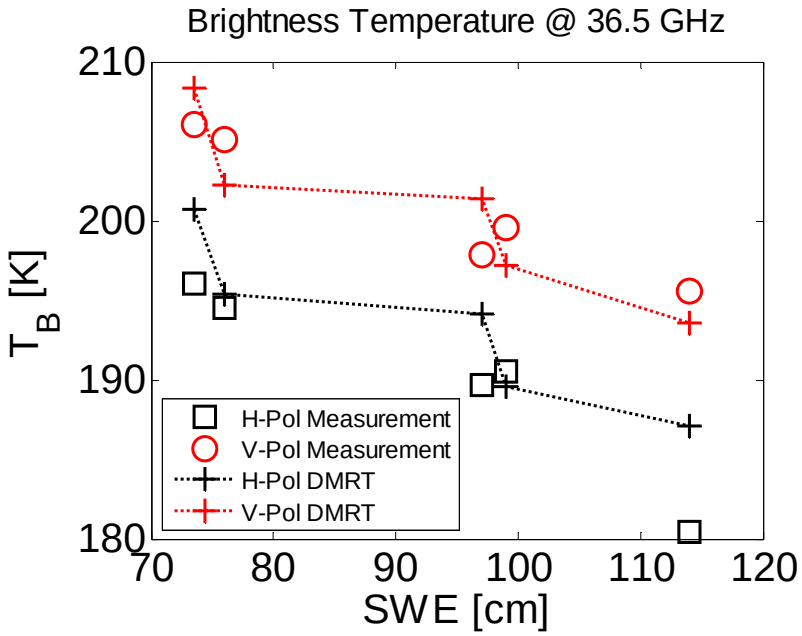

Figure 3-12 Brightness temperature against SWE at 36.5 GHz

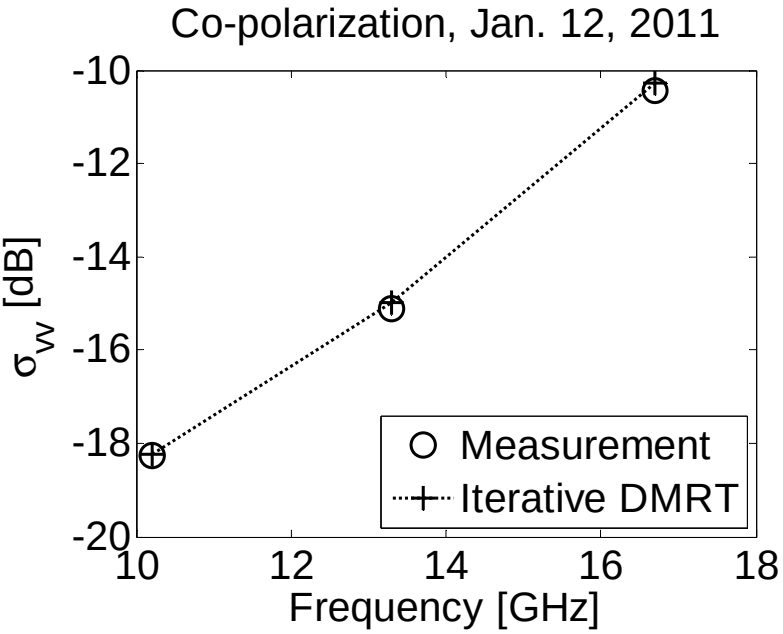

Figure 3-13 Radar backscattering coefficients against frequency for data taken on Jan. 12, 2011

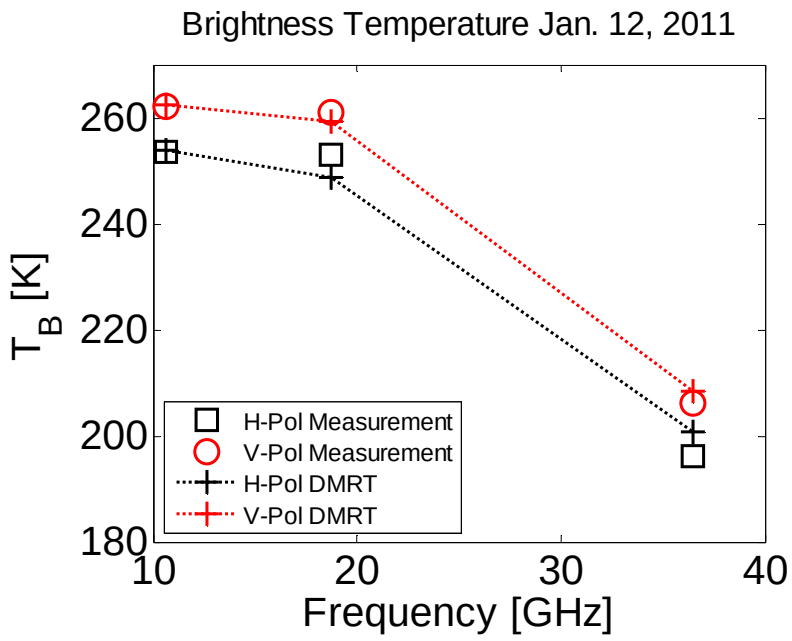

Figure 3-14 Brightness temperature against frequency for data taken on Jan. 12, 2011

Table 3-1 Snowpack properties and bicontinuous media parameters

	Mean grain size [mm]	Density [g / cc]	$\langle\zeta\rangle$ $[m^{-1}]$	b
Jan. 12	3.0	0.163	10000	2.0
Jan. 18	2.8	0.152	10000	1.2
Feb. 01	4.0	0.180	9000	1.5
Feb. 08	2.0	0.143	11000	1.0
Mar. 01	2.0	0.193	11000	2.0

3.5 CONCLUSIONS

Backscattering enhancement effects become essential when both active and passive microwave observation of snowpack are examined at the same time. It increases backscattering coefficients without decreasing brightness temperature. A new approach of solving vector DMRT equation with inclusion of cyclical terms using iterative approach numerically is proposed. This approach naturally allows accounting for multiple scattering effects by accumulation of scattering orders. It also allows the identification of cyclical terms and separate out their contribution. The cyclical correction of the contribution from cyclical terms enables vector radiative transfer theory to agree with wave approach in co-pol backscattering coefficient. The DMRT equation is solved using this numerical iterative approach with cyclical correction for two reflective boundaries to predict backscattering coefficients. Backscattering enhancement effects always play an important role in high order scattering, and with reflective boundaries, this is even observable in first order scattering results. A separate passive DMRT code with quadrature eigenvalue analysis to include multiple scattering effects is applied to compute brightness temperature. The scattering models of QCA with sticky particles and bicontinuous media / DDA are used to compute phase matrix, extinction coefficient and effective permittivity. The bicontinuous media modeling of snow medium, when combined with the DMRT models, gets agreement with both passive and active observations from the NoSREx campaign. The agreement is achieved for six channels simultaneously with the same set of physical parameters of snowpack.

CHAPTER 4: MICROWAVE SCATTERING AND MEDIUM CHARACTERIZATION FOR TERRESTRIAL SNOW WITH QCA-MIE AND BICONTINUOUS MODELS: COMPARISONS STUDIES

4.1 INTRODUCTION

The Snow Water Equivalent (SWE) represents the water storage in the form of snow on earth, and the estimation of SWE is important for management of water resources on earth and the prediction of climate change. Active and passive microwave remote sensing have been used to retrieve the snow water equivalent. Passive sensors include AMSR-E and AMSR2 [4]. Active sensors have drawn considerable interests recently. The Constellation of small Satellites for the Mediterranean basin Observation-SkyMed (COSMO-S) has a SAR sensor at X band [5]. The Cold Regions Hydrology High-Resolution Observatory (CoReH2O) was a satellite mission proposed but not selected by ESA [2] [6]. The Tier-3 decadal satellite mission of National Aeronautics and Space Administration (NASA) – Snow and Cold Land Processes (SCLP) utilizes active microwave SAR at Ku band and X band similar to the CoReH2O design, and has included dual-frequency (18.7 / 36.5 GHz) passive microwave radiometers [1]. NASA has supported the Cold Land Process Experiments (CLPX). ESA has also sponsored several field campaigns to acquire data for algorithm development. There were ground-based SnowScat [8] and airborne SnowSAR (X- and Ku-band) campaigns [3] [7] in Finland. SnowSAR measurements have been made in Alaska and Canada. Extensive ground measurements were also taken during these campaigns.

In snow, the ice particles are packed closely and there are thousands of ice grains packed in a one-wavelength cube at the microwave frequencies. As the propagation and scattering of

electromagnetic waves are coherent within distances of several wavelengths, the ice grains in snow do not scatter independently. In the Dense Media Radiative Transfer theory (DMRT), the collective scattering and wave interaction effects of densely packed ice grains are taken into account. The analytic model of Quasi-Crystalline Approximation (QCA) [11] [12] [18] was first introduced. In the medium characterization, the particles are assumed to be densely packed and can also adhere together to form aggregates. Because the aggregates are no longer much smaller than one wavelength, the Mie scattering's T matrices are used in the QCA model, making it a QCA-Mie-DMRT model. Salient features of the QCA-DMRT are: Firstly, the frequency dependence can be much weaker than independent scattering. Secondly, the phase matrix has more forward scattering than the Rayleigh phase matrix because of the aggregation effects. The strong forward scattering is also a feature that is assumed in the HUT Model [28] [29]. The MEMLS [24] [25] assumes a Rayleigh phase matrix. Recently, 3D computer simulations of microstructures of snow based on the bicontinuous model are used to resemble that of real snow. 3D numerical solutions of Maxwell equations are computed using DDA for the automatically-generated snow.

In snow microstructure characterizations, the QCA model uses single size, single size with stickiness, and multiple sizes. The correlations of particle positions are described by the pair distribution functions, and the Percus-Yevick pair distribution functions will be used. In bicontinuous medium, the model parameters $\langle\zeta\rangle$ and b will be used. From the bicontinuous wavenumber distribution, the correlation function can be derived. A key question in snow scattering model is how to obtain model parameters from ground snow measurements. Measurements of single grain size, multiple grain sizes, and SSA have been made. If a digitized picture of snow is obtained, the correlation function can be derived. Vallese and Kong studied

the correlation functions of snow and ice samples [19]. If the correlation function is examined close to the origin, the correlation function is close to exponential function. The correlation length as derived in this manner is small between 0.2 mm to 0.4 mm. When substituted such small correlation length into the physical model, it gives Rayleigh scattering and Rayleigh phase function.

In this chapter, two dense media models – the QCA particle model and the bicontinuous model are compared. For the QCA model, the single size with stickiness, and the multiple sizes are used. For the bicontinuous model, Gamma distributions are used to describe the wavenumber's probability distributions. Then the extinction coefficients and the phase matrix are compared. The correlation functions can be derived from the pair distribution functions. These can be performed in the spatial domain or in the Fourier transform domain. Based on the pair distribution functions, the derived correlation functions have tails that agree with the correlation functions of bicontinuous model. Both models are different from the exponential correlation functions which do not have tails. Because scattering depends strongly on size, the tails of correlation functions contribute to varied scattering behavior that depart from Rayleigh scattering and Rayleigh phase functions.

In Section 4.2, the scattering properties of QCA model and bicontinuous model are compared by computing the phase matrices, extinction coefficients, and mean cosine of scattering. The case of multi-size QCA and the bicontinuous model are particularly compared. In particular, the size distribution of QCA whose frequency dependence matches bicontinuous model will be shown. In Section 4.3, the pair distribution functions are used to derive the correlation functions of QCA model. The results are cast in the spatial domain and the Fourier transform domain. In Section 4.4, using the Percus-Yevick pair distribution functions, the covariance functions of exponential,

single size with stickiness, and multiple sizes are shown. They are compared with the covariance function of bicontinuous medium, particularly paying attention to the tails of the correlation functions. In particular, a multi-size case is selected such that it matches the bicontinuous correlation function asymptotically in the tail. In Section 4.5, methods are suggested on how input parameters of QCA model and bicontinuous model can be obtained from ground measurements.

4.2 SCATTERING PROPERTIES OF QCA AND BICONTINUOUS MODELS

First the phase matrices in the 1-2 frame are compared. 1-2 frame is defined as the plane formed by the incident and scattered directions [32]. The co-polarization phase matrices are $P_{ii}(\Theta)$ $(i = 1,2)$ and the cross polarization phase matrices are $P_{ij}(\Theta)$ $(i \neq j)$, where Θ is the angle between the incident and the scattered directions. $\Theta = 0$ represents forward scattering direction, while $\Theta = \pi$ represents backscattering direction. However, the 1 and 2 unit vectors are not constant in space. Consider incident wave in $\hat{z}$ direction, and let polarization be $\bar{E}_{inc} = \hat{x}$. Let the scattered wave be in the direction $\hat{k}_s = \sin\theta_s \cos\phi_s\ \hat{x} + \sin\theta_s \sin\phi_s\ \hat{y} + \cos\theta_s\ \hat{z}$. Then in 1-2 frame

$\begin{aligned} \cos\Theta &= \cos\theta_s \\ \Theta &= \theta_s \end{aligned}$	(4-1a)
$\hat{1}_i = \hat{1}_s = -\cos\ \phi_s\hat{y} + \sin\ \phi_s\hat{x}$	(4-1b)
$\hat{2}_i = \hat{k}_i \times \hat{1}_i = \cos\ \phi_s\hat{x} + \sin\ \phi_s\hat{y}$	(4-1c)

Therefore the electric fields in 1-2 directions are

$E_{1i} = \sin\phi_s$	(4-2a)

$$E_{2i} = \cos\ \phi_s$$

$$\begin{aligned} E_{1s} &= f_{11}(\theta_s)\sin\ \phi_s + f_{12}(\theta_s)\cos\ \phi_s \\ E_{2s} &= f_{21}(\theta_s)\sin\ \phi_s + f_{22}(\theta_s)\cos\ \phi_s \end{aligned} \quad \text{(4-2b)}$$

The square of the magnitude of the scattered electric fields are

$$|E_{1s}|^2 = |f_{11}(\theta_s)|^2\sin^2\ \phi_s + |f_{12}(\theta_s)|^2\cos^2\ \phi_s + 2\mathrm{Re}\big(f_{11}(\theta_s)f_{12}^*(\theta_s)\big)\sin\ \phi_s\cos\ \phi_s \quad \text{(4-2c)}$$

$$|E_{2s}|^2 = |f_{21}(\theta_s)|^2\sin^2\ \phi_s + |f_{22}(\theta_s)|^2\cos^2\ \phi_s + 2\mathrm{Re}\big(f_{21}(\theta_s)f_{22}^*(\theta_s)\big)\sin\ \phi_s\cos\ \phi_s \quad \text{(4-2d)}$$

In the angular integration, the cross terms integrate to zero. So the scattering coefficients is [32]

$$\kappa_S = \frac{1}{V}\int_0^{\pi} d\theta_s \sin\theta_s \int_0^{2\pi} d\phi_s(|E_{1s}|^2 + |E_{2s}|^2) \quad \text{(4-3a)}$$

$$\kappa_s = \frac{1}{V}\pi \int_0^{\pi} d\Theta \sin\Theta[|f_{11}(\Theta)|^2 + |f_{12}(\Theta)|^2 + |f_{21}(\Theta)|^2 + |f_{22}(\Theta)|^2] \quad \text{(4-3b)}$$

$$\kappa_s = \pi \int_0^{\pi} d\Theta \sin\Theta[|P_{11}(\Theta)|^2 + |P_{12}(\Theta)|^2 + |P_{21}(\Theta)|^2 + |P_{22}(\Theta)|^2] \quad \text{(4-3c)}$$

Mean cosine ($\bar{\mu}$) describes the angular distribution of phase matrices. It is defined as

$$\bar{\mu} = \frac{\int_0^{\pi} d\Theta \sin\Theta \cos\Theta\ [P_{11}(\Theta) + P_{12}(\Theta) + P_{21}(\Theta) + P_{22}(\Theta)]}{\int_0^{\pi} d\Theta \sin\Theta\ [P_{11}(\Theta) + P_{12}(\Theta) + P_{21}(\Theta) + P_{22}(\Theta)]} \quad \text{(4-4)}$$

The value $\bar{\mu} = 0$ represents dipole scattering pattern or Rayleigh scattering function. $\bar{\mu} = 1.0$ represents all power is scattered to the forward scattering direction. In the HUT model, $\bar{\mu}$ is empirically selected as 0.96 [28] [29], which is corresponding to very strong forward scattering effect.

4.2.1 QCA model

In QCA model, the cases are single size, single size with stickiness, multi-size, and multi-size with stickiness. In the single-size sticky case, the two parameters are the grain size or the diameter of spherical particle, and the stickiness parameter τ which controls the degree of bonding between particles [12] [42]. The stickiness parameter τ ranges from 0.1 to infinity. As τ decreases, the particles tend to bond stronger into larger aggregates within the medium. For $\tau = \infty$, the sticky case becomes the non-sticky case. In the multi-size case, the parameters are a size distribution. Three cases of dense media with particle size distributions are considered: Gamma distribution $p_G(d)$, log-normal distribution $p_L(d)$ [57], and inverse-Gamma distribution $p_I(d)$.

$$p_G(d) = \frac{\beta+1}{\Gamma(\beta+1)\langle d\rangle}\left[(\beta+1)\frac{d}{\langle d\rangle}\right]^{\beta}\exp\left[-(\beta+1)\frac{d}{\langle d\rangle}\right]$$	(4-5a)
$$p_L(d) = \frac{1}{d\sqrt{2\pi}\sigma}\exp\left[-\frac{(\ln d - \ln\langle d\rangle)^2}{2\sigma^2}\right]$$	(4-5b)
$$p_I(d) = \frac{1}{\Gamma(\beta+2)\langle d\rangle}\left[(\beta+1)\frac{\langle d\rangle}{d}\right]^{\beta+2}\exp\left[-(\beta+1)\frac{\langle d\rangle}{d}\right]$$	(4-5c)

where $\langle d\rangle$ is the mean size, σ is the shape parameter for log-normal distribution, and β is the shape parameter for both Gamma and inverse-Gamma distributions. Given the size distribution, one discretizes it into multiple sizes based on the discrete sizes. Then the corresponding Percus-Yevick pair distribution functions are used in the QCA model. The scattering properties of QCA model are described in [12].

4.2.2 Bicontinuous model

For the bicontinuous model, the microstructure of medium is generated as follows [13]. Let $S(\bar{r})$ be equal to a summation of N random sinusoidal waves where N is a large number:

$$S(\bar{r}) = \frac{1}{\sqrt{N}} \sum_{n=1}^{N} \cos(\bar{\zeta}_n \cdot \bar{r} + \varphi_n) \quad (4\text{-}6)$$

where the wavenumber vector $\bar{\zeta}_n$ and the phase term φ_n are both random variables. The magnitude of wavenumber ζ_n follows a probability distribution $p(\zeta)$ ranging from 0 to $+\infty$. It is assumed that directions of wavenumber vector $\bar{\zeta}_n$ are uniformly distributed over a unit spherical surface. The phase φ_n follows uniform distribution between 0 and 2π. The he computed value of $S(\bar{r})$ at $\bar{r}$ is then compared with a cutting level α given by

$$\alpha = \mathrm{erf}^{-1}(1 - 2f_V) \quad (4\text{-}7)$$

where $\mathrm{erf}^{-1}(.)$ is the inverse error function. The comparison between $S(\bar{r})$ and α will determine the material to be filled at the point $\bar{r}$ according to the indicator function

$$\Theta(\bar{r}) = \begin{cases} 1, S(\bar{r}) > \alpha, (\text{ice}) \\ 0, S(\bar{r}) < \alpha, (\text{air}) \end{cases} \quad (4\text{-}8)$$

The same process is repeated for every lattice point within the whole simulation volume. After each lattice point is filled, one realization of random snow medium is generated. Monte Carlo simulation will be done for the random snow medium, by solving the volume integral equation and the Discrete Dipole Approximation (DDA), which is further sped up by FFT [11]. The incoherent scattering intensity will then be extracted from the scattering fields of these realizations. Finally the phase matrices, extinction coefficient, and mean cosine are computed.

Bicontinuous model is also related to QCA multi-size model. Let

$\zeta = Cd^{-1}$	(4-9)

where C is a constant and d is the diameter. Therefore the probability distribution of size is $\tilde{p}(d) = Cd^{-2}p(Cd^{-1})$. Thus, Gamma wavenumber distribution $p_G(\zeta)$ is corresponding to inverse-Gamma size distribution $p_I(d)$, log-normal wavenumber distribution $p_L(\zeta)$ is corresponding to log-normal size distribution $p_L(d)$.

$p_G(\zeta) = \frac{b+1}{\Gamma(b+1)\langle\zeta\rangle}\left[(b+1)\frac{\zeta}{\langle\zeta\rangle}\right]^b \exp\left[-(b+1)\frac{\zeta}{\langle\zeta\rangle}\right]$	(4-10a)
$p_L(\zeta) = \frac{1}{\zeta\sqrt{2\pi}\sigma}\exp\left[-\frac{(\ln\zeta - \ln\langle\zeta\rangle)^2}{2\sigma^2}\right]$	(4-10b)
$p_I(\zeta) = \frac{1}{\Gamma(b+2)\langle\zeta\rangle}\left[(b+1)\frac{\langle\zeta\rangle}{\zeta}\right]^{b+2} \exp\left[-(b+1)\frac{\langle\zeta\rangle}{\zeta}\right]$	(4-10c)

where $\langle\zeta\rangle = C\langle d\rangle^{-1}$ representing the mean value of ζ.

4.2.3 Comparison among QCA multi-size, QCA sticky, and bicontinuous model

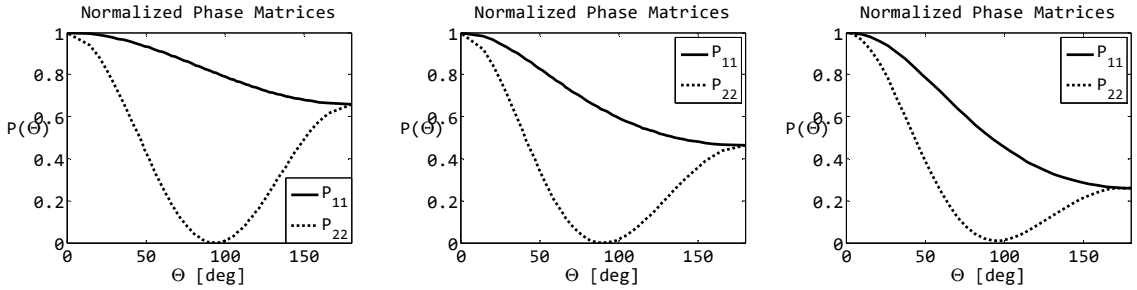

(a) (d) (g)

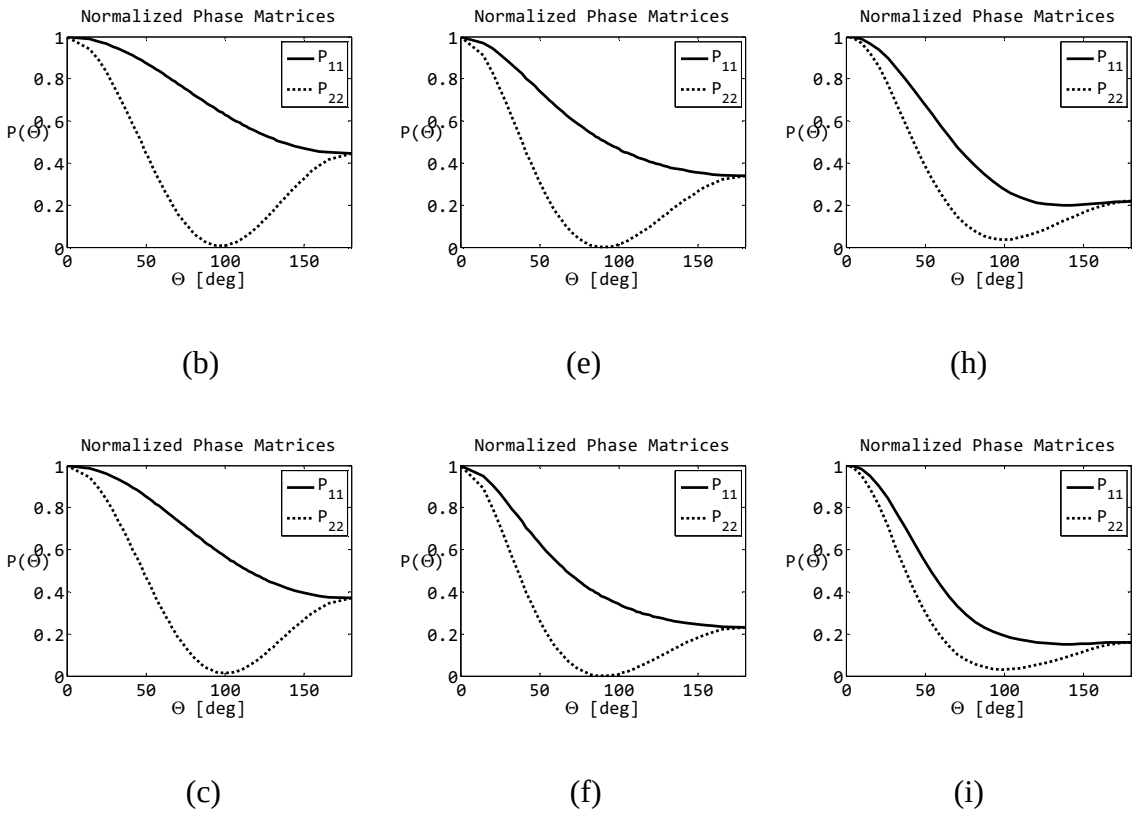

Figure 4-1 Normalized co-polarization phase matrices of QCA multi-size, QCA sticky and bicontinuous models.

Left column – QCA multi-size: (a) 10.0 GHz (b) 13.0 GHz (c) 17.0 GHz

Middle column – QCA sticky: (d) 10.0 GHz (e) 13.0 GHz (f) 17.0 GHz

Right column – Bicontinuous: (g) 10.0 GHz (h) 13.0 GHz (i) 17.0 GHz

In Figure 4-1 the normalized co-polarization phase matrices $\tilde{P}_{ij}(\Theta)$ are plotted for QCA multi-size, QCA sticky and bicontinuous model at three frequencies (10.0, 13.0, 17.0 GHz) as a function of Θ.

$$\tilde{P}_{ij}(\Theta) = \frac{P_{ij}(\Theta)}{\max_{\Theta} P_{ij}(\Theta)} (i,j = 1,2) \quad (4\text{-}11)$$

The parameters are: for QCA multi-size model, $\langle d \rangle = 1.0$ mm, $\beta = 4.0$, and the twenty sizes are equally spaced between 0.1 mm and 7.0 mm; for bicontinuous model, $\langle \zeta \rangle = 4500$ m^{-1}, $b = 0.5$; and for sticky particle model, grain size (diameter) = 1.0 mm, $\tau = 0.1$; and the fraction volume is 30%. Each of the phase matrices is normalized by its maximal value, or $P(\Theta = 0)$. All the phase matrices shown in Figure 4-1 exhibit moderate forward scattering effect, which is the major difference between dense medium model and Rayleigh scattering model in which the phase matrices are $P_{11}(\Theta) = 1$ and $P_{22}(\Theta) = \cos^2 \Theta$. It is also seen that the forward scattering effect becomes stronger as the frequency increases. This is because with a fixed physical size of ice grain, its electrical size increases with increasing frequency, hence the stronger forward scattering.

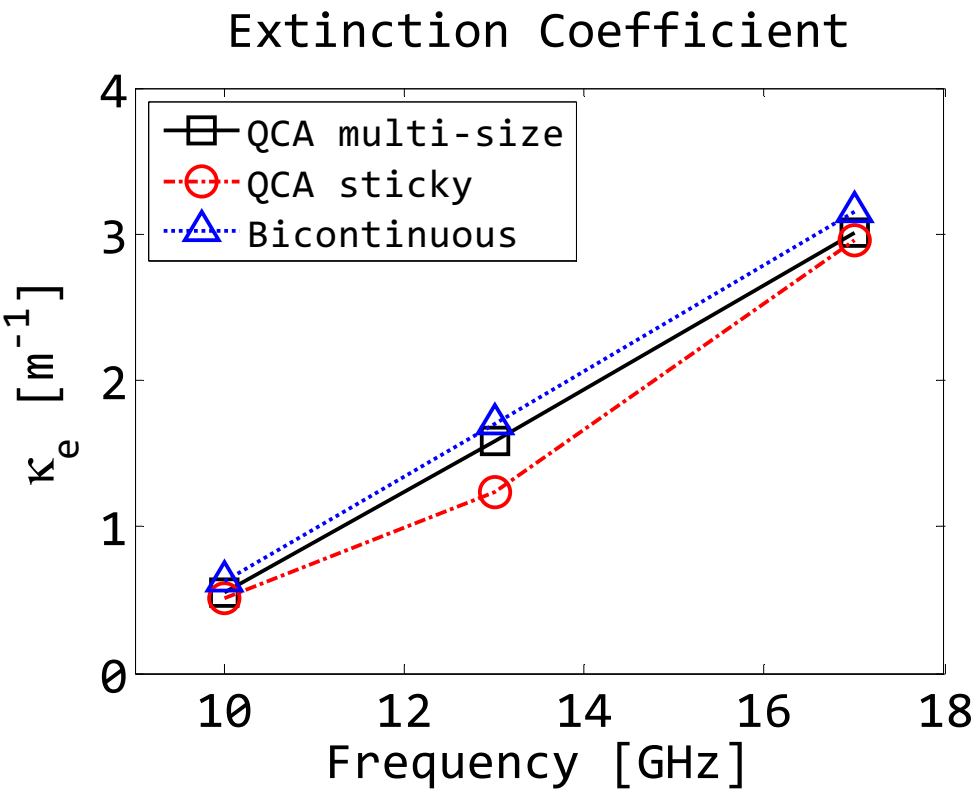

Figure 4-2 Extinction coefficients of QCA multi-size, QCA sticky and bicontinuous models.

Figure 4-2 illustrates the respective extinction coefficients of QCA multi-size, QCA sticky, and bicontinuous models. The model parameters are the same as those used in Figure 4-1. The extinction coefficients of all three models increase as frequency increases. Frequency dependence is extracted from the extinction coefficients at 10.0 and 17.0 GHz. QCA multi-size gives 3.2, QCA sticky models gives 3.3, and bicontinuous model gives 3.1. All of thee power law are lower than Rayleigh scattering model of 4.0.

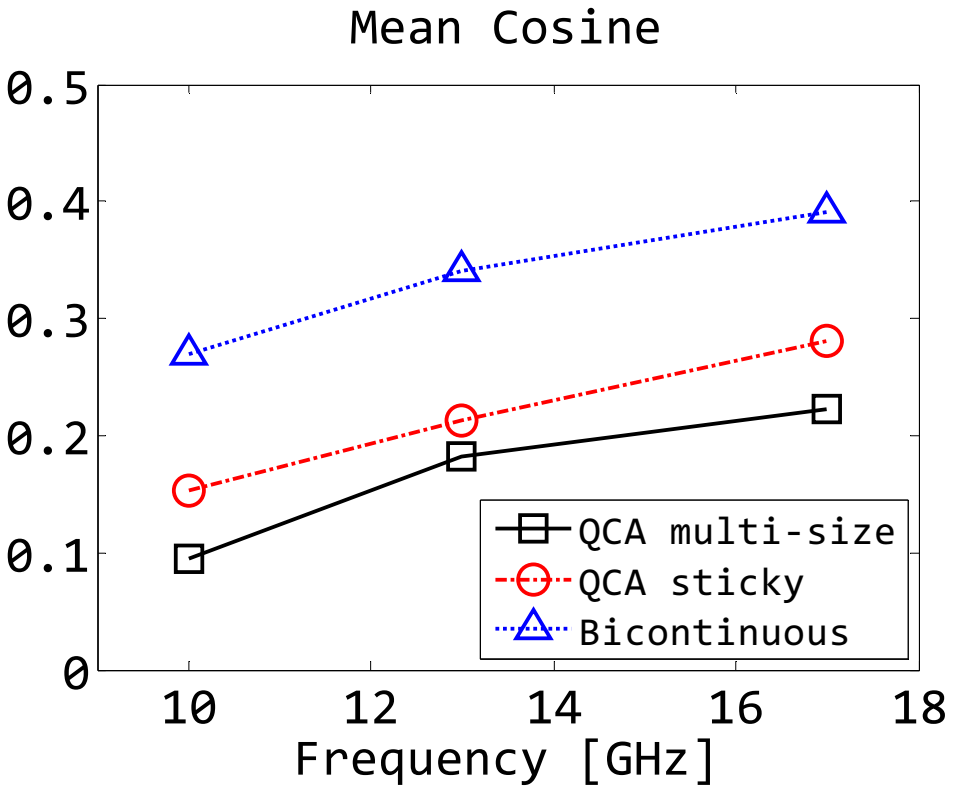

Figure 4-3 Mean cosine of QCA multi-size, QCA sticky and bicontinuous models.

The numerical values of the mean cosine derived from the phase matrices for three frequencies, are illustrated in Figure 4-3. The model parameters are the same as those used in Figure 4-1 and 4-2. It is seen that mean cosine increases with frequency for all three models. As frequency increases, electrically larger aggregation gives stronger forward scattering, and thus larger mean

cosine $\bar{\mu}$. All the values of mean cosine are between 0.1 and 0.4, which shows the moderate forward scattering effect.

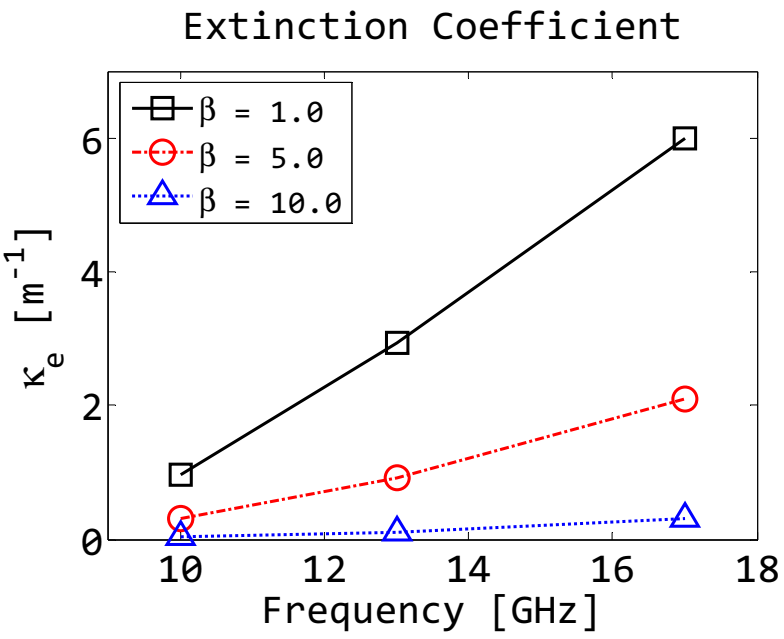

(a)

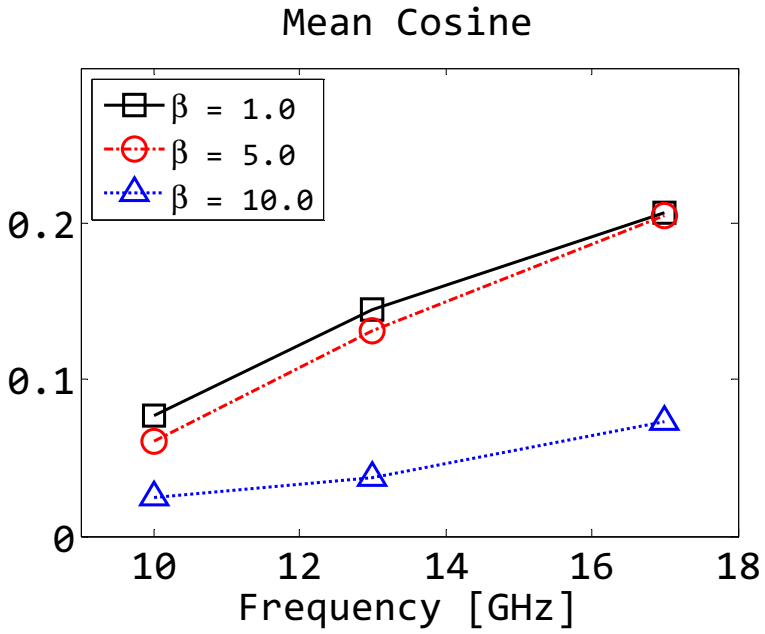

(b)

Figure 4-4 Scattering properties of QCA multi-size model

(a) extinction coefficient (b) mean cosine

Figure 4-4 illustrates the scattering properties of QCA multi-size model with different model parameters. The average grain size is fixed at 1.0 mm, but the values of size distribution parameter β are 1.0, 5.0, and 10.0. The multiple grain sizes are twenty discrete equally spaced sizes between 0.1 mm and 7.0 mm. In Figure 4-4(a), the extinction coefficients are plotted against the frequency. The extinction coefficients increase as the frequency increases, but the frequency dependence is 3.4, 3.6, and 4.0 when $\beta = 1.0, 5.0, \text{and } 10.0$ respectively. It is close to Rayleigh scattering model when $\beta = 10.0$. In Figure 4-4(b), the mean cosines are plotted against frequencies. The values of mean cosine are moderate and fall between 0.0 and 0.25.

4.3 COMPUTATION OF CORRELATION FUNCTION FROM PAIR DISTRIBUTION FUNCTIONS

In this section, the correlation function is derived in terms of pair functions. The relation can be expressed in the spatial domain and in the Fourier transform domain. The cases of multiple sizes and sticky particles are also studied. It is to be noted that that Torquato and Stell [58] and Veysoglu and Kong [59] also studied the relation between correlation function and pair function for single size non-sticky particles.

Let $\Theta(\bar{r})$ be the indicator function.

$$\Theta(\bar{r}) = \begin{cases} 1, \text{for } \bar{r} \text{ in ice} \\ 0, \text{for } \bar{r} \text{ in air} \end{cases} \quad (4\text{-}12)$$

The correlation function of $\Theta(\bar{r})$ is

$$C(|\bar{r}_1 - \bar{r}_2|) = E[\Theta(\bar{r}_1)\Theta(\bar{r}_2)] \quad (4\text{-}13)$$

where $E[.]$ denotes the statistical average. For an isotropic medium, the correlation function $is\ C(|\bar{r}_1 - \bar{r}_2|)$ which depends only on the distance $r = |\bar{r}_1 - \bar{r}_2|$. The covariance function is defined as

$$C_{OV}(|\bar{r}_1 - \bar{r}_2|) = E[\Theta(\bar{r}_1)\Theta(\bar{r}_2)] - E[\Theta(\bar{r}_1)]E[\Theta(\bar{r}_2)] \quad (4\text{-}14a)$$

$$C_{OV}(\bar{r}) = C(\bar{r}) - f_V^2 \quad (4\text{-}14b)$$

where f_V denotes the volume fraction of medium. Equation (4-14b) is used in an isotropic medium, where $\bar{r}$ degrades to scalar r. From Equation (4-12) and (4-13), the correlation function is

$$C(\bar{r}) = P(\Theta(0) = 1, \Theta(\bar{r}) = 1) \quad (4\text{-}15)$$

where $P(.)$ is the joint probability of $\Theta(0) = 1$ and $\Theta(\bar{r}) = 1$. Two types of particle configurations contribute to the correlation function in Equation (4-13): the first term P_S is for the configuration where the particle positions $\bar{r}_1$ and $\bar{r}_2$ are located in the same sphere; while the second term P_D is for the configuration that $\bar{r}_1$ and $\bar{r}_2$ reside in different spheres. In the first part, the sphere is assumed to be the i-th sphere in the medium, the correlation function is

$$P_S(\bar{r}) = \sum_{i=1}^{N} P(|\bar{r}_i| < a, |\bar{r}_i - \bar{r}| < a) \quad (4\text{-}16a)$$

$$P_S(\bar{r}) = N\frac{V(|\bar{r}_i| < a, |\bar{r}_i - \bar{r}| < a)}{V} \quad (4\text{-}16b)$$

$$P_S(\bar{r}) = \begin{cases} 0 & r > 2a \\ n_0\left(\frac{4\pi a^3}{3}\right)\left[1 - \frac{3}{4}\frac{r}{a} + \frac{1}{16}\left(\frac{r}{a}\right)^3\right] & 2a \geq r \end{cases} \quad \text{(4-16c)}$$

where $V(.)$ is the volume of $|\bar{r}_i| < a, |\bar{r}_i - \bar{r}| < a$, V is the whole volume of the scatterer, and a is the radius of the particle. In the second part, the correlation function is

$$P_D(\bar{r}) = \sum_{i=1}^{N}\sum_{j=1, j\neq i}^{N} P\left(|\bar{r}_i| < a, \left|\bar{r}_j - \bar{r}\right| < a\right) \quad \text{(4-17a)}$$

$$P_D(\bar{r}) = N^2 \iint\limits_{|\bar{r}_i|<a, \left|\bar{r}_j-\bar{r}\right|<a} d\bar{r}_i d\bar{r}_j P\left(\bar{r}_i, \bar{r}_j\right) \quad \text{(4-17b)}$$

$$P_D(\bar{r}) = n_0^2 \iint\limits_{|\bar{r}_i|<a, \left|\bar{r}_j-\bar{r}\right|<a} d\bar{r}_i d\bar{r}_j g\left(\left|\bar{r}_i - \bar{r}_j\right|\right) \quad \text{(4-17c)}$$

where $P\left(\bar{r}_i, \bar{r}_j\right)$ is the joint probability of particle 1 at $\bar{r}_1$ and particle 2 at $\bar{r}_2$, n_0 is the number density, and $g(.)$ is the pair distribution function [11] defined as $P\left(\bar{r}_i, \bar{r}_j\right) = \frac{g\left(|\bar{r}_i - \bar{r}_j|\right)}{V^2}$. The correlation function of the QCA model can be obtained from Equation (4-16) and (4-17):

$$C(\bar{r}) = P_S(\bar{r}) + P_D(\bar{r}) = n_0\left(\frac{4\pi a^3}{3}\right)\left[1 - \frac{3}{4}\frac{r}{a} + \frac{1}{16}\left(\frac{r}{a}\right)^3\right] + n_0^2 \iint\limits_{|\bar{r}_i|<a, \left|\bar{r}_j-\bar{r}\right|<a} d\bar{r}_i d\bar{r}_j g\left(\left|\bar{r}_i - \bar{r}_j\right|\right) \quad \text{(4-18)}$$

The integral in Equation (4-18) is six-fold, but can be reduced to four-fold due to uniformity in azimuthal ϕ_i and ϕ_j directions:

$$C(\bar{r}) = n_0\left(\frac{4\pi a^3}{3}\right)\left[1 - \frac{3}{4}\frac{r}{a} + \frac{1}{16}\left(\frac{r}{a}\right)^3\right] + (2\pi n_0)^2 \int_0^a dr_i r_i^2 \int_{-1}^1 d\mu_i \int_0^a dR R^2 \int_{-1}^1 d\mu\, g\left(\left|\bar{r}_i - \bar{r}_j\right|\right) \quad (4\text{-}19a)$$

$$\left|\bar{r}_i - \bar{r}_j\right| = \sqrt{R^2 + 2R\mu\sqrt{r_i^2(1-\mu_i^2) + (r - r_i\mu_i)^2} + [r_i^2(1-\mu_i^2) + (r - r_i\mu_i)^2]} \quad (4\text{-}19b)$$

where the argument in pair distribution function $g(.)$ is expanded from $\left|\bar{r}_i - \bar{r}_j\right|$ in spherical coordinates, with $\mu_i = \cos\theta_i$ and $\mu = \cos\Theta$. The brutal-force integration of the second additive term is time-consuming, especially when the radius of the sphere is large. Fourier transform is developed to numerically compute the correlation function. Define

$$I(\bar{r}', \bar{r}) = 1, (\text{If } |\bar{r}'| < a, |\bar{r}| < a) \quad (4\text{-}20)$$

Then the second part of correlation function in Equation (4-18) is

$$P_D(\bar{r}', \bar{r}) = n_0^2 \iint\limits_{|\bar{r}_i|<a, |\bar{r}_j - \bar{r}|<a} d\bar{r}_i d\bar{r}_j I\left(\bar{r}' - \bar{r}_i, \bar{r} - \bar{r}_j\right)\left[g\left(\bar{r}_i, \bar{r}_j\right) - 1\right] + n_0^2 \iint\limits_{|\bar{r}_i|<a, |\bar{r}_j - \bar{r}|<a} d\bar{r}_i d\bar{r}_j I\left(\bar{r}' - \bar{r}_i, \bar{r} - \bar{r}_j\right) \quad (4\text{-}21)$$

Note that the first term in Equation (4-21) is related to the total influence function $h(\bar{r}) = g(\bar{r}) - 1$ [11] and the pair distribution function $g(\bar{r})$:

$$P_D(\bar{r}', \bar{r}) = P_{dc}(\bar{r}', \bar{r}) + n_0^2\left(\frac{4\pi a^3}{3}\right)^2 \quad (4\text{-}22a)$$

$$P_{dc}(\bar{r}',\bar{r}) \triangleq n_0^2 \iint\limits_{|\bar{r}_i|<a,|\bar{r}_j-\bar{r}|<a} d\bar{r}_i d\bar{r}_j I(\bar{r}'-\bar{r}_i,\bar{r}-\bar{r}_j)h(\bar{r}_i,\bar{r}_j)$$	(4-22b)

The second term in Equation (4-22a) represents the offset of the correlation function. After removing this term, the covariance function will be obtained. Equation (4-22b) has a spatial convolution functional form. Define the spatial Fourier transforms as

$$P_{dc}(\bar{r}) = \int d\bar{p}\exp(i\bar{p}.\bar{r})\,P_{dc}(\bar{p})$$	(4-23a)
$$h(\bar{r}) = \int d\bar{p}\exp(i\bar{p}.\bar{r})\,H(\bar{p})$$	(4-23b)
$$I(\bar{r}',\bar{r}) = \int d\bar{p}\int d\bar{p}'\exp(i\bar{p}'.\bar{r}'-i\bar{p}.\bar{r})\,I(\bar{p}',\bar{p})$$	(4-23c)

Therefore the spatial convolution in Equation (4-22b) becomes spectral multiplication

$$P_{dc}(\bar{p}) = n_0^2 I(\bar{p},\bar{p})H(\bar{p})(2\pi)^6$$	(4-24)

Then according to Equation (4-23c)

$$I(\bar{p}',\bar{p}) = \frac{1}{(2\pi)^6}\int_{|\bar{r}'|<a} d\bar{r}'\int_{|\bar{r}|<a} d\bar{r}\exp(-i\bar{p}'.\bar{r}'+i\bar{p}.\bar{r})$$	(4-25a)
$$I(\bar{p}',\bar{p}) = \frac{1}{(2\pi)^6}Q(\bar{p})Q^*(\bar{p}')$$	(4-25b)
$$Q(\bar{p}) = \int_{|\bar{r}|<a} d\bar{r}\exp(i\bar{p}.\bar{r})$$	(4-25c)

Assuming isotropic medium, vector $\bar{p}$ reduces to p

$$P_{dc}(p) = n_0^2 Q^2(p) H(p) \quad \text{(4-26a)}$$

$$Q(p) = \frac{4\pi a^2}{p} j_1(pa) \quad \text{(4-26b)}$$

where $j_1(.)$ is the first order spherical Bessel function, and $H(p)$ is the Fourier transform of $h(r)$. After $P_{dc}(p)$ is computed, the inverse Fourier transform is applied to compute $P_{dc}(\bar{r})$.

$$P_{dc}(\bar{r}) = \int d\bar{p} \exp(i\bar{p}.\bar{r})\, P_{dc}(\bar{p}) = 4\pi \int_0^{+\infty} dp p^2 P_{dc}(p) \frac{\sin(pr)}{pr} \quad \text{(4-27a)}$$

$$P_{dc}(\bar{r}) = (4\pi)^3 n_0^2 a^4 \int_0^{+\infty} dp j_1^2(pa) \frac{\sin(pr)}{pr} \quad \text{(4-27b)}$$

Finally the correlation function is obtained as

$$C(\bar{r}) = n_0 \left(\frac{4\pi a^3}{3}\right)\left[1 - \frac{3}{4}\left(\frac{r}{a}\right) + \frac{1}{16}\left(\frac{r}{a}\right)^3\right] + n_0^2 \left(\frac{4\pi a^3}{3}\right)^2 + P_{dc}(\bar{r}) \quad \text{(4-28)}$$

The analytical expressions $H(p)$ of Percus-Yevick pair distribution functions can be found in [11]. The correlation function can be extended to multi-size case. Assume the multiple grain sizes are $a_1, a_2, \ldots a_M$ $(0 < a_1 < a_2 < \cdots < a_M)$, and M is the number of particle species, then Equation (4-16c) becomes

$$P_S^{(m)}(\bar{r}) = \begin{cases} 0 & r > 2a_M \\ \tilde{P}_M(\bar{r}) & 2a_M \geq r > 2a_{M-1} \\ \tilde{P}_M(\bar{r}) + \tilde{P}_{M-1}(\bar{r}) & 2a_{M-1} \geq r > 2a_{M-2} \\ \vdots & \vdots \\ \tilde{P}_M(\bar{r}) + \tilde{P}_{M-1}(\bar{r}) + \cdots + \tilde{P}_1(\bar{r}) & 2a_1 \geq r \geq 0 \end{cases} \quad \text{(4-29a)}$$

$$\tilde{P}_k(\bar{r}) \triangleq n_k \left(\frac{4\pi a_k^3}{3}\right)\left[1 - \frac{3}{4}\frac{r}{a_k} + \frac{1}{16}\left(\frac{r}{a_k}\right)^3\right], k = 1,2, \ldots, M \quad \text{(4-29b)}$$

where the subscript (m) stands for multi-size, $P_S^{(m)}(\bar{r})$ represents the probability of two points residing in the same particle. Then the probability of two points residing in different particles is

$$P_D^{(m)}(\bar{r}) = \sum_{k=1}^{M}\sum_{l=1}^{M} n_k n_l \iint\limits_{|\bar{r}_i|<a_k, |\bar{r}_j-\bar{r}|<a_l} d\bar{r}_i d\bar{r}_j g_{kl}\left(|\bar{r}_i - \bar{r}_j|\right) \quad (4\text{-}30a)$$

$$P_D^{(m)}(\bar{r}) = \sum_{k=1}^{M}\sum_{l=1}^{M} (2\pi n_k)(2\pi n_l)\int_0^{a_k} dr_i r_i^2 \int_{-1}^{1} d\mu_i \int_0^{a_l} dR R^2 \int_{-1}^{1} d\mu\, g_{kl}\left(|\bar{r}_i - \bar{r}_j|\right) \quad (4\text{-}30b)$$

$$|\bar{r}_i - \bar{r}_j| = \sqrt{R^2 + 2R\mu\sqrt{r_i^2(1-\mu_i^2) + (r - r_i\mu_i)^2} + [r_i^2(1-\mu_i^2) + (r - r_i\mu_i)^2]} \quad (4\text{-}30c)$$

Finally the correlation function of multi-size spheres is a sum as below

$$C^{(m)}(\bar{r}) = P_S^{(m)}(\bar{r}) + P_D^{(m)}(\bar{r}) \quad (4\text{-}31)$$

Then each four-fold space integral in the double sum can be computed using the Fourier transform. First the offset of the correlation function is extracted out

$$P_D^{(m),k,l}(\bar{r}', \bar{r}) = P_{dc}^{(m),k,l}(\bar{r}', \bar{r}) + n_k n_l \left(\frac{4\pi a_k^3}{3}\right)\left(\frac{4\pi a_l^3}{3}\right) \quad (4\text{-}32)$$

Then the Fourier transform of the first term in Equation (4-32) is

$$P_{dc}^{(m),k,l}(p) = n_k n_l Q_k(p) Q_l(p) H_{kl}(p) \quad (4\text{-}33a)$$

$$Q_k(p) = \frac{4\pi a_k^2}{p} j_1(p a_k) \quad (4\text{-}33b)$$

$$Q_l(p) = \frac{4\pi a_l^2}{p} j_1(pa_l) \quad (4\text{-}33c)$$

After inverse Fourier transform, the covariance function is

$$P_{dc}^{(m),k,l}(\vec{r}) = \int d\vec{p} \exp(i\vec{p}.\vec{r})\, P_{dc}^{(m),k,l}(\vec{p}) = 4\pi \int_0^{+\infty} dp p^2 P_{dc}^{(m),k,l}(p) \frac{\sin(pr)}{pr} \quad (4\text{-}34)$$

Finally the correlation function for multi-size spheres is obtained as

$$C^{(m)}(\vec{r}) = P_S^{(m)}(\vec{r}) + \sum_{k=1}^{M}\sum_{l=1}^{M}\left[P_{dc}^{(m),k,l}(\vec{r}) + n_k n_l \left(\frac{4\pi a_k^3}{3}\right)\left(\frac{4\pi a_l^3}{3}\right)\right] \quad (4\text{-}35)$$

4.3.1 QCA single-size and QCA sticky model

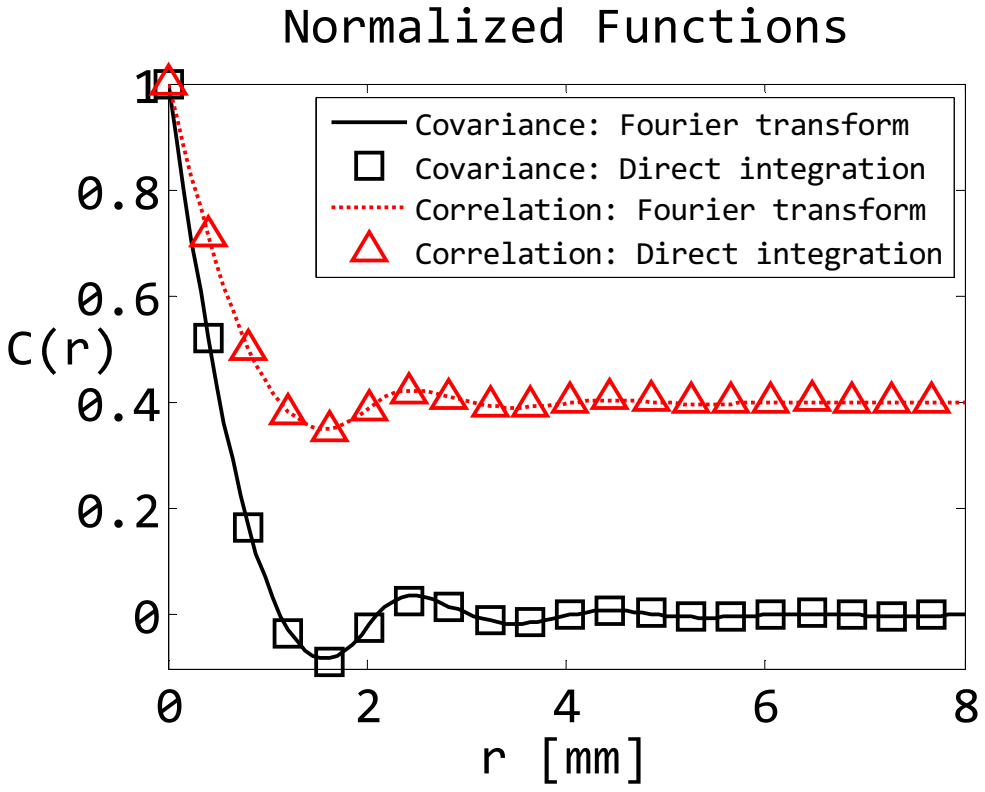

Figure 4-5 Normalized covariance and correlation functions using direct integration approach and Fourier transform approach.

Fraction volume = 40%; diameter = 2.0 mm; stickiness parameter = 1.0.

In Figure 4-5 the covariance and correlation functions of sticky particle computed using the direct space integral approach [59] and the Fourier transform approach are compared. The fractional volume is 40%, the diameter is 2.0 mm, and the stickiness is 1.0. The functions are plotted up to 4 times the diameter. The agreement of the two approaches validates the Fourier transform approach. However, to compute the covariance (correlation) function values of 1000 spatial points, the direct space integral approach takes longer than 1 hour CPU time, while the Fourier transform approach gives numerical results with much less CPU.

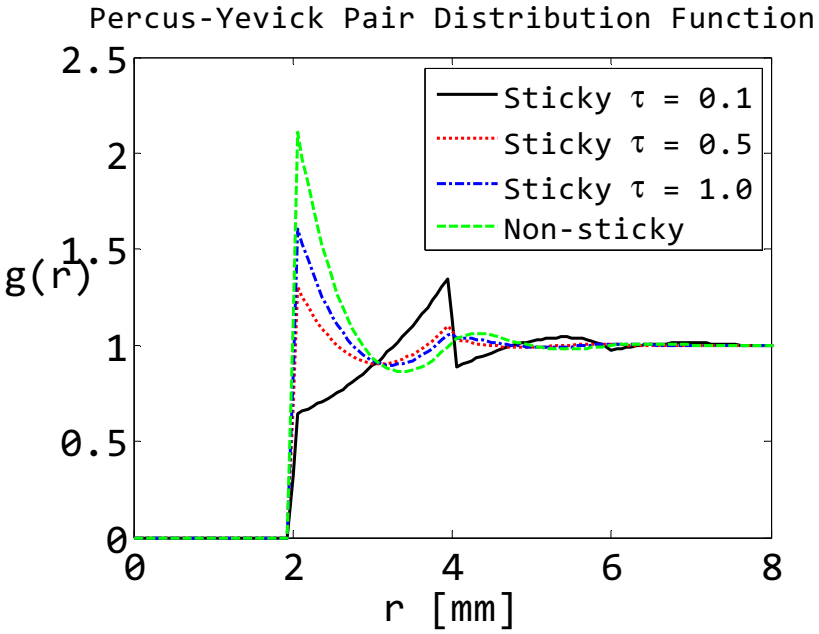

(a)

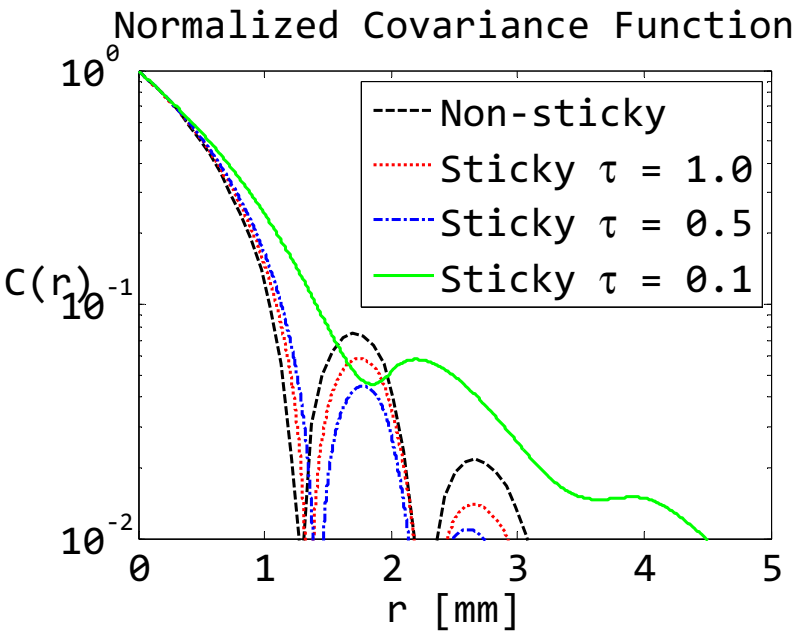

(b)

Figure 4-6 Percus-Yevick pair distribution functions and normalized covariance functions of non-sticky and sticky particle models.

Fraction volume = 30%; diameter = 2.0 mm.

(a) Pair distribution function (b) covariance function

Figure 4-6 illustrates the pair distribution functions and the covariance functions of non-sticky and sticky particles with different stickiness. The diameter of particles is 2.0 mm and the fractional volume is 30%. In Figure 4-6(a), the Percus-Yevick pair distribution functions are plotted up to 4 times the diameter where they reach the steady value 1.0. At distances smaller than the diameter, the pair distribution functions are zero, which indicates that the particles are non-penetrable. As shown in Figure 4-6(b), the correlation function of sticky particle becomes closer to that of the non-sticky particle model as the parameter τ increases. The oscillation pattern observed in the correlation function is because of the geometric structure being based on

impenetrable spheres. When τ decreases to 0.1, the oscillation pattern is largely reduced (the solid line), since smaller τ leads to stronger aggregation effect, and thus there exists effectively large grains in the medium.

4.3.2 QCA multi-size model

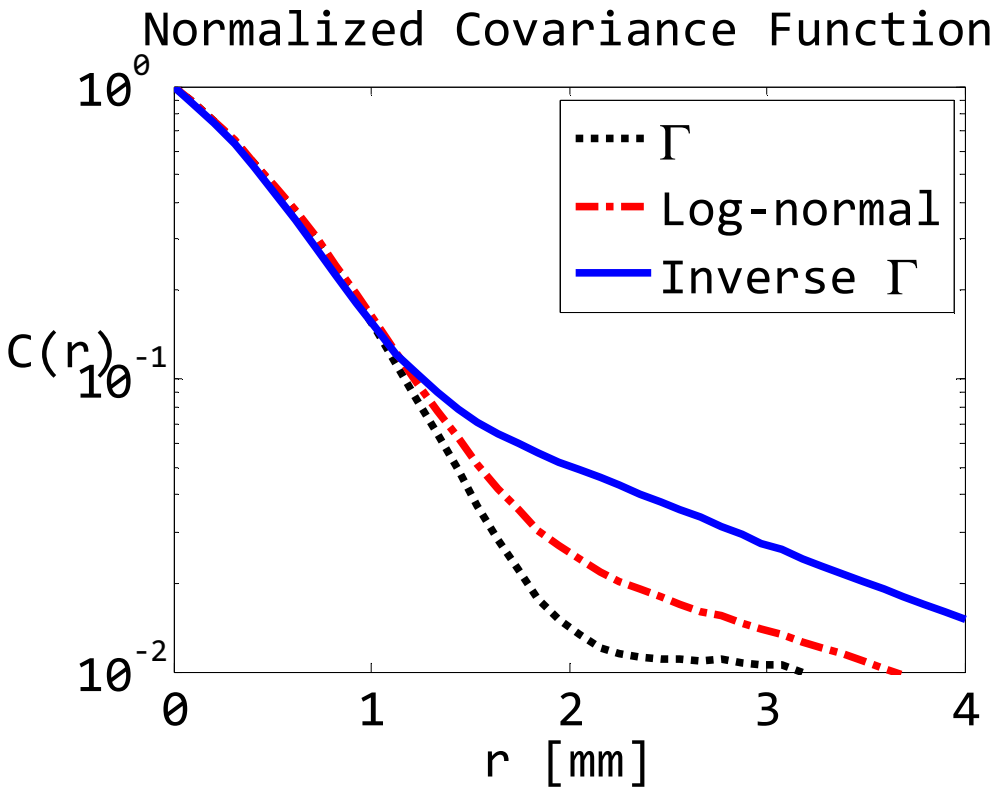

Figure 4-7 Covariance functions of three types of size distribution: Gamma, log-normal, inverse-Gamma.

Figure 4-7 illustrates the corresponding covariance functions for the respective three size distributions: Gamma distribution $p_G(d)$, log-normal distribution $p_L(d)$, and inverse-Gamma distribution $p_I(d)$. Twenty equal-spaced grain sizes, from 0.1 mm to 7.0 mm, are used to approximate the continuous size distribution. The pair distribution functions for multiple-size non-sticky particles can be found in [11]. The correlation functions are then computed from the

corresponding pair distribution functions. The mean diameter $\langle d \rangle$ is fixed at 1.0 mm for all three size distributions. The parameters are: $\beta = 1.5$, for Gamma distribution; $\sigma = 0.5$ for log-normal distribution; and $\beta = 6.0$ for inverse-Gamma distribution. These size distribution parameters are adjusted so that the three covariance functions coincide at small distances (< 1.0 mm). The values of covariance functions are plotted to 10^{-2}. It is noticeable that the Gamma distribution has a lower tail than the other two types, and the inverse-Gamma distribution has the highest tail. Thus the inverse-Gamma size distribution would be a good model to characterize large aggregation in snow.

4.4 COMPARISON OF COVARIANCE FUNCTIONS WITH BICONTINUOUS MODEL

4.4.1 Bicontinuous correlation function

The correlation function of bicontinuous model is given by [13] [34].

$$C(\bar{r}) = f_V^2 + \sum_{m=1}^{+\infty} C_m(\alpha)[C_S(r)]^m \tag{4-36}$$

where $C_m(\alpha) = \frac{\exp(-2\alpha^2) H_{m-1}^2(\alpha)}{\pi m! 2^m}$ and $H_{m-1}(.)$ is the $m-1$ order Hermite polynomial. In Equation (4-36), $C_S(r)$ is the correlation function of $S(r)$

$$C_S(r) = \int_0^{+\infty} d\zeta p(\zeta) \frac{\sin(\zeta r)}{\zeta r} \tag{4-37}$$

The analytical expression of $C_S(r)$ for Gamma distribution was in [13]. For a general distribution, $C_S(r)$ can be obtained by numerical integration. The Gamma distribution of wavenumber was considered in [13] [49], where $\langle \zeta \rangle$ is the mean wavenumber and b is the shape parameter. The mean wavenumber $\langle \zeta \rangle$ is inversely proportional to the mean grain size, and the

parameter b is related to the clustering effect; as b decreases there will be more effectively large ice grain aggregates in the medium. Log-normal and inverse-Gamma distributions for the wavenumber are also considered. In $p_G(\zeta)$, $p_L(\zeta)$, and $p_I(\zeta)$, there are two parameters. One parameter is related to the mean grain size, while the other is related to the size distribution.

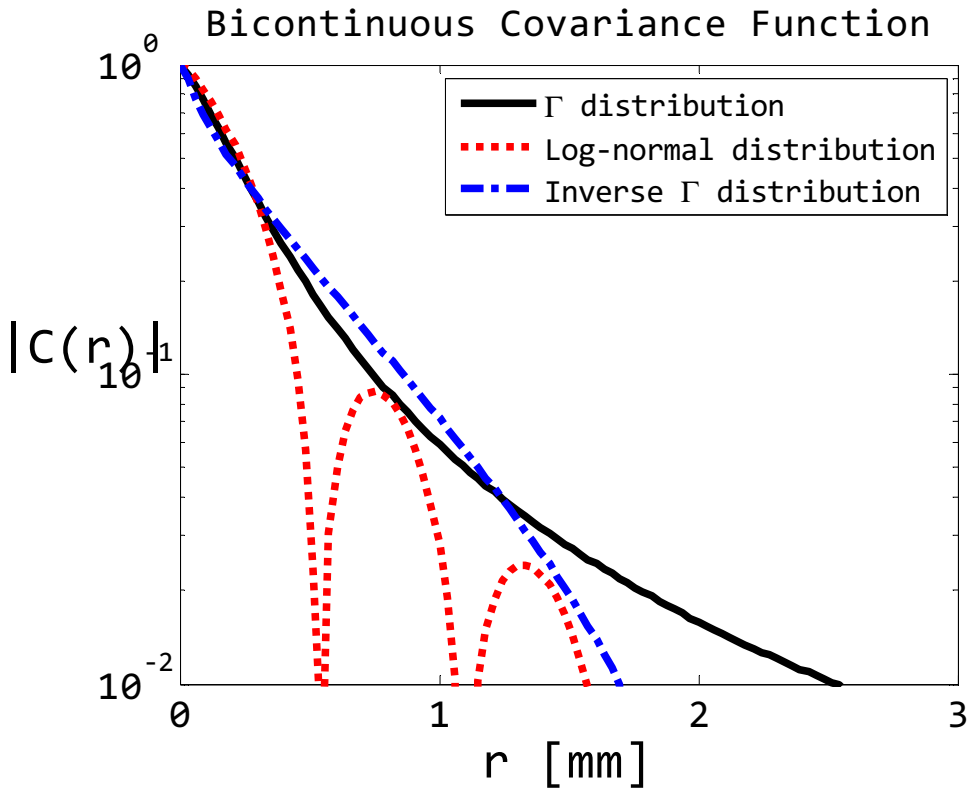

Figure 4-8 Normalized covariance functions of bicontinuous model, using three types of wavenumber distribution.

In Figure 4-8 the correlation functions for the bicontinuous models with three types of distribution functions are shown. The fractional volume is 30%. The model parameters are adjusted such that the three distribution functions coincide at small distance r: $\langle\zeta\rangle = 6000\, m^{-1}$ and $b = 1.0$ for the Gamma distribution; $\langle\zeta\rangle = 6000\, m^{-1}$ and $\sigma = 0.2$ for the log-normal distribution; and $\langle\zeta\rangle = 3800\, m^{-1}$ and $b = 0.1$ for the inverse-Gamma distribution. It is seen that

that the Gamma distribution has a higher tail, which is contributed by small ζ in $p_G(\zeta)$, or equivalently the large aggregation in the medium. The log-normal distribution has the smallest tail, because the wavenumber distribution is relatively narrow. The correlation length is defined as the value of r where the correlation function $C(r)$ is equal to e^{-1}. As shown in Figure 4-8, the three curves intersect $r = 0.3$ mm which is approximately the correlation length of medium. The correlation length is insufficient to describe the random medium as the tail of the correlation function contributes significantly to scattering because scattering increases with grain sizes.

It is worth noting that the wavenumber distributions defined in Equation (4-10) are the inverse to the size distributions defined in Equation (4-5). For example, Gamma and inverse-Gamma distributions are inverses to each other, and log-normal distribution is the inverse of itself. Thus the covariance functions of inverse-Gamma size distribution and Gamma wavenumber distribution both give high tails. Both can be used to describe ice grain aggregation in snow.

4.4.2 Comparison among QCA multi-size, QCA sticky, and bicontinuous models

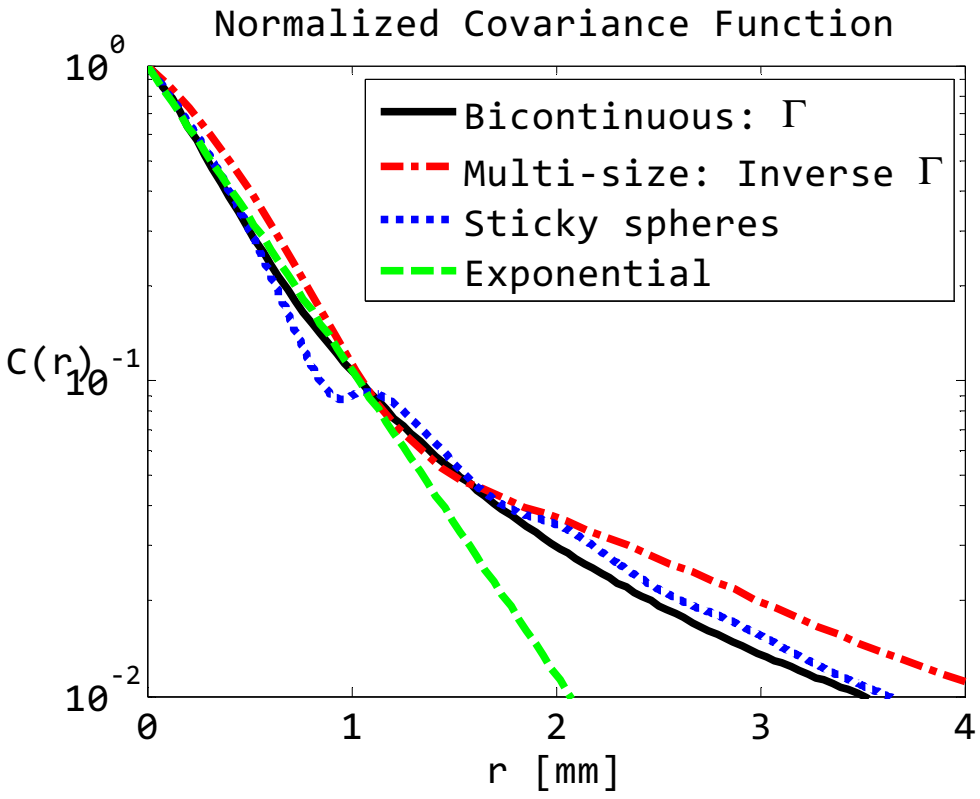

Figure 4-9 Covariance functions of QCA multi-size, QCA sticky, and bicontinuous models

In Figure 4-9, the QCA multi-size, QCA sticky, and bicontinuous covariance functions are compared with exponential covariance function. The functions are plotted in log-scale, so exponential function is a straight line. The parameters are: QCA multi-size: $\langle d \rangle = 1.0$ mm, $\beta = 7.0$; QCA sticky $d = 1.0$ mm, $\tau = 0.1$; bicontinuous: $\langle \zeta \rangle = 4000$ m^{-1}, $b = 1.0$; fraction volume = 30%. It is shown that all functions have about the same correlation length, as they coincide at distances smaller than 1.0 mm. However, exponential function decays linearly in log-scale. Other three covariance functions have tails at distances larger than 2.0 mm, which indicates large grain aggregation in the medium. Particularly, the multi-size covariance function matches to bicontinuous model asymptotically in the tail.

4.5 PARAMETER EXTRACTION FROM GROUND MEASUREMENT

In the present ground measurements, there are two physical quantities: measured grain size, and the correlation length. Relations have been established empirically between grain size and correlation length [21] [26]. These have been used to compute scattering for the MEMLS model and the HUT model. However, to use the QCA sticky model, the QCA multiple-size model, and the bicontinuous model, more parameters are needed. In this section, it will be described how measurements can be used to determine input parameters for these three models.

QCA multi-size spheres model parameter is a grain size distribution. Therefore the measured multiple grain sizes can be empirically fit with a size distribution. Then the Percus-Yevick pair distribution functions are used for computation in the QCA multi-size model.

In QCA sticky model, there are two model parameters: mean grain size and stickiness parameter. The mean grain size can be measured. The other model parameter is the stickiness parameter, which can be extracted from the covariance function. One can use the digitized picture of snow to extract the covariance function accurately to 0.01. By comparing the measured covariance function with that of covariance function of sticky particle, the stickiness parameter can be extracted.

When extracting the correlation function from one single digitized snow picture, the spatially stationary property of the snow medium is assumed, which means the two point correlation function is determined by the difference between the two points

$$C(\bar{r}_1, \bar{r}_2) = C(\bar{r}_1 - \bar{r}_2) = C(\bar{r}) \quad (4\text{-}38)$$

Then the correlation function extracted from one snow image is

$$C(\bar{r}) = \sum_{\bar{r}' \text{ in the image}} \Theta(\bar{r}')\Theta(\bar{r}' + \bar{r}) \quad (4\text{-}39)$$

where $\Theta(.)$ is the indicator function.

The bicontinuous model has two parameters, the mean wavenumber $\langle\zeta\rangle$ and the factor b that determines the aggregation and size distribution. Based on the above discussions, it is proposed to extract the bicontinuous model parameters from ground measurements using the following two approaches:

(1) Measurements of multiple grain sizes: From the measured multiple grain sizes, they are first fit into a grain size distributions, and then the Percus-Yevick pair distributions functions can be computed. Using the pair distribution functions, the covariance (correlation) function can be computed. By comparing the covariance (correlation) function with that of the bicontinuous model, the bicontinuous model parameters can be extracted.

(2) Digitized picture of snow microstructure: Using digitized pictures of snow, the covariance (correlation) functions of natural snow can be computed. This is required to be computed with high accuracy such as up to 0.01 so that the tail of the covariance (correlation) function can be ascertained. By comparing the computed covariance (correlation) function with that of the bicontinuous model, the two bicontinuous parameters can be determined.

4.6 CONCLUSION

In this chapter, the scattering properties of QCA multi-size model, the QCA sticky particle model and bicontinuous model are compared. Co-polarization phase matrices of all three models show moderate forward scattering effect, with mean cosine between 0.1 and 0.4. All three models give a frequency dependence weaker than 4.0. Then medium characterization is also studied. For

QCA, the covariance function is derived from the Percus-Yevick pair distribution functions, which is used for both multi-size and single-size sticky cases. The covariance functions are also derived for bicontinuous model. The covariance function is compared with those of the QCA multi-size and QCA sticky models. It is shown that all models have tails in the covariance functions that are distinctly different from the exponential function. The tails contribute strongly to scattering. Measurements equired to determine the model parameters are also discussed. In particular, measurements of grain size distribution and measurements of covariance function with accuracy up to 0.01 are proposed.

BIBLIOGRAPHY

[1] Board, Space Studies. *Earth science and applications from space: National imperatives for the next decade and beyond*. National Academies Press, 2007.

[2] H. Rott, D. W. Cline, C. Duguay, R. Essery, P. Etchevers, I. Hajnsek, M. Kern, G. Macelloni, E. Malnes, J. Pulliainen, and S. H. Yueh, "CoReH2O, a dual frequency radar mission for snow and ice observations," *Geoscience and Remote Sensing Symposium (IGARSS), 2012 IEEE International* , vol., no., pp.5550,5553, 22-27 July 2012

[3] A. Coccia, C. Trampuz, E. Imbembo, and A. Meta, "First Results of SnowSAR, the new X- and Ku-Band Polarimetric Airborne SAR Sensor supporting the CoReH2O Mission." *Workshop on Advanced RF Sensors and Remote Sensing Instruments, ESA/ESTEC, Noordwijk, NL*. 2011.

[4] R. E. Kelly, A. T. Chang, L. Tsang, and J. L. Foster. "A prototype AMSR-E global snow area and snow depth algorithm." *Geoscience and Remote Sensing, IEEE Transactions on* 41, no. 2 (2003): 230-242.

[5] S. Pettinato, E. Santi, M. Brogioni, S. Paloscia, P. Pampaloni, E. Palchetti, J. Shi, and C. Xiong. "The potential of Cosmo-Skymed SAR images in mapping snow cover and snow water equivalent." *In Geoscience and Remote Sensing Symposium (IGARSS), 2011 IEEE International*, pp. 2733-2736. IEEE, 2011.

[6] H. Rott, S. H. Yueh, D. W. Cline, C. Duguay, R. Essery, C. Haas, F. Heliere, M. Kern, G. Macelloni, E. Malnes, T. Nagler, J. Pulliainen, H. Rebhan, and A. Thompson, "Cold Regions Hydrology High-Resolution Observatory for Snow and Cold Land Processes," *Proceedings of the IEEE* , vol.98, no.5, pp.752,765, May 2010

[7] J. Cohen, J. Lemmetyinen, T. Smolander, and J. Pulliainen, Processing of Airborne SnowSAR data to level 2 product, *ESA ESTEC Contract No. 22830/09/NL/JC*, July 2012.

[8] J. Lemmetyinen, A. Kontu, J. Pulliainen, A. Wiesmann, C. Werner, T. Nagler, H. Rott and M. Heidinger, Technical Assistance for the Deployment of an X- to Ku-Band Scatterometer during the NoSREx II Experiment, Final Report, *ESA ESTEC Contract No. 22671/09/NL/JA*, Dec. 2011.

[9] S. Chandrasekhar, *Radiative transfer*. Courier Dover Publications, 1960.

[10] A. Ishimaru, *Wave propagation and scattering in random media*. Vol. 2. New York: Academic press, 1978.

[11] L. Tsang, J.A. Kong, K. H. Ding, and C. O. Ao. *Scattering of electromagnetic waves, numerical simulations*. Vol. 2. Wiley-Interscience, 2001.

[12] L. Tsang, J.A. Kong. *Scattering of electromagnetic waves: Advanced Topics*. Vol. 3. Wiley-Interscience, 2001.

[13] K.-H. Ding; X. Xu; L. Tsang, "Electromagnetic Scattering by Bicontinuous Random Microstructures With Discrete Permittivities," *Geoscience and Remote Sensing, IEEE Transactions on* , vol.48, no.8, pp.3139,3151, Aug. 2010.

[14] L. Tsang, C.-T. Chen, A. T. C. Chang, J. Guo, and K.-H. Ding, “Dense media radiative transfer theory based on quasicrystalline approximation with applications to passive microwave remote sensing of snow,” *Radio Sci*, vol. 35, no. 3, pp. 731-749, 2000.

[15] L. Tsang, J. Pan, D. Liang, Z. Li, D. W. Cline, and Y. Tan, “Modeling active microwave remote sensing of snow using dense media radiative transfer (DMRT) theory with

multiple-scattering effects," *IEEE Trans. Geosci. Remote Sens.*, vol. 45, no. 4, pp. 990-1004, Apr. 2007.

[16] K. K. Tse, L. Tsang, C. H. Chan, K. H. Ding, and K. W. Leung, "Multiple scattering of waves by dense random distributions of sticky particles for applications in microwave scattering by terrestrial snow," *Radio Science*, vol. 42, RS5001, 2007.

[17] L. Tsang and J. A. Kong, "Scattering of electromagnetic waves from random media with strong permittivity fluctuations," *Radio Science*, 16(3), 303-320, May-June 1981.

[18] L. Tsang, J. A. Kong, and R. T. Shin. "*Theory of microwave remote sensing*." (1985).

[19] F. Vallese, & J. A. Kong, "Correlation function studies for snow and ice". *Journal of Applied Physics*, 52(8), 4921-4925. 1981.

[20] A. Stogryn, "Correlation functions for random granular media in strong fluctuation theory." *Geoscience and Remote Sensing, IEEE Transactions on* 2 (1984): 150-154.

[21] C. Mätzler, "Autocorrelation functions of granular media with free arrangement of spheres, spherical shells or ellipsoids." *Journal of Applied Physics* 81.3 (1997): 1509-1517.

[22] C. Mätzler, "Improved Born approximation for scattering of radiation in a granular medium." *Journal of Applied Physics* 83.11 (1998): 6111-6117.

[23] A. Wiesmann, C. Mätzler, and T. Weise, "Radiometric and structural measurements of snow samples," *Radio Science*, vol. 33, no. 2, pp. 273-289, 1998.

[24] C. Mätzler, and A. Wiesmann. "Extension of the microwave emission model of layered snowpacks to coarse-grained snow." *Remote Sensing of Environment* 70.3 (1999): 317-325.

[25] A. Wiesmann, and C. Mätzler. "Microwave emission model of layered snowpacks." *Remote Sensing of Environment* 70.3 (1999): 307-316.

[26] C. Mätzler, “Relation between grain-size and correlation length of snow,” *J. Glaciol*., vol. 48, no. 162, pp. 461-466, 2002.

[27] X. Phan, L. F.-Famil, M. Gay, Y. Durand, M. Dumont, and G. D'Urso. "Multilayer snowpack backscattering model and assimilation of TerraSAR-X satellite data." *Geoscience and Remote Sensing Symposium (IGARSS), 2012 IEEE International*, pp. 5856-5859. IEEE, 2012.

[28] J. T. Pulliainen, J. Grandell, and M. T. Hallikainen. "HUT snow emission model and its applicability to snow water equivalent retrieval." *Geoscience and Remote Sensing, IEEE Transactions on* 37.3 (1999): 1378-1390.

[29] J. Lemmetyinen, J. Pulliainen, A. Rees, A. Kontu, Y. Qiu, and C. Derksen, “Multiple-layer adaptation of HUT snow emission model: comparison with experimental data,” *IEEE Trans. Geosci. Remote Sens*., vol. 48, no. 7, pp. 2781-2794, July 2010.

[30] L. Tsang; K. H. Ding; S. Huang; and X. Xu, "Electromagnetic Computation in Scattering of Electromagnetic Waves by Random Rough Surface and Dense Media in Microwave Remote Sensing of Land Surfaces," *Proceedings of the IEEE* , vol.101, no.2, pp.255,279, Feb. 2013

[31] S. Huang; L. Tsang; E. G. Njoku, and K. S. Chan, "Backscattering Coefficients, Coherent Reflectivities, and Emissivities of Randomly Rough Soil Surfaces at L-Band for SMAP Applications Based on Numerical Solutions of Maxwell Equations in Three-Dimensional Simulations," *Geoscience and Remote Sensing, IEEE Transactions on* , vol.48, no.6, pp.2557,2568, June 2010

[32] L. Tsang, J.A. Kong, and K. H. Ding, *Scattering of electromagnetic waves, theories and applications*. Vol. 1. Wiley-Interscience, 2000.

[33] X. Xu, L. Tsang, S. Yueh,, "Electromagnetic Models of Co/Cross-polarization of Bicontinuous/DMRT in Radar Remote Sensing of Terrestrial Snow at X- and Ku-band for CoReH2O and SCLP Applications," *Selected Topics in Applied Earth Observations and Remote Sensing, IEEE Journal of* , vol.5, no.3, pp.1024-1032, June 2012

[34] N. F. Berk, Scattering properties of the leveled-wave model of random morphologies. *Physical Review A*, 44(8), 5069. 1991.

[35] V. I. Tatarski, *Wave propagation in a turbulent medium*. New York: McGraw-Hill. 1961.

[36] F. Domine, A. Cabanes, A. Taillandier, and L. Legagneux, "Specific surface area of snow samples determined by CH4 adsorption at 77 K and estimated by optical microscopy and scanning electron microscopy," *Environmental Science and Technology*, vol. 35, no. 4, pp. 771-780, Feb. 2001.

[37] M. Kerbrat, B. Pinzer, T. Huthwelker, H. W. Gäggeler, M. Ammann, & M. Schneebeli, "Measuring the specific surface area of snow with X-ray tomography and gas adsorption: comparison and implications for surface smoothness". *Atmospheric Chemistry and Physics*, *8*(5), 1261-1275. 2008.

[38] J. Gallet, F. Domine, C. Zender, and G. Picard, "Measurement of the specific surface area of snow using infrared reflectance in an integrating sphere at 1310 and 1550 nm," *The Cryosphere*, vol. 3, pp. 167-182, Aug. 2009.

[39] L. Arnaud, G. Picard, N. Champollion, F. Domine, J.-C. Gallet, E. Lefebvre, M. Fily and J.M. Barnola, “Measurement of vertical profiles of snow specific surface area with a 1 cm resolution using infrared reflectance: Instrument description and validation,” *Journal of Glaciology*, vol. 57, no. 201, pp. 17-29, Feb. 2011.

[40] W. Chang, L. Tsang, J. Lemmetyinen, X. Xu, and S. Yueh. “Bicontinuous/DMRT Model Applied To Active and Passive Microwave Remote Sensing of Terrestrial Snow.” Submitted to *Proceedings of IEEE 13th Specialist Meeting on Microwave Radiometry and Remote Sensing of the Environment (MicroRad),* Pasadena, USA, 2014

[41] C. Fierz, R. L. Armstrong, Y. Durand, P. Etchevers, E. Greene, D. M. McClung, K. Nishimura, P. K. Satyawali, and S. A. Sokratov, “The international classification for seasonal snow on the ground,” *IHP-VII Technical Documents in Hydrology No 83, IACS Contribution No 1, UNESCO-IHP*, Paris, 2009.

[42] X. Xu, D. Liang, L. Tsang, K. M. Andreadis, E. G. Josberger, D. P. Lettenmaier, D. W. Cline, and S. Yueh, “Active remote sensing of snow using NMM3D/DMRT and comparison with CLPX II airborne data,” *IEEE J. Sel. Topics Appl. Earth Observ. Remote Sens*., vol. 3, pp. 689–697, 2010.

[43] M. T. Hallikainen, F. T. Ulaby and T. E. Deventer, “Extinction behavior of dry snow in the 18 to 90 GHz range,” *IEEE Trans. Geosci. Remote Sens.*, vol.25, no.6, pp. 737-745, 1987

[44] G. Picard, L. Brucker, A. Roy, F. Dupont, M. Fily, A. Royer and C. Harlow, “Simulation of the microwave emission of multi-layered snowpacks using the Dense Media Radiative transfer theory: the DMRT-ML model,” *Geosci. Model Dev.*, 6: 1061-1078, 2013.

[45] H. Rott, T. Nagler, M. Heidinger, F. Müller, G. Macelloni, F. Montomoli, G. Fontanelli, U. Cortezi, M. Gai, R. Liguri, R. Scheiber, I. Hajnsek, D. Flach, J. Pulliainen, A. Arslan, E. Malnes, T. Tollefsen, K. J. Grottum, P. Etchevers and Y. Durand, “Development of Snow Retrieval Algorithms for CoReH$_2$O,” Final Report. ESA ESTEC Contract No. 22830/09/NL/JC.

[46] F. T. Ulaby, W. H. Stiles and M. Abdelrazik, “Snow cover influence on backscattering from terrain,” *IEEE Trans. Geos. Rem. Sens.*, 22(2): 126-133, 1984.

[47] L. Tsang, C. E. Mandt and K. H. Ding, “Monte Carlo simulations of the extinction rate of dense media with randomly distributed dielectric spheres based on solution of Maxwell’s equations,” Optics Letters, vol. 17, no. 5, pp. 314-316 , March 1992.

[48] D. Liang, X. Xu, L. Tsang, K. M. Andreadis and E. G. Josberger, “The effects of layers in dry snow on its passive microwave emissions using dense media radiative transfer theory based on the quasicrystalline approximation (QCA/DMRT),” *IEEE Trans. Geos. Rem. Sens.*, vol. 46, no. 11, pp. 3663-3671, Nov. 2008.

[49] W. Chang, S. Tan, J. Lemmetyinen, L. Tsang, X. Xu, and S. Yueh. "Dense Media Radiative Transfer Applied to SnowScat and SnowSAR," *Selected Topics in Applied Earth Observations and Remote Sensing, IEEE Journal of* , vol. pp., no.99, pp.1, 2015

[50] L. Tsang and A. Ishimaru, “Backscattering enhancement of random discrete scatterers,” *J. Opt. Soc. Am. A*, vol. 1, no. 8, pp. 836-1338, Aug. 1984.

[51] L. Tsang and A. Ishimaru, “Theory of backscattering enhancement of random discrete isotropic scatterers based on the summation of all ladder and cyclical terms,” *J. Opt. Soc. Am. A*, vol. 2, no. 8, pp. 1331-1338, Aug. 1985.

[52] Y. Kuga and A. Ishimaru, “Retroreflectance from a dense distribution of spherical particles,” *J. Opt. Soc. Am. A*, vol. 1, no. 8, pp. 831-835, Aug. 1984.

[53] Y. Kuga, L. Tsang and A. Ishimaru, “Depolarization effects of the enhanced retroreflectance from a dense distribution of spherical particles,” *J. Opt. Soc. Am. A*, vol. 2, no. 4, pp. 616-618, Apr. 1985.

[54] R. H. Lang and J. S. Sidhu, “Electromagnetic backscattering from a layer of vegetation: a discrete approach,” *IEEE Trans. Geo. Remote Sensing*, vol. GE-21, no. 1, pp. 62-71, Jan. 1983.

[55] J. Lemmetyinen, A. Kontu, K. Rautiainen, J. Vehviläinen, J. Pulliainen, T. Nagler, F. Müller, M. Heidinger, R. Sandner, H. Rott and A. Wiesmann, Technical Note NoSRex Consolidated Datasets, ESA ESTEC Contract No. 22671/09/NL/JA, Nov. 2013.

[56] S. Huang, L. Tsang, “Electromagnetic Scattering of Randomly Rough Soil Surfaces Based on Numerical Solutions of Maxwell Solutions of Maxwell Equations in Three-Dimensional Simulations Using a Hybrid UV/PBTG/SMCG Method,” *Geoscience and Remote Sensing, IEEE Transactions on*, vol. 50, no. 10, pp. 4025-4035, Oct. 2012

[57] L. M. Zurk, L. Tsang; J. Shi; and R. E. Davis, "Electromagnetic scattering calculated from pair distribution functions retrieved from planar snow sections," *Geoscience and Remote Sensing, IEEE Transactions on* , vol.35, no.6, pp.1419,1428, Nov 1997

[58] S. Torquato and G. Stell, "Microstructure of two-phase random media. V. The n-point matrix probability functions for impenetrable spheres." *The Journal of chemical physics* 82.2 (1985): 980-987.

[59] M. E. Veysoglu, and J. A. Kong. "Multi-scale correlation functions." *Progress In Electromagnetics Research* 14 (1996): 279-315.

APPENDIX

Consider two points $\bar{r}_1$ and $\bar{r}_2$, then the correlation function is the probability that both points are inside ice particles

$C(\overline{r}_2,\overline{r}_1) = E\big(\Theta(\overline{r}_2)\Theta(\overline{r}_1)\big)$	(A1a)
$C(\overline{r}_2,\overline{r}_1) = 1\times 1\times P(\Theta(\overline{r}_2)=1,\Theta(\overline{r}_1)=1) + 1\times 0\times P(\Theta(\overline{r}_2)=1,\Theta(\overline{r}_1)=0) + 0 \times 1\times P(\Theta(\overline{r}_2)=0,\Theta(\overline{r}_1)=1) + 0\times 0\times P(\Theta(\overline{r}_2)=0,\Theta(\overline{r}_1)=0)$	(A1b)
$C(\overline{r}_2,\overline{r}_1) = P(\Theta(\overline{r}_2)=1,\Theta(\overline{r}_1)=1)$	(A1c)

There are two possibilities: (1) the probability that both $\bar{r}_1$ and $\bar{r}_2$ are in the same particle P_S; (2) $\bar{r}_1$ and $\bar{r}_2$ are in different particles P_D. Then

$C(\overline{r}_2,\overline{r}_1) = P_S(\Theta(\overline{r}_2)=1,\Theta(\overline{r}_1)=1) + P_D(\Theta(\overline{r}_2)=1,\Theta(\overline{r}_1)=1)$	(A2)

Because of spherical symmetry

$C(\overline{r}_2,\overline{r}_1) = C(\lvert\overline{r}_2-\overline{r}_1\rvert)$	(A3)

Let $r = |\overline{r}_2 - \overline{r}_1|$. Without loss of generality, the point $\overline{r}_1$ is set at the origin and the point $\overline{r}_2$ is set at the positive z axis. Let $\overline{r}_2 = \bar{r} = (0,0,r) = (0,0,z)$. In random medium, let there be N particles in a box of volume V. Let i be the i-th particle, $i = 1,2,\dots,N$. $p(\bar{r}_i)$ is the probability density function of particle to be centered at $\bar{r}_i$, then

$p(\bar{r}_i) = \dfrac{1}{V}$	(A4)

Note that $N \gg 1$, then $n_0 = \frac{N}{V}$ is the number of particles per unit volume.

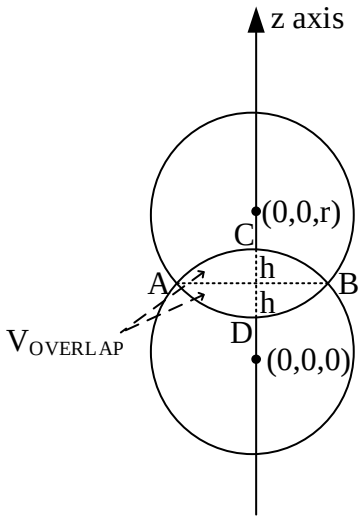

Figure A1. Particle positions 0 and $\bar{r}$ are located in the same sphere

Then

$$P_S = \sum_{i=1}^{N} P_i \quad \text{(A5)}$$

where P_i is the probability that both points are inside particle i. Since the particles are identical

$$P_S = NP_i \quad \text{(A6)}$$

Therefore

$$P_i = P(|\overline{r}_i| < a, |\overline{r}_i - \overline{r}| < a) \quad \text{(A7a)}$$

$$P_i = \int_{|\overline{r}_i|<a,|\overline{r}_i-\overline{r}|<a} p(\overline{r}_i) d\overline{r}_i \quad \text{(A7b)}$$

$$P_i = \frac{1}{V} \int_{|\overline{r}_i|<a,|\overline{r}_i-\overline{r}|<a} d\,\bar{r}_i \quad \text{(A7c)}$$

$$P_i = \frac{V_{overlap}}{V} \quad \text{(A7d)}$$

where

$$V_{overlap} = \int_{|\bar{r}_i|<a, |\bar{r}_i-\bar{r}|<a} d\,\bar{r}_i \quad \text{(A8)}$$

$V_{overlap}$ is the overlap volume of a sphere centered at the origin and a sphere centered at $\bar{r}$. Therefore

$$P_S = NP_i = N\frac{V_{overlap}}{V} = n_0 V_{overlap} \quad \text{(A9)}$$

According to Figure A1, $V_{overlap}$ is the sum of two identical spherical caps ABC and ABD, so it can be obtained by using the formula of the spherical cap V_{cap}

$$V_{cap} = \frac{\pi h^2}{3}(3a - h) \quad \text{(A10a)}$$

where h is the height of the spherical cap, and a is the radius. From Figure A1, for two intersecting spheres of identical radii a and separation distance r between the two centers, the height is

$$h = a - \frac{r}{2} \quad \text{(A10b)}$$

So $V_{overlap}$ is twice of V_{cap}

$$V_{overlap} = 2\frac{\pi h^2}{3}(3a - h) \quad \text{(A11)}$$

Then it can be simplified to

$$V_{overlap} = \begin{cases} 0 & r > 2a \\ \left(\frac{4\pi a^3}{3}\right)\left[1 - \frac{3}{4}\frac{r}{a} + \frac{1}{16}\left(\frac{r}{a}\right)^3\right] & 0 \le r \le 2a \end{cases} \quad \text{(A12a)}$$

$$P_S = \begin{cases} 0 & r > 2a \\ n_0\left(\frac{4\pi a^3}{3}\right)\left[1 - \frac{3}{4}\frac{r}{a} + \frac{1}{16}\left(\frac{r}{a}\right)^3\right] & 0 \le r \le 2a \end{cases} \quad \text{(A12b)}$$

To calculate P_D, pair distribution function $g(\bar{r}_j - \bar{r}_i)$ will be used. Let $p(\bar{r}_i, \bar{r}_j)$ be the joint probability density function of particle i centered at $\bar{r}_i$ and particle j centered at $\bar{r}_j$

$$p(\bar{r}_i, \bar{r}_j) = p(\bar{r}_j|\bar{r}_i)p(\bar{r}_i) = p(\bar{r}_j|\bar{r}_i)\frac{1}{V} \quad \text{(A13a)}$$

where $p(\bar{r}_j|\bar{r}_i)$ is the conditional probability density function. Let

$$p(\bar{r}_j|\bar{r}_i) = g(\bar{r}_j - \bar{r}_i)\frac{1}{V} \quad \text{(A13b)}$$

Then

$$p(\bar{r}_i, \bar{r}_j) = \frac{g(\bar{r}_j - \bar{r}_i)}{V^2} \quad \text{(A13c)}$$

Let P_D be the joint probability of 0 inside particle i and $\bar{r}$ inside particle j, $i \neq j$. This means

$$|\overline{r}_i - 0| < a, |\overline{r}_j - \overline{r}| < a \quad \text{(A14a)}$$

$$P(0 \text{ inside particle } i, \bar{r} \text{ inside particle } j) = \iint_{|\overline{r}_i - 0| < a, |\overline{r}_j - \overline{r}| < a} d\overline{r}_i d\overline{r}_j p(\overline{r}_i, \overline{r}_j) \quad \text{(A14b)}$$

The probability P_D is the sum over all particle i and j

$$P_D(\bar{r}) = \sum_{i=1}^{N} \sum_{j=1, j\neq i}^{N} P(0 \text{ inside particle } i, \bar{r} \text{ inside particle } j) \quad \text{(A15)}$$

Without loss of generality, let $\overline{r} = (0,0,r) = (0,0,z)$, which is shown in Figure A2.

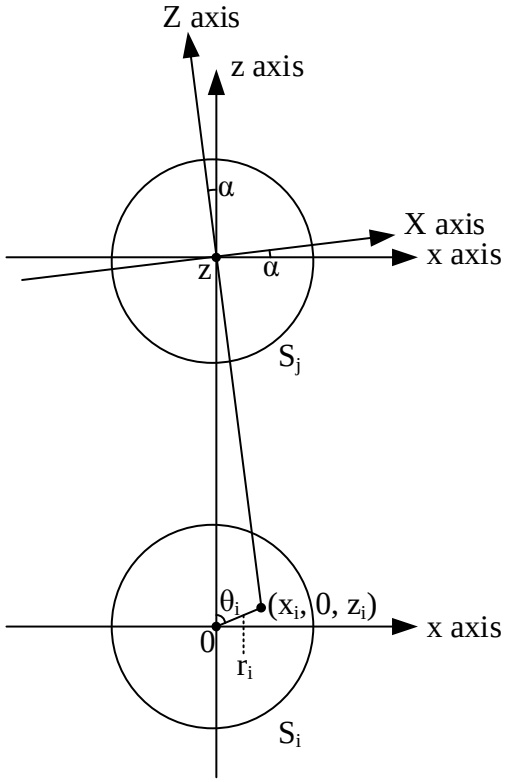

Figure A2. Particle positions 0 and $\bar{r}$ are located in different spheres S_i and S_j

Therefore

$$P_D(\bar{r}) = \frac{1}{V^2} \sum_{i=1}^{N} \sum_{j=1, j\neq i}^{N} \iint_{|\overline{r}_i - 0|<a, |\overline{r}_j - \overline{r}|<a} d\overline{r}_i d\overline{r}_j g(\overline{r}_i, \overline{r}_j) \quad \text{(A16a)}$$

$$P_D(\bar{r}) = \frac{N(N-1)}{V^2} \iint_{|\overline{r}_i - 0|<a, |\overline{r}_j - \overline{r}|<a} d\overline{r}_i d\overline{r}_j g(\overline{r}_i, \overline{r}_j) \quad \text{(A16b)}$$

$$P_D(\bar{r}) = n_0^2 \iint_{|\bar{r}_i - 0| < a, |\bar{r}_j - \bar{r}| < a} d\bar{r}_i d\bar{r}_j g(\bar{r}_i, \bar{r}_j) \quad \text{(A16c)}$$

From Equation (A16b) to (A16c), $N \gg 1$ is used. The above integral is six-fold over $dr_i d\theta_i d\phi_i dr_j d\theta_j d\phi_j$ for each $\bar{r}$. The six-fold integration can be reduced to four-fold, and computed using Brute force integration.

The integration is done over two spheres: S_i is the sphere of radius a about the origin, and S_j is the sphere of radius a about $(0,0,z) = (0,0,r)$. The integrand is independent of ϕ_i

$$\int d\bar{r}_i \int d\bar{r}_j g(\bar{r}_i, \bar{r}_j) = 2\pi \left[\iint dr_i r_i^2 d\theta_i \sin\theta_i \int d\bar{r}_j g(\bar{r}_i, \bar{r}_j) \right]_{\phi_i = 0} \quad \text{(A17)}$$

Let

$$\begin{aligned} x_i &= r_i \sin\theta_i \\ y_i &= 0 \\ z_i &= r_i \cos\theta_i \end{aligned} \quad \text{(A18)}$$

Figure A2 shows the two spherical particles S_i and S_j. A straight line is drawn joining $(0,0,z)$ to $\bar{r}_i = (r_i \sin\theta_i, 0, r_i \cos\theta_i)$

$$\hat{Z} = \frac{-r_i \sin\theta_i \, \hat{x} + (z - r_i \cos\theta_i)\hat{z}}{\sqrt{r_i^2 \sin^2\theta_i + (z - r_i \cos\theta_i)^2}} \quad \text{(A19)}$$

The angle between $\hat{Z}$ and $\hat{z}$ is shown in Figure A2

$$\cos\ \alpha = \frac{(z - r_i\, cos\, \theta_i)}{\sqrt{r_i^2\, sin^2\, \theta_i + (z - r_i\, cos\, \theta_i)^2}} \qquad \text{(A20)}$$

$$\sin\ \alpha = \frac{r_i sin\ \theta_i}{\sqrt{r_i^2\, sin^2\, \theta_i + (z - r_i\, cos\, \theta_i)^2}}$$

Let the Z coordinate to be defined as along the axis with $(0,0,z)$ as the origin: $X, Y, Z =$ corrdinates of $\overline{r}_j$ with respect to $(0,0,z)$. In spherical coordinates

$$\begin{aligned} X &= R \sin\Theta \cos\Phi \\ Y &= R \sin\Theta \sin\Phi \\ Z &= R \cos\Theta \end{aligned} \qquad \text{(A21)}$$

In the integration $\int_{|\overline{r}_j - \overline{r}| < a} d\overline{r}_j g(\overline{r}_i, \overline{r}_j)$, the ranges of variables are

$$\begin{aligned} 0 &< R < a \\ 0 &< \Theta < \pi \\ 0 &< \Phi < 2\pi \end{aligned} \qquad \text{(A22)}$$

Let $x_j, y_j, z_j =$ corrdinates of $\overline{r}_j$ with respect to $(0,0,0)$, which is shown in Figure A3.

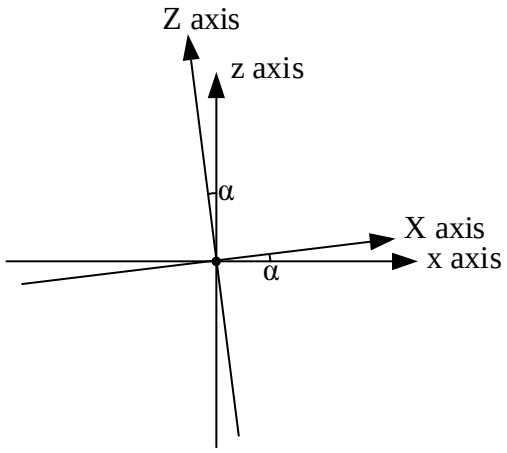

Figure A3. Coordinate rotation

Using the coordinate rotation

$$\begin{aligned} x_j &= X\cos\alpha - Z\sin\alpha \\ z_j - z &= X\sin\alpha + Z\cos\alpha \\ y_j &= Y \end{aligned} \tag{A23}$$

The pair distribution function $g(\bar{r}_i, \bar{r}_j)$ depends on $\bar{r}_j - \bar{r}_i$, which can be expressed in the Cartesian coordinate

$$\begin{aligned} x_j - x_i &= R\,sin\,\Theta\,cos\,\Phi\,cos\,\alpha - R\,cos\,\Theta\,sin\,\alpha - r_i\,sin\,\theta_i \\ y_j - y_i &= R\,sin\,\Theta\,sin\,\Phi \\ z_j - z_i &= R\,sin\,\Theta\,cos\,\Phi\,sin\,\alpha + R\,cos\,\Theta\,cos\,\alpha + z - r_i\,cos\,\theta_i \end{aligned} \tag{A24}$$

Then the magnitude $|\bar{r}_j - \bar{r}_i|$ is calculated as

$$(x_j - x_i)^2 = R^2 sin^2\ \Theta cos^2\ \Phi \frac{(z - r_i\,cos\,\theta_i)^{\,2}}{r_i^2\,sin^2\,\theta_i + (z - r_i\,cos\,\theta_i)^2} - \frac{2\,R sin\,\Theta\,cos\,\Phi (z - r_i\,cos\,\theta_i)\,r_i\,sin\,\theta_i}{\sqrt{r_i^2\,sin^2\,\theta_i + (z - r_i\,cos\,\theta_i)^2}} \left[\frac{R\,cos\,\Theta}{\sqrt{r_i^2\,sin^2\,\theta_i + (z - r_i\,cos\,\theta_i)^2}} + 1 \right] + r_i^2 sin^2\ \theta_i \left[\frac{R\,cos\,\Theta}{\sqrt{r_i^2\,sin^2\,\theta_i + (z - r_i\,cos\,\theta_i)^2}} + 1 \right]^2 \tag{A25a}$$

$$(y_j - y_i)^2 = R^2 sin^2\ \Theta sin^2\ \Phi \tag{A25b}$$

$$(z_j - z_i)^2 = R^2 sin^2\ \Theta cos^2\ \Phi \frac{r_i^2\ sin^2\ \theta_i}{r_i^2\ sin^2\ \theta_i + (z - r_i\ cos\ \theta_i)^2}$$

$$+ \frac{2\ Rsin\ \Theta\ cos\ \Phi r_i\ sin\ \theta_i (z - r_i\ cos\ \theta_i)}{\sqrt{r_i^2\ sin^2\ \theta_i + (z - r_i\ cos\ \theta_i)^2}} \left[\frac{(Rcos\ \Theta)}{\sqrt{r_i^2\ sin^2\ \theta_i + (z - r_i\ cos\ \theta_i)^2}} \right.$$

$$\left. + 1 \right] + (z - r_i cos\ \ \theta_i)^2 \left[\frac{(Rcos\ \Theta)}{\sqrt{r_i^2\ sin^2\ \theta_i + (z - r_i\ cos\ \theta_i)^2}} + 1 \right]^2 \quad \text{(A25c)}$$

Adding all three terms together, the cross terms will cancel. Then

$$(z_j - z_i)^2 + (y_j - y_i)^2 + (x_j - x_i)^2$$

$$= R^2 sin^2\ \Theta cos^2\ \Phi \frac{r_i^2 sin^2\ \ \theta_i + (z - r_i\ cos\ \theta_i)^2}{r_i^2 sin^2\ \ \theta_i + (z - r_i\ cos\ \theta_i)^2}$$

$$+ r_i^2 sin^2\ \ \theta_i \left[\frac{Rcos\ \Theta}{\sqrt{r_i^2\ sin^2\ \theta_i + (z - r_i\ cos\ \theta_i)^2}} + 1 \right]^2 + R^2 sin^2\ \ \Theta sin^2\ \ \Phi$$

$$+ (z - r_i cos\ \ \theta_i)^2 \left[\frac{Rcos\ \Theta}{\sqrt{r_i^2\ sin^2\ \theta_i + (z - r_i\ cos\ \theta_i)^2}} + 1 \right]^2 \quad \text{(A26a)}$$

$$(z_j - z_i)^2 + (y_j - y_i)^2 + (x_j - x_i)^2$$

$$= R^2 sin^2\ \Theta + r_i^2 sin^2\ \theta_i \left[\frac{Rcos\,\Theta}{\sqrt{r_i^2\ sin^2\,\theta_i + (z - r_i\,cos\,\theta_i)^2}} + 1\right]^2$$

$$+ (z - r_i cos\ \theta_i)^2 \left[\frac{Rcos\,\Theta}{\sqrt{r_i^2\ sin^2\,\theta_i + (z - r_i\,cos\,\theta_i)^2}} + 1\right]^2 \quad \text{(A26b)}$$

Therefore the magnitude $\left|\bar{r}_j - \bar{r}_i\right|$ is independent on Φ as expected. The above expression can be further simplified

$$(z_j - z_i)^2 + (y_j - y_i)^2 + (x_j - x_i)^2$$

$$= R^2\ sin^2\,\Theta$$

$$+ [r_i^2\ sin^2\,\theta_i + (z - r_i\,cos\,\theta_i)^2]\left[\frac{Rcos\,\Theta}{\sqrt{r_i^2\ sin^2\,\theta_i + (z - r_i\,cos\,\theta_i)^2}} + 1\right]^2 \quad \text{(A27a)}$$

$$= R^2\ sin^2\,\Theta$$

$$+ [r_i^2\ sin^2\,\theta_i + (z - r_i\,cos\,\theta_i)^2]\left[\frac{R^2\,cos^2\,\Theta}{r_i^2\ sin^2\,\theta_i + (z - r_i\,cos\,\theta_i)^2}\right.$$

$$\left. + 2\frac{(Rcos\,\Theta)}{\sqrt{r_i^2\ sin^2\,\theta_i + (z - r_i\,cos\,\theta_i)^2}} + 1\right]$$

$$(z_j - z_i)^2 + (y_j - y_i)^2 + (x_j - x_i)^2$$

$$= R^2 + 2\frac{Rcos\ \Theta[r_i^2 sin^2\ \theta_i + (z - r_i cos\ \theta_i)^2]}{\sqrt{r_i^2 sin^2\ \theta_i + (z - r_i cos\ \theta_i)^2}}$$

$$+ [r_i^2\, sin^2\, \theta_i + (z - r_i\, cos\, \theta_i)^2] \qquad \text{(A27b)}$$

$$\left|\overline{r}_j - \overline{r}_i\right|$$

$$= \sqrt{R^2 + 2R\cos\Theta\sqrt{r_i^2 sin^2\ \theta_i + (z - r_i cos\ \theta_i)^2} + [r_i^2\, sin^2\, \theta_i + (z - r_i\, cos\, \theta_i)^2]} \qquad \text{(A27c)}$$

Then the $d\Phi$ integration gives 2π, therefore only a four-fold integration over $dr_i d\theta_i dRd\Theta$ is needed instead of the original six-fold integration. Let $\mu_i = \cos\theta_i\,, \mu = \cos\Theta$, then

$$P_D(\bar{r}) = P_D(r) = (2\pi n_0)^2 \int_0^a dr_i r_i^2 \int_{-1}^1 d\mu_i \int_0^a dRR^2 \int_{-1}^1 d\mu \qquad \text{(A28)}$$

$$g\left(\sqrt{R^2 + 2R\mu\sqrt{r_i^2(1-\mu_i^2) + (r - r_i\mu_i)^2} + [r_i^2(1-\mu_i^2) + (r - r_i\mu_i)^2]}\right)$$

The integral in Equation (A28) can be computed using Fourier transform. Define

$$V(\overline{r}', \overline{r}) = \begin{cases} 1 & \text{if both } |\overline{r}| < a, \left|\overline{r}'\right| < a \\ 0 & \text{otherwise} \end{cases} \qquad \text{(A29)}$$

Then

$$P_D(\overline{r}', \overline{r}) = n_0^2 \iint\limits_{\left|\overline{r}_i - \overline{r}'\right| < a, |\overline{r}_j - \overline{r}| < a} d\overline{r}_i d\overline{r}_j g(\overline{r}_i, \overline{r}_j) \qquad \text{(A30a)}$$

$$P_D(\overline{r}', \overline{r}) = n_0^2 \iint d\overline{r}_i d\overline{r}_j V(\overline{r}' - \overline{r}_i, \overline{r} - \overline{r}_j) g(\overline{r}_i, \overline{r}_j) \qquad \text{(A30b)}$$

Without loss of generality, $\bar{r}' = 0$ is assumed. Then $P_d(\overline{r}', \overline{r})$ is

$$P_D(\overline{r}', \overline{r}) = n_0^2 \iint d\overline{r}_i d\overline{r}_j V(\overline{r}' - \overline{r}_i, \overline{r} - \overline{r}_j)[g(\overline{r}_i, \overline{r}_j) - 1] + n_0^2 \iint d\overline{r}_i d\overline{r}_j V(\overline{r}' - \overline{r}_i, \overline{r} - \overline{r}_j) \quad \text{(A31a)}$$

Substituting in the definition of $V(\bar{r}', \bar{r})$

$$\iint d\overline{r}_i d\overline{r}_j V(\overline{r}' - \overline{r}_i, \overline{r} - \overline{r}_j) = \int_{|\overline{r}' - \overline{r}_i| < a} d\overline{r}_i \int_{|\overline{r} - \overline{r}_j| < a} d\overline{r}_j = \left(\frac{4\pi a^3}{3}\right)^2 \quad \text{(A31b)}$$

Therefore

$$P_D(\overline{r}', \overline{r}) = P_{dc}(\overline{r}', \overline{r}) + f^2 \quad \text{(A31c)}$$

$$P_{dc}(\overline{r}', \overline{r}) = n_0^2 \iint d\overline{r}_i d\overline{r}_j V(\overline{r}' - \overline{r}_i, \overline{r} - \overline{r}_j)[g(\overline{r}_i, \overline{r}_j) - 1] \quad \text{(A31d)}$$

$$P_{dc}(\overline{r}', \overline{r}) = n_0^2 \iint d\overline{r}_i d\overline{r}_j V(\overline{r}' - \overline{r}_i, \overline{r} - \overline{r}_j) h(\overline{r}_i, \overline{r}_j) \quad \text{(A31e)}$$

where $f = n_0 \frac{4\pi a^3}{3}$ is the fraction volume. Note that in statistical homogeneous medium

$$P_{dc}(\overline{r}', \overline{r}) = P_{dc}(\overline{r}' - \overline{r}) \quad \text{(A32a)}$$

$$h(\overline{r}_i, \overline{r}_j) = h(\overline{r}_i - \overline{r}_j) \quad \text{(A32b)}$$

It is clearly seen that Equation (A31e) is in spatial convolution functional form. Then 3D Fourier transforms are defined as follow

$$h(\overline{r}) = \int d\overline{p} H(\overline{p}) \exp(i\overline{p} \cdot \overline{r}) \quad \text{(A33a)}$$

Let

$$P_{dc}(\bar{r}) = \int d\overline{p} exp(i\overline{p} \cdot \overline{r}) P_{dc}(\overline{p})$$	(A33b)
$$P_{dc}(\overline{p}) = \frac{1}{(2\pi)^3} \int d\overline{r} exp(-i\overline{p} \cdot \overline{r}) P_{dc}(\overline{r})$$	(A33c)
$$V(\overline{r}', \overline{r}) = \int d\overline{p} \int d\overline{p}' \exp(i\overline{p}' \cdot \overline{r}' - i\overline{p} \cdot \overline{r}) V(\overline{p}', \overline{p})$$	(A33d)

Then Equation (A31e) becomes

$$\int d\overline{p} \exp\left(i\overline{p} \cdot (\overline{r}' - \overline{r})\right) P_{dc}(\overline{p}) = n_0^2 \iint d\overline{r}_i d\overline{r}_j \int d\overline{p} \int d\overline{p}' \exp\left(i\overline{p}' \cdot (\overline{r}' - \overline{r}_i) - i\overline{p} \cdot (\overline{r} - \overline{r}_j)\right) V(\overline{p}', \overline{p}) \int d\overline{p}_1 H(\overline{p}_1) \exp\left(i\overline{p}_1 \cdot (\overline{r}_i - \overline{r}_j)\right)$$	(A34a)
$$\int d\overline{p} \exp\left(i\overline{p} \cdot (\overline{r}' - \overline{r})\right) P_{dc}(\overline{p}) = n_0^2 \iint d\overline{r}_i d\overline{r}_j \int d\overline{p} \int d\overline{p}' \exp(i\overline{p}' \cdot \overline{r}' - i\overline{p} \cdot \overline{r}) \exp\left(i\overline{p}' \cdot (-\overline{r}_i) - i\overline{p} \cdot (-\overline{r}_j)\right) V(\overline{p}', \overline{p}) \int d\overline{p}_1 H(\overline{p}_1) \exp\left(i\overline{p}_1 \cdot (\overline{r}_i - \overline{r}_j)\right)$$	(A34b)

After switching the integration order, the integral over $d\overline{r}_i d\overline{r}_j$ will give δ function

$$\iint d\overline{r}_i d\overline{r}_j \exp(-i\overline{p}' \cdot \overline{r}_i + i\overline{p} \cdot \overline{r}_j) \exp\left(i\overline{p}_1 \cdot (\overline{r}_i - \overline{r}_j)\right) = (2\pi)^6 \delta(\overline{p}' - \overline{p}_1) \delta(\overline{p} - \overline{p}_1)$$	(A35)

Therefore Equation (A34b) becomes

$$\int d\overline{p}\exp\left(i\overline{p}\cdot\left(\overline{r}'-\overline{r}\right)\right)P_{dc}(\overline{p}) = n_0^2\int d\overline{p}\int d\overline{p}'\exp\left(i\overline{p}'\cdot\overline{r}'-i\overline{p}\cdot\overline{r}\right)V\left(\overline{p}',\overline{p}\right)\int d\overline{p}_1 H\left(\overline{p}_1\right)(2\pi)^6\delta\left(\overline{p}'-\overline{p}_1\right)\delta\left(\overline{p}-\overline{p}_1\right) \quad \text{(A36a)}$$

$$\int d\overline{p}\exp\left(i\overline{p}\cdot\left(\overline{r}'-\overline{r}\right)\right)P_{dc}(\overline{p}) = n_0^2\int d\overline{p}_1 H\left(\overline{p}_1\right)(2\pi)^6 V\left(\overline{p}_1,\overline{p}_1\right)\exp\left(i\overline{p}_1\cdot\overline{r}'-i\overline{p}_1\cdot\overline{r}\right) \quad \text{(A36b)}$$

$$\int d\overline{p}\exp\left(i\overline{p}\cdot\left(\overline{r}'-\overline{r}\right)\right)P_{dc}(\overline{p}) = n_0^2\int d\overline{p}H(\overline{p})(2\pi)^6 V(\overline{p},\overline{p})\exp\left(i\overline{p}\cdot\overline{r}'-i\overline{p}\cdot(\overline{r})\right) \quad \text{(A36c)}$$

$$P_{dc}(\overline{p}) = n_0^2 V(\overline{p},\overline{p})H(\overline{p})(2\pi)^6 \quad \text{(A36d)}$$

where $V(\overline{p},\overline{p})$ can be obtained from the Fourier transform

$$V\left(\overline{p}',\overline{p}\right) = \frac{1}{(2\pi)^6}\int_{\left|\overline{r}'\right|<a} d\overline{r}'\int_{|\overline{r}|<a} d\overline{r}\exp\left(-i\overline{p}'\cdot\overline{r}'+i\overline{p}\cdot\overline{r}\right) \quad \text{(A37)}$$

The integral in Equation (A37) can be decomposed into two integral over $d\overline{r}'$ and $d\overline{r}$ respectively.

$$V(\overline{p}',\overline{p}) = \frac{1}{(2\pi)^6}Q(p)Q^*(p') \quad \text{(A38a)}$$

where

$$Q(p) = \int_{|\overline{r}|<a} d\overline{r}\exp(i\overline{p}\cdot\overline{r}) \quad \text{(A38b)}$$

Let $\mu = \cos\theta$

$$Q(p) = 2\pi \int_0^a drr^2 \int_{-1}^1 d\mu \exp(ipr\mu) = \frac{2\pi}{ip} \int_0^a drr[\exp(ipr) - \exp(-ipr)] \quad \text{(A38c)}$$

Then $Q(p)$ is

$$Q(p) = \frac{4\pi a^2}{p} j_1(pa) \quad \text{(A39a)}$$

where $j_1(.)$ is the first order spherical Bessel function.

$$j_1(pa) = \frac{\sin(pa)}{p^2 a^2} - \frac{\cos(pa)}{pa} \quad \text{(A39b)}$$

Then according Equation (A36d) and (A38a)

$$V(\overline{p}, \overline{p}) = \frac{1}{(2\pi)^6} Q^2(p) \quad \text{(A40a)}$$

$$P_{dc}(\overline{p}) = n_0^2 V(\overline{p}, \overline{p}) H(\overline{p}) (2\pi)^6 = n_0^2 Q^2(p) H(p) \quad \text{(A40b)}$$

The calculation of $H(p)$ for single size, sticky and multi-size are described in [11]. By assuming spherical symmetry, it is readily shown that $P_{dc}(\overline{r})$ can be reduced to 1D integral

$$P_{dc}(r) = 4\pi \int_0^{+\infty} dpp^2 P_{dc}(p) \frac{\sin(pr)}{pr} \quad \text{(A41a)}$$

$$P_{dc}(\bar{r}) = (4\pi)^3 n_0^2 a^4 \int_0^{+\infty} dp j_1^2(pa) \frac{\sin(pr)}{pr} \quad \text{(A41b)}$$

In summary, the complete expression of correlation function is

$$C(\bar{r}) = P_S(\bar{r}) + P_D(\bar{r}) = P_S(\bar{r}) + P_{dc}(\bar{r}) + f_V^2 \quad \text{(A42a)}$$

$$P_S = \begin{cases} 0 & r > 2a \\ n_0\left(\frac{4\pi a^3}{3}\right)\left[1 - \frac{3}{4}\frac{r}{a} + \frac{1}{16}\left(\frac{r}{a}\right)^3\right] & 0 \le r \le 2a \end{cases}$$	(A42b)
$$P_{dc}(\bar{r}) = (4\pi)^3 n_0^2 a^4 \int_0^{+\infty} dp j_1^2(pa)\frac{\sin(pr)}{pr} H(p)$$	(A42c)
$$H(p) = \frac{C(p)}{1 - n_0(2\pi)^3 C(p)}$$	(A42d)
$$j_1(pa) = \frac{\sin(pa)}{(pa)^2} - \frac{\cos(pa)}{pa}$$	(A42e)

The Equations (A42a) – (A42e) are consistent with the expressions in [58]. The two point correlation function $S_2(r)$ is

$$S_2(r) = 1 - \rho V_2(r) + \rho^2 M(r)$$	(A43a)
$$V_2(r) = \begin{cases} \frac{4\pi}{3}\left(1 + \frac{3}{4}r - \frac{r^3}{16}\right) & r < 2 \\ \frac{8\pi}{3} & r > 2 \end{cases}$$	(A43b)
$$M(r) = \frac{1}{2\pi^2 r}\int_0^{+\infty} dk \frac{\hat{c}(k)}{1 - \rho\hat{c}(k)}\,\hat{m}^2(k) k \sin(kr) + \frac{16\pi^2}{9}$$	(A43c)
$$\hat{m}(k) = \frac{4\pi}{k}\left(\frac{\sin k}{k^2} - \frac{\cos k}{k}\right)$$	(A43d)

In [58], unit radius is assumed, so $a = 1$. Besides, the symbols correspondence are $\rho = n_0$, $p = k$, and $\hat{c}(k) = (2\pi)^3 C(k) = (2\pi)^3 C(p)$. Therefore when $r < 2$

$$S_2(r) = \left(1 - n_0\frac{8\pi}{3} + n_0^2\frac{16\pi^2}{9}\right) + n_0\frac{4\pi}{3}\left(1 - \frac{3}{4}r + \frac{r^3}{16}\right) + (4\pi)^3 n_0^2 \int_0^{+\infty} dp\, \frac{C(p)}{1 - n_0(2\pi)^3 C(p)} \left(\frac{\sin p}{p^2} - \frac{\cos p}{p}\right)^2 \frac{\sin(pr)}{pr} \quad \text{(A44a)}$$

$$C(\bar{r}) = \left(n_0\frac{4\pi}{3}\right)^2 + n_0\frac{4\pi}{3}\left(1 - \frac{3}{4}r + \frac{1}{16}r^3\right) + (4\pi)^3 n_0^2 \int_0^{+\infty} dp \left(\frac{\sin p}{p^2} - \frac{\cos p}{p}\right)^2 \frac{\sin(pr)}{pr} \frac{C(p)}{1 - n_0(2\pi)^3 C(p)} \quad \text{(A44b)}$$

When $r > 2$

$$S_2(r) = \left(1 - n_0\frac{8\pi}{3} + n_0^2\frac{16\pi^2}{9}\right) + (4\pi)^3 n_0^2 \int_0^{+\infty} dp\, \frac{C(p)}{1 - n_0(2\pi)^3 C(p)} \left(\frac{\sin p}{p^2} - \frac{\cos p}{p}\right)^2 \frac{\sin(pr)}{pr} \quad \text{(A45a)}$$

$$C(\bar{r}) = \left(n_0\frac{4\pi}{3}\right)^2 + (4\pi)^3 n_0^2 \int_0^{+\infty} dp \left(\frac{\sin p}{p^2} - \frac{\cos p}{p}\right)^2 \frac{\sin(pr)}{pr} \frac{C(p)}{1 - n_0(2\pi)^3 C(p)} \quad \text{(A45b)}$$

It is observed that $S_2(r)$ and $C(\bar{r})$ only differ in the constant value. It is also noted that the steady values of the two correlation functions are

$$S_2(\infty) = 1 - n_0\frac{8\pi}{3} + n_0^2\frac{16\pi^2}{9} = \left(1 - n_0\frac{4\pi}{3}\right)^2 = (1 - f_V)^2 \quad \text{(A46a)}$$

$$C(\infty) = \left(n_0\frac{4\pi}{3}\right)^2 = f_V^2 \quad \text{(A46b)}$$

This difference is due to the different definitions of the indicator functions. In [58]

$$S_2(\bar{r}_1, \bar{r}_2) = P(\Theta_A(\bar{r}_1) = 1, \Theta_A(\bar{r}_2) = 1) \quad \text{(A47a)}$$

$\Theta_A(\bar{r}) = \begin{cases} 1 & \bar{r} \text{ in air background} \\ 0 & \bar{r} \text{ in ice particle} \end{cases}$	(A47b)

However in this thesis

$C(\bar{r}_1, \bar{r}_2) = P(\Theta_B(\bar{r}_1) = 1, \Theta_B(\bar{r}_2) = 1)$	(A48a)
$\Theta_B(\bar{r}) = \begin{cases} 1 & \bar{r} \text{ in ice particle} \\ 0 & \bar{r} \text{ in air background} \end{cases}$	(A48b)